Digital Light Processing Bioprinting Full-Thickness Human Skin for Modelling Infected Chronic Wounds *in Vitro*

by

Evan Stefanek
Bachelor of Engineering, University of Victoria, 2020

A Thesis Submitted in Partial Fulfillment
of the Requirements for the Degree of

Master of Applied Science

in the Department of Mechanical Engineering

Supervisory Committee

Digital Light Processing Bioprinting Full-Thickness Human Skin for Modelling Infected Chronic Wounds *in Vitro*

by

Evan Stefanek
Bachelor of Engineering, University of Victoria, 2020

Supervisory Committee

Dr. Mohsen Akbari, Mechanical Engineering

Supervisor

Dr. Stephanie Willerth, Mechanical Engineering

Departmental Member

Dr. Mina Hoorfar, Mechanical Engineering

Departmental Member

Abstract

Chronic wounds have a detrimental impact on patient quality of life, a significant economic cost, and often lead to severe outcomes such as amputation, sepsis or death. The elaborate interplay between bacteria, cutaneous cells, immune cells, growth factors, and proteases in chronic wounds has complicated the development of new therapies that could improve outcomes for chronic wound patients. Existing *in vitro* models of chronic wounds do not appreciably mimic the complexity of the wound environment. In this work, tissue-engineered skin was developed with the goal of creating an *in vitro* platform appropriate for testing potential clinical therapies for chronic wounds. The Lumen-X, a digital light processing bioprinter, was used to create tissue-engineered skin from a 7.5% (w/v) gelatin methacryloyl hydrogel laden with primary dermal fibroblasts. This dermal layer was developed with an emphasis on providing a favourable microenvironment for the fibroblasts in order to mimic their *in vivo* phenotype. An epidermal layer of human keratinocytes was formed on the hydrogel surface and stratified through culture at the air-liquid-interface. The maturation of the epidermis was thoroughly characterized with histology, immunohistochemistry, and trans-epithelial electrical resistance analyses which showed a degree of maturation suitable for wound healing studies. To verify the suitability of this tissue-engineered skin for studying healing *in vitro*, sharp tweezers were used to create physical wounds in the epidermis which were then infected with *Pseudomonas aeruginosa*. Reepithelialisation, the production of the pro-inflammatory cytokine TNF-α, and the presence of bacteria were monitored over time, showing healing in wounds without infection and those treated with antibiotics, and potential biofilm formation in infected wounds. The tissue-engineered skin developed here is suitable for use as an *in vitro* model of the infected chronic wound environment. Future work includes developing better methods for creating the physical wound and characterizing the bacterial biofilm in order to improve the reproducibility and clarity of results. Such a model will then be well-poised to begin testing potential chronic wound therapies *in vitro*.

Table of Contents

Supervisory Committee ii
Abstract iii
Table of Contents v
List of Figures vii
List of Tables xi
Glossary xii
Acknowledgements xiii
Chapter 1 - Introduction 1
  1.1 Anatomy of Human Skin 3

  1.2 The Wound Healing Process 6

  1.3 Chronic Wounds 9

  1.4 Tissue-Engineered Skin Models 13

  1.5 Natural Hydrogels and Gelatin Methacryloyl 18

  1.6 Extrusion and DLP Bioprinting 23

  1.7 Conclusion and Outlook 25

Chapter 2 - Optimization of the Dermal Layer 27
  2.1 Materials and Methods 29

  2.2 Results and discussion 36

  2.3 Conclusion 45

Chapter 3 - Establishment and Verification of the Epidermal Layer 46
  3.1 Materials and Methods 47

  3.2 Results and Discussion 53

  3.5 Conclusion 63

Chapter 4 – Healing of Infected *in Vitro* Wounds 65
  4.1 Materials and Methods 66

4.2 Results and Discussion 69

4.3 Conclusion 73

Chapter 5 - Conclusion and Future Work 75
References 78

List of Figures

Figure 1-1: (A) Anatomy of the epidermis and dermis (adapted with permission from [19]). (B) Layers of the epidermis (reproduced with permission [19]). 3

Figure 1-2: Diagram of the cornified envelope and upper stratum granulosum (reproduced with permission [18]). 5

Figure 1-3: Schematic of a wound at the end of the **inflammatory phase** of healing (Reproduced with permission from [2] Copyright Massachusetts Medical Society). 7

Figure 1-4: Schematic of a wound near the end of the **proliferative phase** of healing (Reproduced with permission from [2] Copyright Massachusetts Medical Society). 8

Figure 1-5: The process of biofilm formation by planktonic bacteria (reproduced with permission [26]). 11

Figure 1-6: Comparison of human skin (A, C, E, G) with various examples of tissue-engineered skin (B, D, F, H). Tissue-engineered skin models included a polystyrene scaffold (B, H), casted plasma hydrogel (D), and bioprinted hybrid hydrogel (F). Keratin (C, D) and filaggrin (G, H) are shown in green, and laminin is shown in orange in human skin (E) and white in the example of tissue-engineered skin (F). In all IHC images (C-H) the nuclei are counterstained in blue. A, B, H reproduced with permission [46]; C, D reproduced with permission [47]; F reproduced with permission [37]. 14

Figure 1-7: The most biologically relevant in vitro chronic wounds models. (A) Tissue-engineered human skin that was artificially wounded (i) to study reepithelialisation in the presence of chronic wound fluid (ii) (creative commons attribution license [49]). (B) A human epidermis above a perfusable channel (i,ii) that was scratched, infected, and treated with antibiotics to study reepithelialisation (iii) (creative commons attribution license [50]). 17

Figure 1-8: Synthesis of GelMA through the reaction of gelatin with methacrylic anhydride (MA) (reproduced with permission [76]) 21

Figure 1-9: Influence of DoF (reproduced with permission [79]) and GelMA concentration (creative commons attribution license [82]) on the microporosity of the crosslinked hydrogel. Note the discrepancy in scale between A and B. 22

Figure 1-10: (A) F-actin staining of human dermal fibroblasts after 7 days in culture encapsulated in GelMA hydrogels (scale bar = 200 µm, creative commons attribution license [82]). (B) Live and dead staining of human neonatal dermal fibroblasts after 3 days of culture encapsulated in GelMA hydrogels (reproduced with permission [36]). 23

Figure 1-11: Simplified schematic of the DLP bioprinting mechanism. Created with BioRender.com. 25

Figure 2-1: Cytotoxicity of 90 minutes of LAP and/or Tartrazine Exposure to Fibroblasts in 2D Culture. 'Bioink' = 0.3% LAP and 2.5mM tartrazine. * $p < 0.05$. 37

Figure 2-2: Printability of 5%, 7.5%, and 10% (w/v) GelMA demonstrated by DLP bioprinting a model containing circular pores with nominal diameters of 2 mm (left), 1 mm (middle), 500 µm (top right), and 250 µm (bottom right). Scale bar: 1 cm. 38

Figure 2-3: Schematic of the tissue-engineered skin biofabrication process. GelMA hydrogel and primary fibroblasts are combined and DLP bioprinted into porous constructs (i) with a flat apical surface (ii), and microporous interior (iii) that is laden with fibroblasts (iv). HaCaT cells are added and after culture at the ALI a stratified and matured epidermis forms (v, vi). Scale bars: 1 mm (i), 100 µm (ii, iv), 50 µm (iii, v, vi). 40

Figure 2-4: Fibroblasts DLP bioprinted in 5, 7.5, and 10% (w/v) GelMA on days 1 and 5 shown with a live (green) and dead (red) stain. Scale bars: 500 µm; and 100 µm in the high magnification insets. 41

Figure 2-5: Distribution of fibroblasts throughout a DLP bioprinted 7.5% GelMA construct after 5 days of culture. (A) Fibroblasts on the basal surface. (B) Maximum projection from a side-view of the construct. (C) Stack of images showing fibroblasts encapsulated in the interior of the hydrogel. Scale bars: 200 µm........ 42

Figure 2-6: Fibroblast proliferation in DLP bioprinted GelMA constructs over 5 days of culture (*p<0.05, **p<0.01, ***p<0.001). 43

Figure 2-7: Representative images of cell densities in the tissue-engineered dermis after 5 days of culture and human reticular dermis shown. White arrows indicate fibroblasts. Scale bars: 50 µm. 44

Figure 3-1:HaCaT plasma membrane labelling with DiI. Scale bars: 100 µm........ 48

Figure 3-2: HaCaT attachment to 5, 7.5, and 10% GelMA surfaces after 1 and 2 seedings. (A) DiI labelled HaCaT cells shown at low magnification (scale bar: 500 µm) with higher magnification insets (scale bar: 100 µm). (B) Quantification of HaCaT surface coverage after 1 and two seedings (*p<0.0001)........ 55

Figure 3-3: (A) The implementation of submerged and ALI culture with Transwell inserts. (B) Top-view of tissue-engineered skin after 2 weeks of maturation. (C) Stack of brightfield images at various heights of the tissue-engineered skin after 2 weeks of maturation. Scale bar: 100 µm. .. 57

Figure 3-4: H&E staining of tissue-engineered skin cross-sections after 7 days culture at the ALI shows (A) the gross tissue morphology, (B) the epidermal layer, (C) the presence of dermal fibroblasts either in small cavities (white arrow) or spread in the hydrogel, and (D) the contrasting smooth and 'ribbed' appearances of the GelMA hydrogel. Scale bar: 100 µm (A) and 50 µm (B, C, and D). 58

Figure 3-5: The morphology of tissue-engineered skin after 1 and 2 weeks of ALI culture with dermal fibroblasts (+fibroblasts) and without (-fibroblasts) in comparison to human skin. White arrows indicate flattened keratinocytes. Scale bars: 50 µm. 59

Figure 3-6: Localization of filaggrin (orange) in tissue-engineered and human skin via IHC with a nuclear counterstain (blue). Scale bars: 50 µm. 60

Figure 3-7: Localization of filaggrin in (A) tissue-engineered skin without fibroblasts on ALI week 2, (B) tissue-engineered skin with fibroblasts on ALI week 1, and (C) human skin. Scale bars: 50 µm. 61

Figure 3-8: Localization of Ki-67 in (A) tissue-engineered skin +fibroblasts on ALI 1 week and (B) human skin. White arrows indicate some of the Ki-67 positive keratinocytes. Scale bars: 50 µm. 62

Figure 3-9: Comparison of the TEER of GelMA hydrogel, tissue-engineered skin, and human skin (*p<0.05, **p<0.01, ***p<0.001). 63

Figure 4-1: Standard curve for the detection of TNF-α with ELISA 69

Figure 4-2:Infection of in vitro wound with P. aeruginosa 70

Figure 4-3: Reepithelialisation and bacterial colonization on uninfected (control), infected, and treated wounds in tissue-engineered skin. Scale bars: 50 µm. 71

Figure 4-4:Production of the pro-inflammatory cytokine TNF-α in tissue-engineered skin (A) during maturation at the ALI and (B) after wounding and infection (*p<0.05). 72

Figure 4-5: Progression of infection in an artificial wound. White arrows indicate bacteria. Scale bars: 100 µm. 73

List of Tables

Table 1-1: Comparison between healing wounds and chronic wounds. 10

Table 1-2: Existing in vitro models of chronic wounds. 16

Table 2-1: Fibroblast cell type and densities in tissue-engineered skin models. 28

Table 2-2: Bioink compositions for DLP bioprinting GelMA hydrogels 32

Table 2-3: Printability map of circular pores in 5, 7.5, and 10% GelMA. 38

Table 3-1: Antibodies used for IHC on tissue-engineered or human skin. 52

Glossary

2D – Two dimensional

3D – Three dimensional

ALI – Air-liquid-interface

bFGF – Basic fibroblast growth factor

CAD – Computer aided design

ELISA – Enzyme linked immunosorbent assay

IHC – Immunohistochemistry

PDGF – Platelet derived growth factor

P. aeruginosa – Pseudomonas aeruginosa

TGFβ – Transforming growth factor β

TIMP – Tissue inhibitor of matrix proteases

TNF-α – Tumor necrosis factor α

VEGF – Vascular endothelial growth factor

Acknowledgements

First, I would like to thank my supervisor Dr. Akbari for his guidance and support during my time in his lab. He gave me enough freedom and autonomy to learn and grow while also providing insight, detailed advice, and optimism whenever I told him “this isn’t possible”. I am grateful for the opportunity he has provided me.

I would like to thank my fellow lab members, past and present, who motivated me to begin this journey and have helped on every step of the way. I have Bahram Mirani and Brent Godau to thank for their assistance and patience back when I was just a co-op student on a summer job—I have been hooked on tissue engineering ever since. Pietro Arnaldi, Briana Dallinger, and Zhina Hadisi, you were all instrumental in various parts of my thesis project, thank you for your assistance and time. Finally, I would like to thank Hossein Dabiri, Amir Seyfoori, and Meitham Amereh for answering my questions, our informal discussions, and for coming to me for advice; you never truly understand something unless you can explain it to someone else. I wish you all the best and hope we get the chance to work together again in the future.

Finally, I want to thank my fiancé and my family. Without your support, motivation, and companionship I would not have made it to where I am today.

Chapter 1 - Introduction

Human skin is a multifunctional organ that protects the body from pathogens, prevents water loss, provides sensation, and can heal upon physical injury. In most cases, healing progresses through an orderly cascade of stages which return the wound site to a similar state as before, albeit with minor differences in mechanical strength and pigmentation. However, in some circumstances, wounds fail to heal normally and remain in an inflamed state with little closure over a period of months. These non-healing, or chronic, wounds are usually found in patients with underlying conditions such as diabetes mellitus, spinal cord injuries, or vascular disease [1], [2]. Determining the prevalence of chronic wounds is a well acknowledged challenge due to inconsistencies in classifying chronic versus other types of wounds, under-reported self-treated cases, and inaccessible clinical databases [3]–[5]. The Canadian Institute for Health Information (CIHI) conservatively estimates that the prevalence of chronic wounds in long-term care residents in Canada is 10%, with more specific data on wound severity or prevalence in the general Canadian population being unavailable [3]. The current standard of care for chronic wounds varies depending on the wound etiology, size, and the progression of healing, but usually includes a combination of offloading, debridement, topical or systemic antimicrobials, and a wound dressing that balances moisture levels. Despite best clinical practices, chronic wounds can still have a detrimental impact on patient health and quality of life and may eventually lead to severe outcomes such as sepsis, limb amputation, or death [6].

A collection of recent studies have shed light on the remarkably complex roles that immune cells [7], [8], growth factors and cytokines [9]–[11], cutaneous cells [9], [12], [13], proteases [14], [15], and biofilms [15], [16] play in chronic wounds. Despite these advances, it has remained a challenge to develop clinical therapies that improve outcomes for chronic wound patients. This can in part be attributed to the complexity of chronic wounds which tends to render therapies that target a single characteristic of chronic wounds ineffective. Additionally, pre-clinical testing of new wound healing therapies in animals is complicated by high expenses, a justified inclination to minimize the number of animals used, and interspecies differences which reduce the relevance of *in vivo* studies [17].

To overcome many of the limitations of animal models, tissue-engineered skin models have been developed to enable *in vitro* testing of human skin. Applications of these skin models for chronic wounds are twofold; they allow for high-throughput testing of potential therapeutics in a realistic environment and also can be used to gain further insight on the complex mechanisms that prevent chronic wounds from healing. Despite this potential, tissue-engineered skin has seldom been used to study chronic wounds.

This thesis will explore the clinical need, design, verification, and use of a tissue-engineered human skin model to study chronic wounds *in vitro*. First, the anatomy of human skin, physiology of normal and chronic wound healing, and existing *in vitro* models of chronic wounds will be discussed. The benefits and limitations of a variety of biomaterials for tissue engineering will be deliberated and a suitable material and biofabrication approach will eventually be chosen and justified. The design and experimental characterization of a tissue-engineered skin model will then be presented with an emphasis on how the biofabrication protocol was optimized to provide a favourable dermal microenvironment and a stratified epidermal layer. The mature tissue-engineered skin will be compared to human skin in order to verify its similar structure and function. Finally, the healing of an infected wound in the tissue-engineered skin will be investigated to evaluate its suitability for mimicking the chronic wound environment.

1.1 Anatomy of Human Skin

Human skin is the interface between the interior of the body and its external environment. Consequently, one of the primary functions of skin is to act as a barrier which prevents water and nutrient loss and simultaneously blocks the ingress of pathogens, toxins, and radiation. Skin also has many other diverse functions including regulating temperature, providing sensation, and recognizing infections [18]. Structurally, skin can be divided into the epidermis and dermis which both sit above a subcutaneous layer (Fig. 1-1 A). The epidermis consists of mostly keratinocytes with little ECM and can be further subdivided into 4 layers in most parts of the body (Fig 1-1 B).

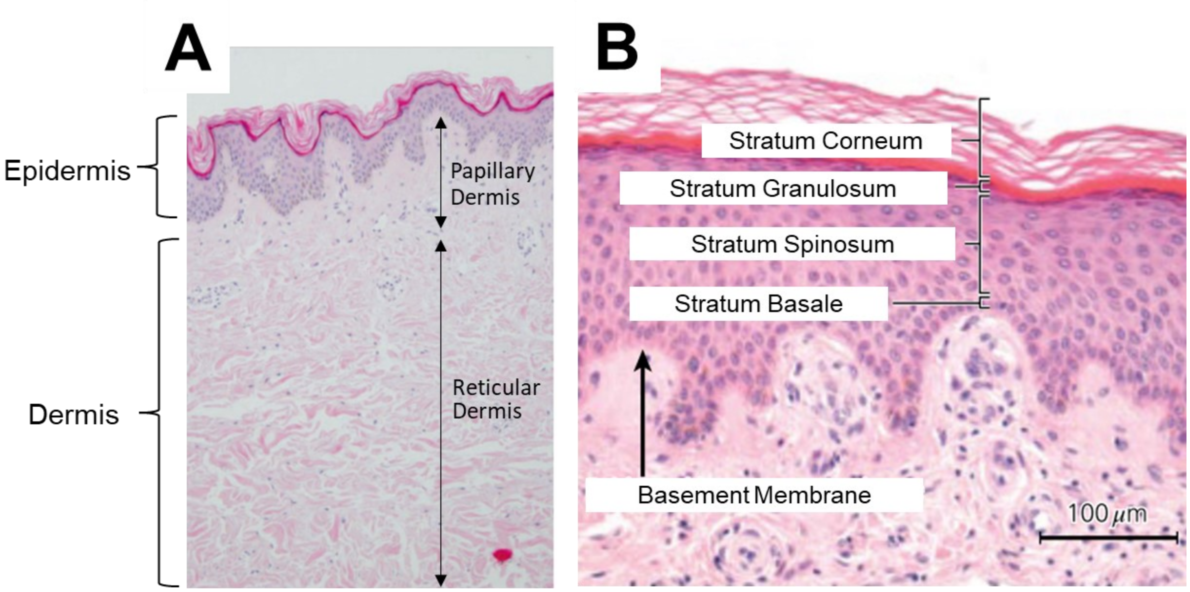

Figure 1-1: (A) Anatomy of the epidermis and dermis (adapted with permission from [19]). (B) Layers of the epidermis (reproduced with permission [19]).

All keratinocytes in the epidermis are products of cell division in the deepest epidermal layer, called the basal layer or stratum basale [18]. Keratinocytes mature and undergo significant structural and morphological changes as they are pushed farther from the basal layer by its persistent cell divisions. The basal layer consists of a single layer of keratinocytes which are firmly attached to the basement membrane. Next is the stratum spinosum, or suprabasal layer, which is comprised of keratinocytes with a polygonal, or slightly flattened, morphology. Desmosomes connect the intracellular keratin filaments of adjacent keratinocytes to give these cells their spiny appearance and this layer its name [18]. In the stratum granulosum, or granular layer, keratinocytes have an even more flattened morphology and are filled with keratohyalin and lamellar granules which contain pro-filaggrin and lipids respectively (Fig 1-2). As keratinocytes further mature and enter the stratum corneum, or horny layer, they undergo apoptosis, lose their nuclei, and release their intracellular granules. Mature filaggrin aggregates keratin fibers in the lower part of the stratum corneum to form a distinct intracellular keratin pattern in corneocytes, cells of the stratum corneum (Fig. 1-2). A strong, insoluble cornified envelope forms on the borders of corneocytes where the structural proteins loricrin and involucrin are crosslinked by transglutaminases. Ceramides and other lipids released from lamellar granules fill the intercellular spaces between corneocytes in the stratum corneum. The combination of the cornified envelope and intercellular lipids act as a tight barrier which prevents water from passing through the stratum corneum. On the superficial edge of the stratum corneum, lipases and proteases reduce the adhesion between keratinocytes which causes them to gradually flake off, or exfoliate.

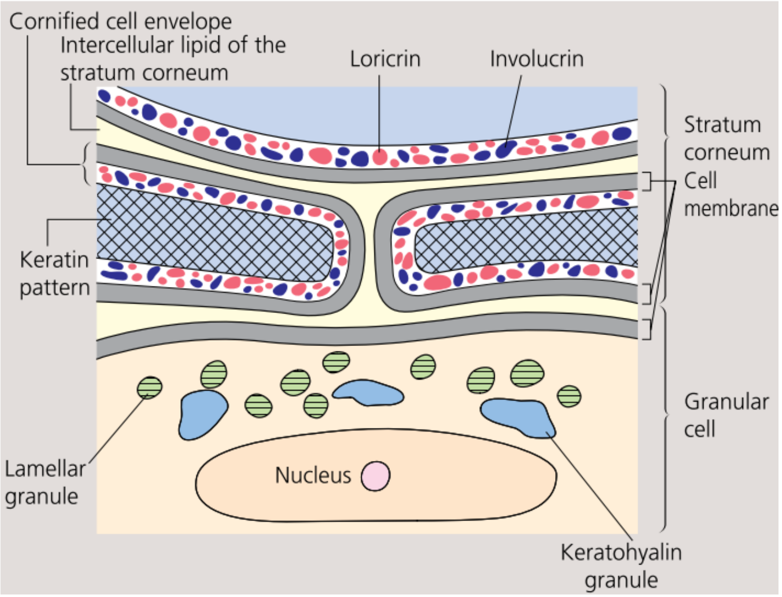

Figure 1-2: Diagram of the cornified envelope and upper stratum granulosum (reproduced with permission [18]).

The dermis sits below the epidermis and is much thicker, typically 1-4 mm depending on the location in the body. Dermal papilla project up from the dermis to form a wave-like interface with the epidermis. A thin, two-dimensional sheet of basement membrane comprises the actual dermo-epidermal junction (DEJ). The basement membrane is a dense two-dimensional (2D) network of fibronectin, laminin, collagen IV, and heparin sulphate fibers that together form a sheet which strongly binds basal keratinocytes. Unlike the epidermis, the dermis mostly consists of ECM and is sparsely populated by cells. Thick bundles of collagen I and III fibers are the primary structural components of the dermis (Fig. 1-1 A). Elastin fibers, proteoglycans, and glycosaminoglycans (GAGs) are also common and provide elasticity and strength in compression. The glycoprotein fibronectin is crucial for integrin-mediated cell binding to collagen, fibrin, or heparin. Fibroblasts are the major cell type found in the dermis and in healthy skin they function to build and maintain the ECM network. Other resident cells of the dermis include: mast cells, which can activate the immune system; endothelial cells and pericytes, which surround blood vessels; and neurons which transmit signals of sensation or pain to the central nervous system. The dermis can be subdivided into the papillary and reticular dermis (Fig. 1-1 A). The papillary dermis sits immediately below the epidermis, has thinner collagen fibers, and contains many blood vessels and nerve endings. The reticular dermis, on the contrary, is located deeper than the papillary layer and contains significantly thicker collagen fibers (Fig. 1-1 A). Skin appendages such as sweat glands, hair follicles, and sebaceous glands originate in the dermis and protrude through the epidermis to reach the skin's surface. Similar to the nomenclature used for skin grafts, full-thickness will be used to refer to skin that has both a dermis and epidermis.

1.2 The Wound Healing Process

Shallow injuries that only harm the epidermis quickly heal as basal keratinocytes proliferate and mature to restore the structure of the epidermis [20]. Deeper wounds that damage both the dermis and epidermis initiate a complex cascade of events that typically heal the wound.

Haemostasis, the first phase of wound healing, begins immediately after the injury as platelets clot with red blood cells and adjacent blood vessels constrict to prevent further blood loss [19]. After blood loss stops, the inflammatory phase begins (Fig. 1-3). Mast cells in the dermis secrete histamine as they migrate towards the wound site while platelets in the blood clot release platelet-derived growth factor (PDGF), transforming growth factor β (TGFβ) and other growth factors [2], [20]. These pro-inflammatory cytokines attract circulating neutrophils which then migrate through the blood vessel wall in the process of diapedesis. Once in the wound site, neutrophils secrete free radicals and proteases to degrade damaged tissue and kill bacteria; phagocytize bacteria and small tissue fragments; and secrete growth factors to recruit additional leukocytes [1]. Neutrophil presence in the wound peaks after 24 hours and they are gradually replaced by monocytes. Circulating monocytes are attracted to fibrin as well as the many pro-inflammatory cytokines present in the wound site. These cytokines cause monocytes in the wound site to gradually differentiate into macrophages. Neutrophils remaining in the wound begin to undergo apoptosis and many are also either engulfed by macrophages or extruded out of the wound into an accumulation of devitalized tissue on the wound's surface, called slough [2]. By 48 - 72 hours after the injury, macrophages are typically the predominant leukocyte in the wound. Macrophages take over the neutrophils' role of engulfing bacteria and debris as well as begin to secrete a variety of growth factors which stimulate adjacent fibroblasts, keratinocytes, and endothelial cells to produce new, healthy tissue (Fig. 1-3).

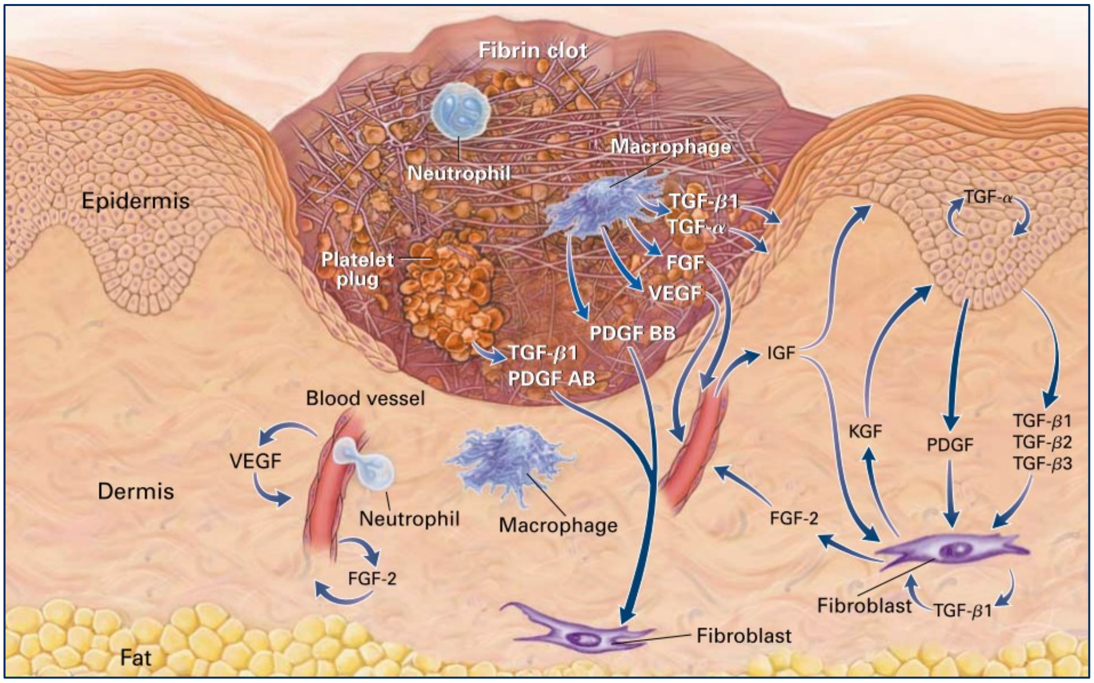

Figure 1-3: Schematic of a wound at the end of the ***inflammatory phase*** *of healing (Reproduced with permission from [2] Copyright Massachusetts Medical Society).*

In the subsequent proliferative stage, cells in the epidermis and dermis begin to proliferate and the wound closes through a combination of reepithelialisation, ECM accumulation, and wound contraction (Fig. 1-4). Growth factors secreted by macrophages such as VEGF, PDGF, bFGF, and

KGF are essential to initiate and drive this process. VEGF and bFGF (FGF7) act on endothelial cells to increase vascular permeability and stimulate angiogenesis in the wound bed [2], [19]. PDGF from macrophages or platelets and IGF from endothelial cells both stimulate fibroblasts to migrate into the wound and proliferate [2], [10]. These fibroblasts deposit new ECM which forms granulation tissue in the wound bed. The fibroblasts strike a delicate balance between secreting matrix metalloproteases (MMPs) to degrade the fibrin clot and secreting tissue inhibitors of matrix proteases (TIMPs) which inhibit the action of MMPs. Additionally, the fibroblasts secrete KGF (FGF7) which causes keratinocytes on the borders of the wound to proliferate, migrate into the wound, and reform the epidermis. During the proliferation phase, a population of fibroblasts differentiate into a myofibroblast phenotype which then contract to physically pull together the edges of the wound [12].

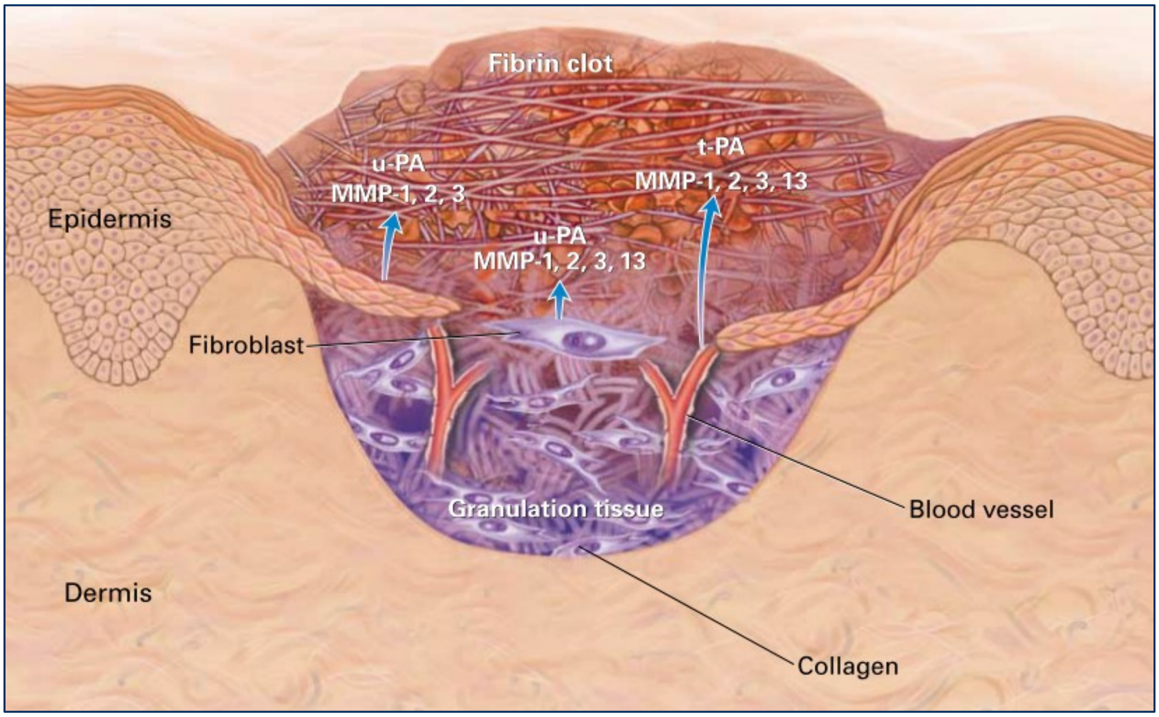

Figure 1-4: Schematic of a wound near the end of the ***proliferative phase*** *of healing (Reproduced with permission from [2] Copyright Massachusetts Medical Society).*

Following the closure of the wound and reepithelialisation, the wound enters a phase of remodelling or maturation. In this phase, collagen fibers in the dermis are remodelled as fibroblasts continue to synthesize collagen and secrete MMPs. Over time, collagen fibers grow in diameter and covalently crosslink together into a complex network. Three weeks after the injury, the regenerated skin has only 20% the strength of the initial tissue, however, this eventually increases to 70% of the initial strength due to the prolonged remodelling process [2].

1.3 Chronic Wounds

In some cases, wounds do not progress normally through the phases of wound healing and are referred to as chronic or non-healing wounds. Underlying conditions that are risk factors for chronic wounds include atheroschlerosis, the build-up of arterial plaque; venous insufficiency, the inability for veins in the lower body to return blood to the heart; or neuropathy, nerve damage causing a lack of feeling or numbness that often results from diabetes mellitus [1], [20]. Clinical care of chronic wounds can include a combination of debridement, topical or systemic antimicrobials, a moist dressing, skin grafting, off-loading, and pain management depending on the wound etiology and current state of healing [2]. Extensive clinical studies on chronic wounds have provided valuable information on how the biochemical environment of chronic wounds compares with that of healing wounds (Table 1-1). The concentrations of influential growth factors are imbalanced in chronic wounds in comparison with healing wounds [11], [21]. Particularly, the levels of pro-inflammatory cytokines are higher and remain elevated for an extended period. This may be caused by the abnormal accumulation and persistence of neutrophils in the wound which secrete the pro-inflammatory cytokines interleukin-1β (Il-1β) and tumor necrosis factor-α (TNF-α) [11]. Moreover, the presence of excessive bacteria in chronic wounds can also cause an extended period of inflammation. High concentrations of proteases in chronic wounds have detrimental effects on the production of new ECM [22] and also quickly degrade peptide growth factors before they can stimulate cell proliferation [23]. Fibroblasts cultured *in vitro* with exudate from chronic wounds were senescent while those cultured in exudate from healing wound were highly proliferative [21], which can partially explain why chronic wounds struggle to produce new ECM and healthy granulation tissue. Collectively, this evidence indicates that chronic wounds are trapped in an inflammatory state and struggle to progress to the proliferative phase of healing.

Table 1-1: Comparison between healing wounds and chronic wounds.

	Healing Wounds	Chronic Wounds
Cytokine/Growth Factor Milieu	Baseline	↑ pro-inflammatory cytokines [11], [22]
Concentrations of proteases and their inhibitors	Baseline	↑ MMPs [22], [24] ↓ TIMPs [11], [22]
Presence of bacteria	Low levels	High levels of bacteria and/or biofilm formation [1], [25], [26]
Number and type of leukocytes present	Baseline	↑ neutrophils [20], [27]
Fibroblast phenotype	Proliferative	Senescent [21]

One plausible reasoning for the persistent inflammation in chronic wounds is that the high prevalence of bacteria drives a continuous cycle of inflammation and immune activation which fails to remove the infection and also stalls the progression out of the inflammatory phase. In general, bacteria in wounds can exist in either a planktonic state or as a biofilm. Planktonic bacteria are individuals that have adhered to a solid substrate while biofilms are characterized by a large number of closely adjacent bacteria with a thick protective coating of extracellular polymeric substances (EPS) including polysaccharides, lipids, and proteins (Fig. 1-5) [15], [26]. All wounds likely contain a variety of planktonic bacteria; however, in chronic wounds bacteria have frequently colonized much of the wound and formed a biofilm. This is exemplified by the findings of James *et al.* that biofilms are found in 60% of chronic wounds and only 6% of healing wounds [25]. The presence of devitalized tissue and low oxygen tension in chronic wounds provides planktonic bacteria with favourable conditions to proliferate. As the bacteria increase in number, molecular pathways and secondary messenger cascades are initiated which can induce the formation of a biofilm (Fig. 1-5) [26]. The matrix of EPS helps coordinate the spatial organization of the bacterial community and provides protection from physical disruption, antibacterials, and host neutrophils [28]. Biofilms are difficult to diagnose on chronic wounds as they are usually less than 100 µm thick and macroscopically appear similar to slough, exudate, or debris [26]. Antimicrobial hydrogel dressings have been proposed as a treatment for chronic wounds to reduce bacterial colonization [29]. However, even if this approach is successful at preventing biofilm formation, it does not address the many other differences between chronic and healing wounds which also act as a barrier to healing.

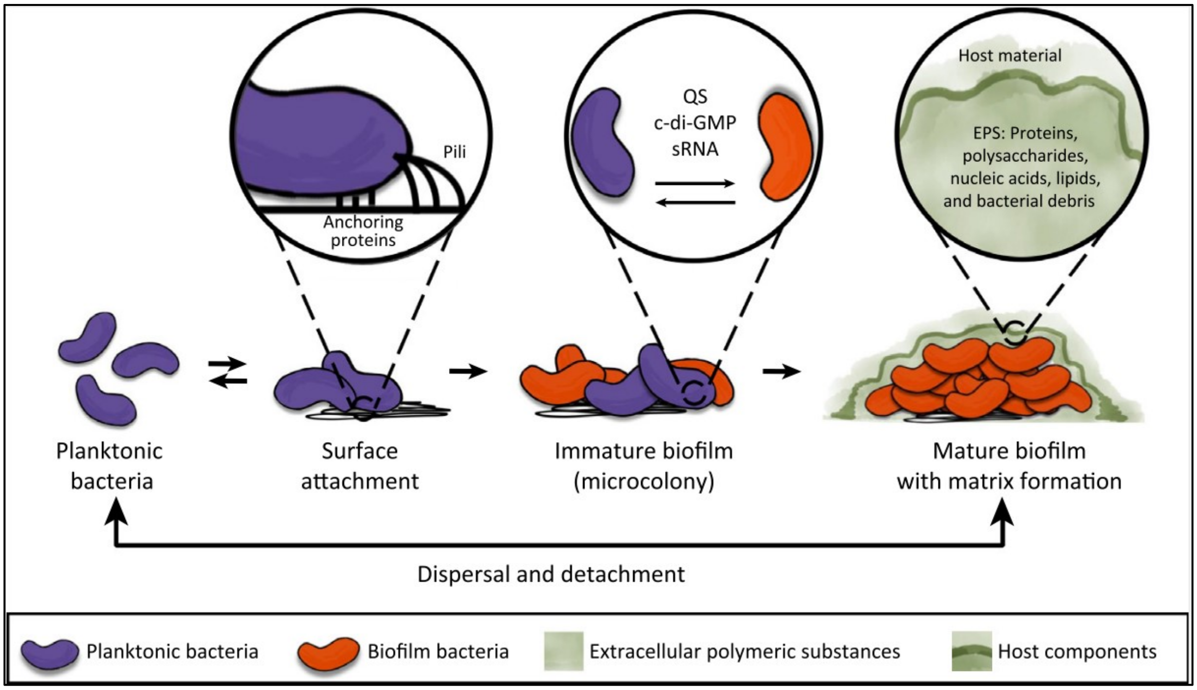

Figure 1-5: The process of biofilm formation by planktonic bacteria (reproduced with permission [26]).

It is difficult to attribute the non-healing of chronic wounds to a single factor and it is likely that the collective interplay between many or all of these factors act to inhibit healing in chronic wounds. Pre-clinical and clinical trials of topical growth factor therapies for chronic wounds have mostly proven unsuccessful [30], [31]. This is potentially due to the treatment approach of topically applying a single growth factor when the well-tuned collective action of dozens of growth factors contributes to healing in healthy wounds. Additionally, the high concentration of proteases in chronic wounds may degrade exogenous growth factors before they can exert a positive influence.

Despite decades of extensive research on chronic wounds, the standard clinical treatment still frequently leads to adverse outcome such as amputation. This is aptly summarized by Ken *et al.*'s call to action: "the immense economic and social impact of wounds in our society calls for allocation of a higher level of attention and resources" [32]. The primary focus of almost all published studies on chronic wounds has been either to elucidate further information on the chronic wound environment or to test a potential therapy on a simplified *in vitro* model, *in vivo*, or in a clinical trial. The desire to reduce the number of animals used for *in vivo* studies makes it unfeasible to systemically test a wide variety of potential chronic wound treatments with animals. Furthermore, *in vivo* studies are expensive and their results are complicated by the interspecies biological differences between humans and animals [17]. On the other end of the spectrum, while *in vitro* studies are relatively cheap and easy to perform, they do not mimic many aspects of the chronic wound environment. For example, antibacterial wound dressings are often evaluated *in vitro* by placing the dressing on an agar plate colonized with *Staphylococcus. aureus* (*S. aereus*) or *Pseudomonas aeruginosa* (*P. aeruginosa*) and the zone of bacterial inhibition is observed [33], [34]. While useful for evaluating antibacterial properties, such studies do not account for the heterogenous bacteria population and potential biofilms found in chronic wounds. Additionally, they cannot provide an indicator of how the potential therapy will affect reepithelialisation, ECM deposition, or wound closure as cutaneous cells are not present. An *in vitro* model of the chronic wound environment which can mimic bacterial colonization, reepithelialisation, ECM deposition, and the host immune response would represent a crucial step forward in the goal of developing more effective clinical therapies for chronic wounds.

1.4 Tissue-Engineered Skin Models

Tissue-engineered skin would be a suitable *in vitro* platform for testing new chronic wound therapies. Many examples of tissue-engineered skin currently exist with varying degrees of complexity from a simple coculture of keratinocytes growing on a fibroblast-laden collagen gel that was first introduced in the 1980s [35], to complex skin tissues with vasculature [36], [37], immune functionality [38], or rete ridges [39]. The most common approach for creating engineered-skin *in vitro* is to first create a dermal layer consisting of fibroblasts encapsulated in a biocompatible hydrogel such as collagen [40], [41], GelMA [42], [43], or fibrin [44]. The dermal layer is commonly fabricated by extrusion bioprinting [37], [40], [42], [45] or micromolding [39], [43]. Keratinocytes are then deposited on the top surface of the dermal layer and cultured at the air-liquid-interface (ALI) until a mature stratum corneum has formed (Fig. 1-6). Satisfactory maturation of keratinocytes in tissue-engineered skin is usually verified by histology and immunohistochemistry (IHC) which show the structural morphology of the epidermis and its proteins expression patterns respectively. Hematoxylin & eosin (H&E) is the most common histological stain and it is very useful for evaluating if an orderly epidermis with flattened keratinocytes in the stratum granulosum and stratum corneum has formed (Fig. 1-6 A, B). Proteins such as keratin 5 or 14 (Fig. 1-6 C, D), and laminin (Fig. 1-6 E, F) are used as markers of the stratum basale and basement membrane respectively. Significant expression of involucrin, loricrin, and filaggrin (Fig. 1-6 E, F) should be seen in the stratum corneum. In tissue-engineered skin, poor keratinocyte maturation or unexpected patterns of protein expression in the epidermis can be caused by factors such as lack of air exposure, growth factor imbalance, or insufficient maturation time. This is exemplified by Fig. 1-6 D which shows disorganized staining of keratin 14 that should only be expressed by basal keratinocytes (Fig. 1-6 C). The intricacies of IHC analysis are highlighted in Figure 1-6 E, F which show the differences between staining human skin with a pan-specific laminin antibody (Fig. 1-6 E) and mature tissue-engineered skin with a laminin 511-specific antibody (Fig. 1-6 F).

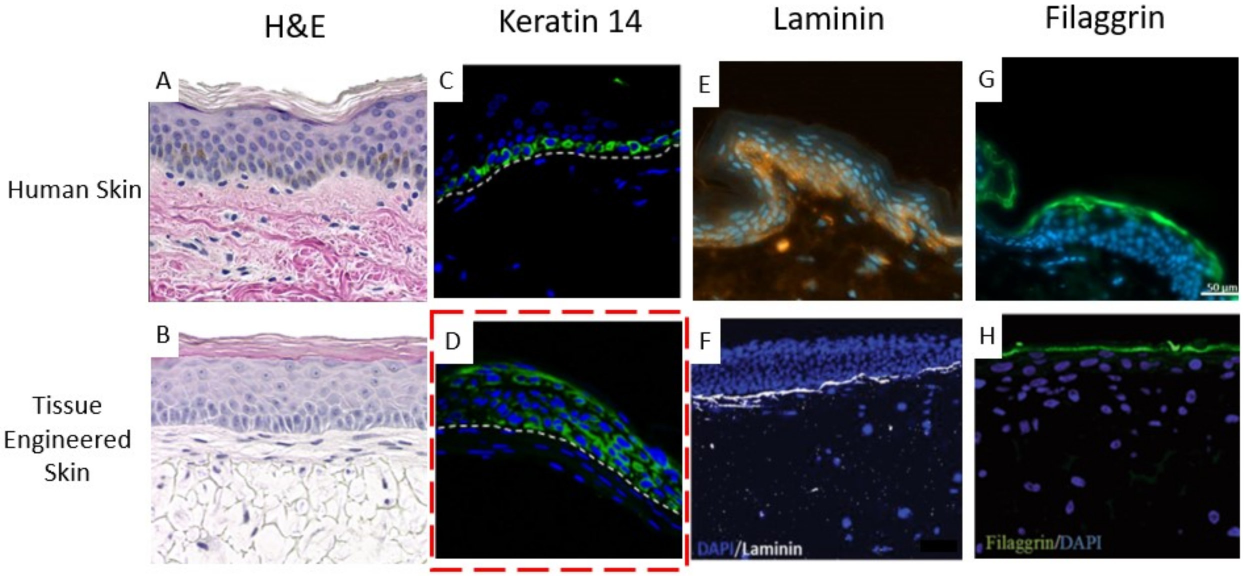

Figure 1-6: Comparison of human skin (A, C, E, G) with various examples of tissue-engineered skin (B, D, F, H). Tissue-engineered skin models included a polystyrene scaffold (B, H), casted plasma hydrogel (D), and bioprinted hybrid hydrogel (F). Keratin (C, D) and filaggrin (G, H) are shown in green, and laminin is shown in orange in human skin (E) and white in the example of tissue-engineered skin (F). In all IHC images (C-H) the nuclei are counterstained in blue. A, B, H reproduced with permission [46]; C, D reproduced with permission [47]; F reproduced with permission [37].

Despite the existence of many sophisticated tissue-engineered skin models, relatively few have been used to study chronic wounds *in vitro*. This criticism is supported by the comprehensive review of *in vitro* platforms for studying chronic wounds by Kadam *et al.* in 2020 which categorized all existing *in vitro* models of chronic wounds into four categories: microbes + cutaneous cells, microbes + immune cells, microbes + ECM, and microbes + wound fluid (adapted in Table 1-2) [48]. Notably, there were no models of chronic wounds that concurrently included damaged human skin, infection, and immune cells. Most of the models that included cutaneous cells and infection were rudimentary. Of all the existing *in vitro* chronic wound models, the wounded tissue-engineered skin developed by Manuela *et al.* is arguably the most biologically relevant [49]. Using a tissue-engineered human skin model that included an epidermis and fibroblast-laden dermis, this study observed the reepithelialisation of a biopsy punched wound that was filled with a collagen hydrogel. During healing process, the tissue-engineered skin was submerged in fluid taken from a chronic wound or in media as a control (Fig. 1-7A) [49]. This experimental approach made it possible to observe how the cytokines and proteases in chronic wound exudate affect reepithelialisation and fibroblast phenotype *in vitro*. However, the model did not include bacteria or immune cells and the epidermis did not have a mature stratum corneum as it was not cultured at the ALI. Another study of note is Jahanshahi *et al.'s* infected epidermis model which evaluated the reepithelialisation of an infected epidermal scratch with and without antibiotics (Fig. 1-7 B) [50]. Interestingly, this model featured a hollow channel that snaked through the gelatin hydrogel and was used to provide nutrients by perfusion; however, the channel had no endothelium. Other limitations of this model include its shallow wound and the exclusion of dermal fibroblasts and immune cells.

Table 1-2: Existing in vitro models of chronic wounds.

	Author	Bacteria	Cutaneous Cells	Immune Cells	Substrate	Exudate	Year	Ref.
Infection + cutaneous cells	Alves *et al.*	*S. aureus,* *P. aeruginosa*	Keratinocytes				2018	[51]
	Tankersley *et al.*	*S. aureus*	Keratinocytes				2014	[52]
	Jahanshahi *et al.*	*E. coli*	Keratinocytes		Gelatin		2020	[50]
Infection + immune cells	Ellett *et al.*	*S. aureus*		Neutrophils			2019	[53]
	Hauser *et al.*	*P. aeruginosa*		Macrophages			1999	[54]
Infection + ECM	Werthen *et al.*	*S. aureus,* *P. aeruginosa*			Collagen I		2010	[55]
	Price *et al.*	*S. aureus,* *P. aeruginosa*			Collagen I		2016	[56]
Cutaneous cells + exudate	Manuela *et al.*		Keratinocytes, Fibroblasts		Collagen I	Acute and chronic	2017	[49]

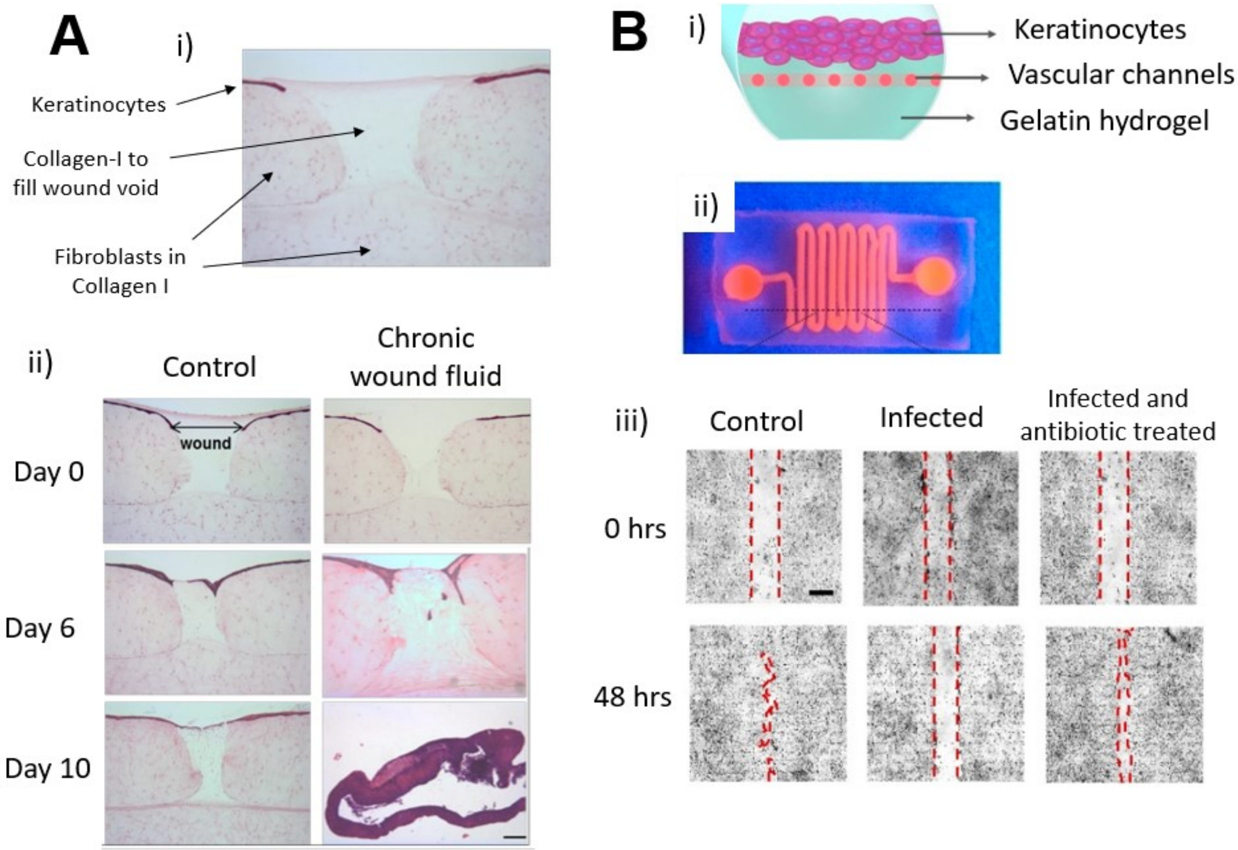

Figure 1-7: The most biologically relevant in vitro chronic wounds models. (A) Tissue-engineered human skin that was artificially wounded (i) to study reepithelialisation in the presence of chronic wound fluid (ii) (creative commons attribution license [49]). (B) A human epidermis above a perfusable channel (i,ii) that was scratched, infected, and treated with antibiotics to study reepithelialisation (iii) (creative commons attribution license [50]).

After considering many of the existing *in vitro* models of chronic wounds, it is clear that all are missing important aspects of the chronic wound environment. Neither Manuela *et al.* or Jahanshahi *et al.* included immune cells, which play a central role in chronic wounds. At a minimum, for an *in vitro* chronic wound model to adequately mimic the *in vivo* situation it should include damaged human skin, infection, and immune cells. Kadam *et al.'s* review goes even further with its description of the ideal *in vitro* chronic wound model, calling for vasculature and mechanical stimulus in addition to the aforementioned factors [48]. To create such an *in vitro* model, it is crucial to begin with tissue-engineered skin that is similar to human skin and is suitable for infection studies. It should be possible to artificially create physical wounds in the tissue-engineered skin. The biomaterials and biofabrication technique used to create the tissue-engineered skin must both be carefully chosen with these constraints in mind.

1.5 Natural Hydrogels and Gelatin Methacryloyl

A limited assortment of the proteins, glycosaminoglycans, and polysaccharides found in humans and animals form hydrogels when isolated and dissolved in water. These natural hydrogels are often used for tissue engineering applications to provide cells with a similar biochemical environment as is found in the ECM of native tissues. Many of the natural hydrogels derived from ECM proteins, such as collagen I, laminin, and fibronectin, promote cell adhesion and exhibit minimal cytotoxicity *in vitro* [57]–[59]. As natural hydrogels degrade, their chemical by-products are typically neither cytotoxic nor inflammatory [60]. One of the major drawbacks of using natural hydrogels for tissue engineering is that the biofabrication of complex three-dimensional (3D) structures can be challenging. Tissue-engineered hydrogel structures are typically fabricated via a crosslinking reaction in which the polymeric chains in the liquid hydrogel crosslink with one another, forming a viscoelastic solid. Natural ECM-derived hydrogels such as collagen I and gelatin crosslink through a thermal mechanism which is slow and difficult to control spatially. This is further complicated by the limited mechanical strength of many natural hydrogels which can cause small features to fracture during or after fabrication [61]. As an exception to the pattern of most natural hydrogels possessing these undesirable properties, alginate is a polysaccharide derived from algae which quickly crosslinks to form a stable gel in the presence of divalent cations. However, alginate lacks cell attachment motifs and also does not replicate the biochemistry of human ECM, limiting its suitability for creating human tissues *in vitro*.

Collagen I is a fibrous protein with a triple helix structure that is the majority component of the ECM in most human tissues [58]. Purified collagen I from animal sources is commonly used for creating tissue-engineered skin [40], [42], [62], cardiac tissue [63]–[65], and neural tissue [66]. GFOGER (O = hydroxyproline) motifs that promote cell attachment to β_1-containing integrins are present throughout the collagen I helix which enables cells to attach to collagen gels *in vitro* [67], [68]. As collagen I accurately replicates the biochemistry of the *in vivo* microenvironment, primary cells laden in collagen I hydrogels *in vitro* generally have high viabilities and similar phenotypes to their *in vivo* counterparts. Despite these advantages, collagen I has similar shortcomings as other natural hydrogels, namely a slow thermal crosslinking mechanism and a weak mechanical strength.

Gelatin is a natural hydrogel obtained from denaturing collagen through heat-mediated hydrolysis of the crosslinks maintaining its triple helix structure [69]. As a result of this process, gelatin still has a similar chemical composition to collagen I but has a much-changed quaternary structure of disorganized polypeptide coils in contrast to the original triple-helix. Gelatin also retains the property of cell attachment, though now primarily mediated by integrin binding to arginine-glycine-aspartic acid (RGD) motifs in its polypeptide backbone [67]. When cooled below the concentration-dependant critical temperature of 26-31°C, gelatin is a solid due to physical crosslinking between chains while at temperatures above, it melts into a shear-thinning liquid [70]. Although challenging to use alone in most cases, gelatin is often combined with other hydrogels [71], [72], enzymatically crosslinked [50], or chemically functionalized into gelatin methacryloyl (GelMA) to enable photo-crosslinking [73], [74].

Of these approaches, GelMA has been widely adopted as one of the most popular biomaterials in tissue engineering due its suitable and tunable mechanical properties, the high degree of spatial control over the photo-crosslinking reaction, and its cell adhesive properties [73], [75]. GelMA is synthesized by a reaction with gelatin and methacrylic anhydride in which methacrylamide or methacrylate groups bind to amino or hydroxyl groups on gelatin respectively (Fig. 1-8). Approximately 5% of gelatin's amino acids have free amino groups (lysine and hydroxylysine), while residues with hydroxyl groups such as serine, threonine, tyrosine, and hydroxyproline make up another 19% [76], [77]. The GelMA synthesis reaction heavily favors the formation of methacrylamide modifications with a methacrylamide:methacrylate ratio of 9:1 in the final GelMA polymer [76]. As the majority of the substitution reaction occurs at amino groups, the degree of functionalization (DoF) of GelMA polymers can be defined as the percentage of the original amino groups that are later occupied by methacrylamide. By adjusting the volume of methacrylic anhydride added per weight gelatin from 1% to 8% (v/w), the DoF of the resulting GelMA polymer can be tuned. Most commonly, 6-8% (v/w) methacrylic anhydride is used which results in a high DoF (75% to 85%) and produces crosslinked gels with higher mechanical strengths than lower degrees of functionalization [74], [76], [78].

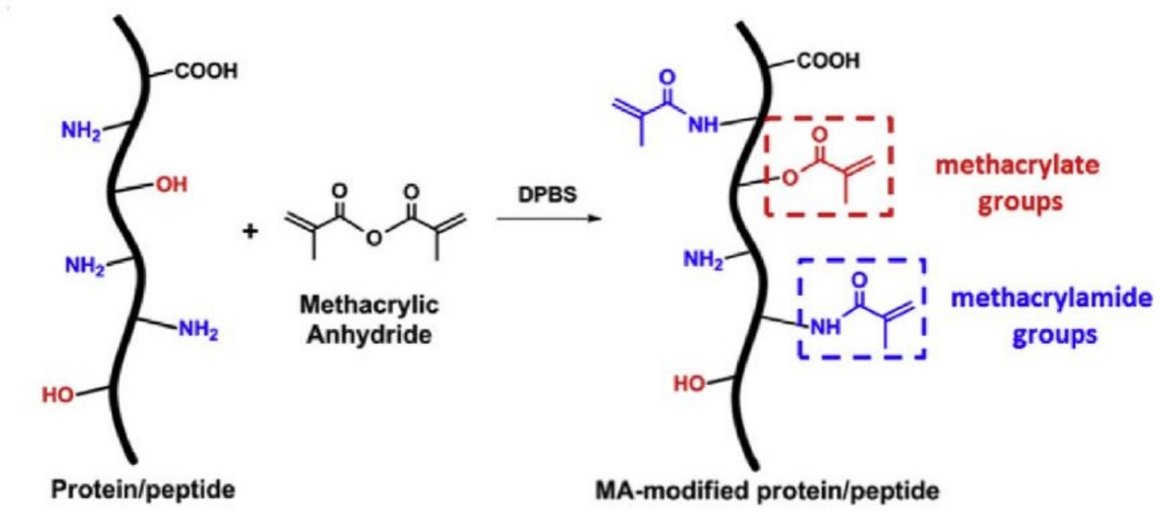

Figure 1-8: Synthesis of GelMA through the reaction of gelatin with methacrylic anhydride (MA) (reproduced with permission [76]).

The morphology of cells encapsulated within a non-toxic hydrogel depends on the presence or absence of cell binding motifs, the intrinsic pore size of the matrix, and the stiffness of the matrix. A major benefit of using GelMA to produce cell-laden tissues is that it has cell binding motifs (RGD) and both the pore size and stiffness of the matrix can be tuned. Many studies have demonstrated that GelMA with a higher DoF forms a stiffer gel with smaller microscale pores (Fig. 1-9A) [79]–[81]. After the GelMA synthesis reaction, the solution is lyophilized (freeze-dried) and then dissolved in an aqueous solution for use. Dissolving GelMA at higher concentrations has also been shown to also produce gels that are stiffer and contain smaller microscale pores (Fig. 1-9 B) [79]–[81].

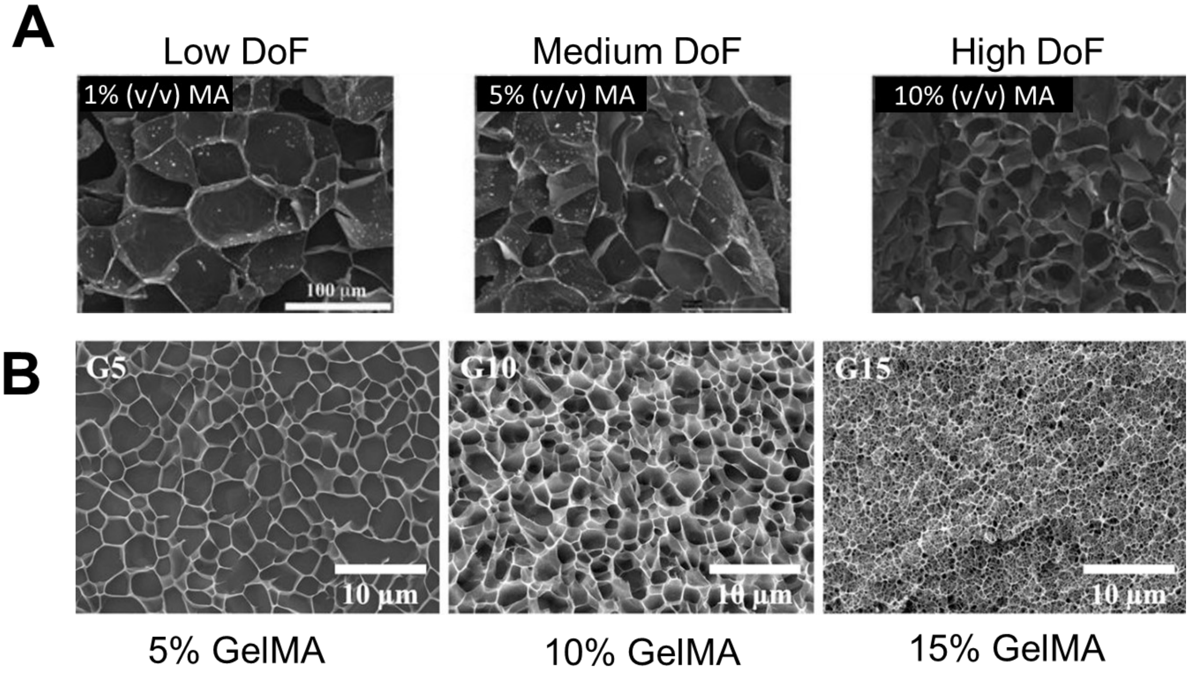

Figure 1-9: Influence of DoF (reproduced with permission [79]) and GelMA concentration (creative commons attribution license [82]) on the microporosity of the crosslinked hydrogel. Note the discrepancy in scale between A and B.

In a cell-laden hydrogel, filopodia extent from the cell body into the pores within the hydrogel matrix in search of attachment sites [83]. Relatively small pores inhibit the penetration of filopodia while larger pores enable deeper ingression. Proteases secreted by mesenchymal cells are capable of locally degrading the GelMA matrix [57] which allows for further extension of filopodia or lamellipodia and even cell migration within the hydrogel. Many studies have shown that fibroblasts suspended in 5% (w/v) GelMA adopt a highly spread morphology similar to what is seen *in vivo* (Fig. 1-10 A, B) [36], [82]. On the contrary, in higher concentrations of GelMA such as 10 or 15% (w/v) the same cells have a round morphology with much smaller projections (Fig. 1-10) [36], [82]. As cell morphology is correlated to patterns of gene expression [84], maintaining a spread fibroblast morphology *in vitro* is crucial for mimicking the natural behavior of these cells in both healthy and chronic wound models.

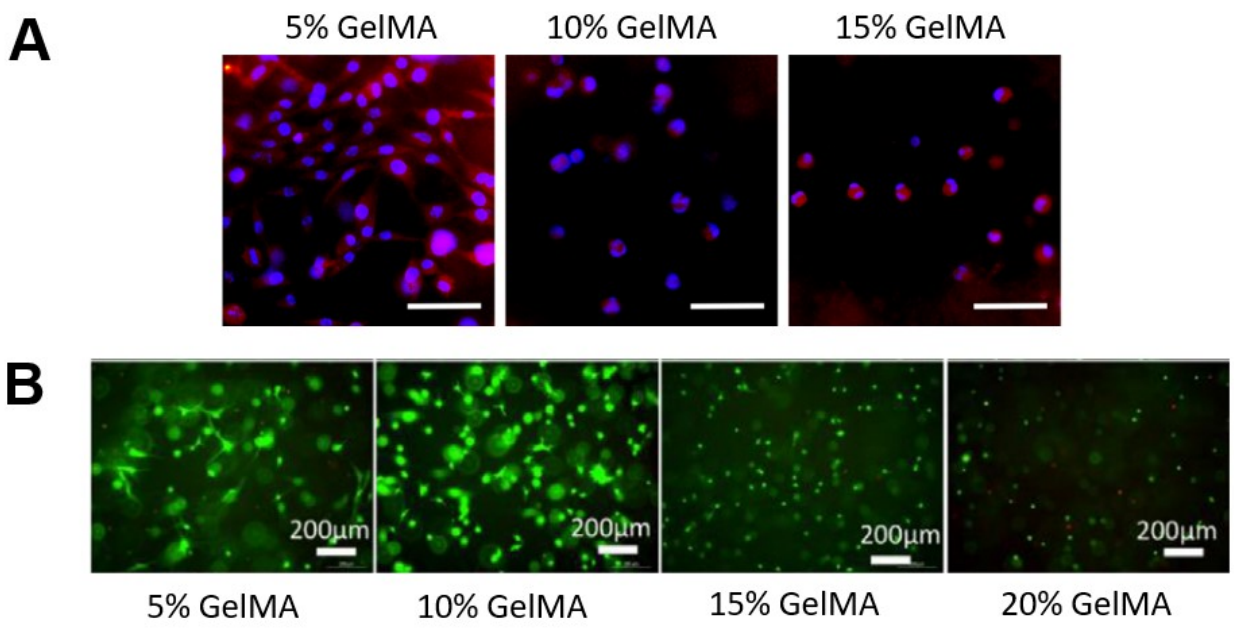

Figure 1-10: (A) F-actin staining of human dermal fibroblasts after 7 days in culture encapsulated in GelMA hydrogels (scale bar = 200 µm, creative commons attribution license [82]). (B) Live and dead staining of human neonatal dermal fibroblasts after 3 days of culture encapsulated in GelMA hydrogels (reproduced with permission [36]).

1.6 Extrusion and DLP Bioprinting

The analysis of cell morphology within GelMA hydrogels shows the benefits of using low concentrations of GelMA. In extrusion bioprinting, a syringe usually loaded with a biocompatible hydrogel is mounted on a 3-axis motorized stage and the hydrogel is slowly extruded out of a needle by a pneumatic or syringe pump [45], [71], [78]. The tip of the needle moves around the build area to produce the desired shape as instructed by a computer aided design (CAD) file. With this approach, the bioprinted gel must maintain its shape in order for the resolution and features to be maintained; however, this is challenging to implement with low concentrations of GelMA due to the relatively weak mechanical properties and slow crosslinking. The extrusion process also introduces shear stresses which are harmful for living cells [78], [85]. The resolution of extrusion bioprinting is limited by the inner diameter of the extrusion needle, and problematically, as the needle diameter is decreased to improve resolution the shear stress increases which reduces the viability of bioprinted cells [85]. For reference, extrusion bioprinting with a 27G needle (inner diameter of 210 μm) has shown suitable cell viability and would be considered a reasonably high resolution for extrusion bioprinting [85], [86]. Many innovative solutions for extrusion bioprinting low concentrations of GelMA have been proposed such as a coaxial mechanical support [86], microfluidic flow focussing [87], and combining GelMA with other materials [45], [71], [72] but these have gained minimal traction mostly due to their complex biofabrication procedures.

A much simpler biofabrication technique to implement called digital light processing (DLP) bioprinting has recently emerged as a practical solution for creating engineered tissues with high resolutions using low concentrations of GelMA or other photo-crosslinkable hydrogels. Following an array of publications describing custom-made DLP bioprinters and their applications [88]–[91], a commercial DLP bioprinter called the Lumen-X was released by Cellink (Sweden) in 2020. DLP bioprinters use a light-source and digital-micromirror-device to project an image through a transparent vat and onto the build platform where the part forms (Fig. 1-11). Each pixel in the image can be selectively turned on or off by the software. For each layer, the corresponding image is projected for a set duration, the build platform translates incrementally away from the projector, and then the image for the next layer is projected. This process continues until the entire part has been produced as specified by the original CAD file provided to the device. There is minimal shear stress in the hydrogel as there is no applied pressure or small orifice which results in a high viability for DLP bioprinted cells. Additionally, the resolution is only limited by the spatial resolution of the projected image. The Lumen-X has a minimum layer height of 50 μm and projects an array of 1280 x 800 pixels which are each 50 μm x 50 μm, providing a maximum part footprint of 6.4 x 4.0 cm [92]. The projector forms each image with 405 nm light, allowing the Lumen-X to photo-crosslink GelMA without harming living cells encapsulated within the hydrogel.

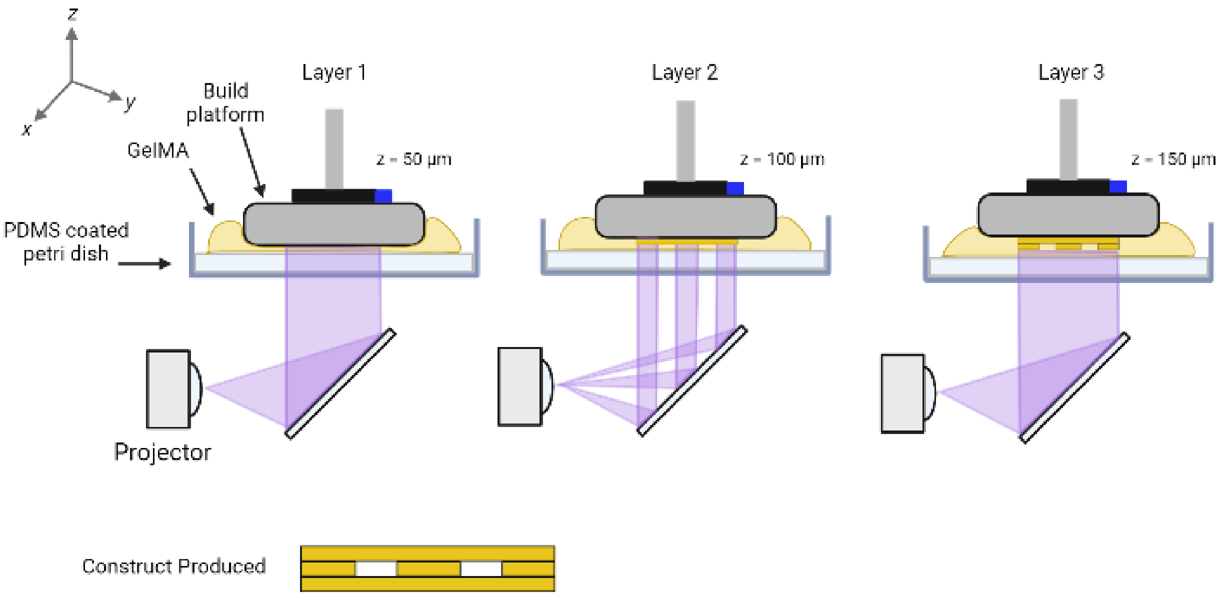

Figure 1-11: Simplified schematic of the DLP bioprinting mechanism. Created with BioRender.com.

1.7 Conclusion and Outlook

The complex interactions in the chronic wound bed between cutaneous cells, bacteria, immune cells, and growth factors/cytokines have made it challenging to introduce new therapeutics for chronic wounds that improve patient outcomes. Tissue-engineered skin can function as a biomimetic *in vitro* testing platform for evaluating potential chronic wound therapies in a controllable environment. The primary goal of this work is to develop a tissue-engineered skin model that is suitable for studying chronic wounds *in vitro*. This goal can be divided into three objectives which have each been dedicated a chapter of this work:

1. develop a tissue-engineered model of the human dermis,

2. develop and verify a full-thickness skin model that includes the dermis and epidermis, and
3. demonstrate that the model can be infected and mimic wound healing *in vitro*.

Initially, the hydrogel and biofabrication process will be optimized to provide a favourable microenvironment for dermal fibroblasts. An epidermal layer will then be added on the top surface of the dermal construct and matured at the ALI. The primary verification of the tissue-engineered skin will be a histological comparison of the epidermal layer with human skin. Patterns of protein expression and electrical resistance will also be compared between the tissue-engineered and human skin. Finally, the epidermis will be wounded then infected and healing will be monitored to establish the usefulness of this *in vitro* model for studying treatments for chronic wounds.

Chapter 2 - Optimization of the Dermal Layer

The dermis provides the majority of the skin's mechanical strength, accounts for almost all of its volume, and can exist *in vitro* independently of an epidermis [18]. In contrast, the epidermis is much thinner and requires a substrate for keratinocyte attachment and stratification. Accordingly, a tissue-engineered dermis will be designed and optimized in this chapter. The epidermis will later be established on the top surface of the dermal constructs and will described and verified in Chapter 3.

As the human dermis is comprised mostly of ECM and sparsely populated with fibroblasts, the logical and widely followed approach for mimicking the dermis *in vitro* is to suspend fibroblasts in a hydrogel that is then crosslinked to form a solid gel [37], [45], [47], [93], [94]. This approach introduces many design parameters such as the hydrogel type and concentration, biofabrication strategy, dermal cell type and cell density, and maturation/culture timeline which all significantly influence the final engineered tissue. The previous discussion of natural hydrogels and biofabrication methods in sections 1.5 and 1.6 respectively led to the decision to DLP bioprint a GelMA hydrogel to form the dermal layer.

The dermal cell type chosen should have a similar phenotype to dermal fibroblasts, be easy to use, and provide reproducible results. Stem cell-derived dermal fibroblasts require a challenging, labour intensive, and often inconsistent differentiation process [95] and offer no benefits over primary fibroblasts which are easily accessible. Thus, primary dermal fibroblasts from a reputable source (ATCC) will be used. The cell density of fibroblasts in the dermal layer should mimic the density of fibroblasts in the human dermis. There should also be a high enough density of fibroblasts to produce a quantity of growth factors capable of inducing differentiation in the epidermal cells. Based on existing tissue-engineered skin models, a concentration of 0.5 x 10^6 fibroblasts per mL was selected (Table 2-1). This decision was also motivated by Schoop *et al.*'s characterization of an epidermis seeded on hydrogels with fibroblast densities ranging from 0.05 to 0.5 x 10^6/mL [93]. Their results showed that 0.5 x 10^6 fibroblasts per mL provided the best organized epidermis after 14 days of culture.

Table 2-1: Fibroblast cell type and densities in tissue-engineered skin models.

Author	Fibroblast Type	Fibroblast Density (per mL)	Year	Ref
Kim *et al.*	Primary Dermal Fibroblasts (Lonza)	0.5 x 10^6	2019	[37]
Baltazar *et al.*	Primary Dermal Neonatal Fibroblasts (collected directly)	0.7 x 10^6	2020	[42]
Abaci *et al.*	Primary Dermal Neonatal Fibroblasts (collected directly)	0.125 x 10^6	2016	[94]
Barros *et al.*	Primary Adult Fibroblasts (ATCC)	8 x 10^6	2020	[45]
Schoop *et al.*	Primary Adult Fibroblasts (collected directly)	0.05 - 0.5 x 10^6	1999	[93]

Next, experiments were performed to verify the suitability of DLP bioprinting GelMA laden with 0.5 x 10^6 fibroblasts/mL for creating a tissue-engineered dermis. The GelMA concentration was also optimized experimentally by evaluating the printability and fibroblast viability, proliferation, and morphology in 5, 7.5, and 10% GelMA.

2.1 Materials and Methods

The following chemicals were purchased from Sigma-Aldrich: phosphate buffered saline (PBS, cat#: P4417), gelatin Type A (cat#: G2500), methacrylic anhydride (cat#276685), 3-(trimethylsilyl)-1-propanesulfonic acid sodium salt (TSP, cat#: A14489.MD), lithium phenyl-2,4,6-trimethylbenzoylphosphinate (LAP, cat#: 900889), tartrazine (cat#: T0388), deuterium oxide (cat#: 151882), bovine serum albumin (BSA, cat#: A1933), and neutral-buffered formalin (NBF, cat#: HT5011).

Dulbecco's Modified Eagle Media (DMEM) with L-glutamine and 4.5g/L glucose (Gibco, cat#: 11965), fetal bovine serum (FBS, Fisher Scientific, cat# 10437), TrypLE Express (Gibco, cat#: 12605), Dulbecco's phosphate buffered saline (DPBS, Gibco, cat#: 14190), Alexa Fluor™ 488 Phalloidin (Invitrogen, A12379), Live/dead viability kit for mammalian cells (Invitrogen, cat# L3224), PrestoBlue cell viability reagent (Invitrogen, cat#: A13262), and 4′,6-diamidino-2-phenylindole (DAPI, Invitrogen, cat#: D1306) were used for cell culture and analysis.

2.1.1 GelMA Synthesis

The protocol for GelMA synthesis was based on published protocols [73], [74] and slightly modified to avoid frequent issues. To begin, 10 g of gelatin was dissolved in 200 mL PBS at room temperature and then heated to 60 ºC with mild stirring. After the gelatin had dissolved to form a clear solution, 8 mL of methacrylic anhydride was added to produce high degree of functionalization (DoF) GelMA. It is crucial to add the methacrylic anhydride in a slow, dropwise manner while vigorously stirring the gelatin solution. If the methacrylic anhydride is added too quickly, the stirring pauses, or the temperature drops, the solution may coagulate into a viscous semi-solid gel which must be discarded and the synthesis procedure should be repeated from the beginning. Once the methacrylic anhydride was added, the solution was protected from light and stirred mildly at 60 ºC for 3 hours. The reaction was then stopped by dilution with 300 mL of PBS pre-warmed to 60 ºC and stirred mildly for 15 minutes. The reaction solution was aliquoted into dialysis membrane tubing and dialysed into distilled water at 45 ºC for 10 days with daily distilled water changes to remove toxic by-products and unreacted methacrylic anhydride. Finally, the dialyzed GelMA solution was filtered with filter paper, frozen at -80 ºC, and then lyophilized for at least 5 days.

2.1.2 ^{1}H NMR Analysis of GelMA Functionalization

Lyophilized GelMA was dissolved in deuterium oxide at a concentration of 0.77% (w/v) and loaded into nuclear magnetic resonance (NMR) tubes. TSP was added as an internal standard. ^{1}H NMR tests were conducted on a Bruker Avance NEO at 500 MHz and data was analyzed using Topspin 4.1.3 (Bruker).

2.1.3 Cell Culture

Primary human neonatal dermal fibroblasts (ATCC® PCS-201-010™) were cultured in DMEM with 10% (v/v) FBS and 100 U/mL penicillin/streptomycin in T25 or T75 flasks. At 90% confluence, fibroblasts were passaged with TrypLE Express and split at a ratio of 1:10. Culture media was changed every third day.

2.1.4 Bioink Cytotoxicity Analysis

The PrestoBlue™ assay uses a resazurin dye that is virtually non-fluorescent until it is reduced to fluorescent resorufin by the reducing environment of viable cells [96]. As non-viable cells or damaged cells cannot maintain a strong reducing ability, this allows the PrestoBlue™ assay to detect the quantity of viable cells in a population based on the fluorescent intensity of the solution. This assay can be used to quantify cell viability upon exposure to a potential cytotoxin or to quantify cell proliferation over time as the dyes are not cytotoxic for short exposures.

The potential cytotoxicity of LAP (photo-initiator) and tartrazine (photo-absorber) were quantified with a PrestoBlue™ assay to confirm their suitability as additives to the bioink for DLP bioprinting. Fibroblasts were seeded into a 96 well plate with 10,000 cells per well in 100 µl of complete media. After 12 hours, all media was removed and replaced with various concentrations of LAP, tartrazine, or both, dissolved in complete media. During the 90-minute incubation at 37ºC, Prestoblue working solution was prepared by diluting the PrestoBlue stock solution in complete media at 10% (v/v). At the end of the incubation time all solutions were removed from the wells and 100 µl of PrestoBlue working solution was added to each well. The plate was protected from light for 12 minutes and then each well was read on a microplate reader (560/590 nm ex/em). The reading of the blank (Prestoblue working solution in an empty well) was subtracted from each value before data analysis.

2.1.5 DLP Bioprinting Cell-laden or Acellular Constructs

DLP bioprinting GelMA requires a photo-initiator to initiate the crosslinking reaction and a photo-absorber to prevent excessive scattering of the projected light. LAP has proven a suitable photo-initiator for photo-crosslinking GelMA with 405 nm light [91], [97]. LAP is unstable in solution and was always stored at 4°C and used within 1 week. Tartrazine is a Food and Drug Administration (FDA) approved yellow food dye (E102) that functions wells as a photo-absorber with DLP bioprinting [88]. A 250 mM tartrazine stock solution was prepared in DPBS + 100 U/mL pen/strep, stored at 4°C, and heated before use to redissolve any precipitates.

To prepare hydrogels for DLP bioprinting, tartrazine stock solution and LAP were added to DMEM with antibiotic as required for the desired GelMA concentration (Table 2-2). The solution was protected from light and warmed in a water-bath at 40°C for 30 minutes or until the LAP had dissolved. GelMA was weighed and added to the solution which was then vortexed and left in the water bath for another 30 minutes for the GelMA to dissolve and the bubbles to settle. Before use, the bioink was sterile filtered with a 0.22 µm acetate cellulose syringe filter.

Table 2-2: Bioink compositions for DLP bioprinting GelMA hydrogels

[GelMA] (w/v)	[Tartrazine]	[LAP] (w/v)	Crosslinking time per layer (s)	Light Intensity (mW/cm^2)	1st layer burn in	Solvent	Layer Height
5%	1.5 mM	0.3%	27.5	20	4X	DMEM + 100 U/mL pen/strep	50 µm
7.5%	1.5 mM		27.5				
10%	2.5 mM		25				

A Lumen-X DLP bioprinter (Cellink, Sweden) was sterilized and moved into a biological safety cabinet to provide a sterile environment. CAD models of the desired constructs were uploaded with a USB drive and sliced at a 50 µm layer height. The crosslinking time, light intensity, 1st layer burn-in, and layer height were all chosen as specified depending on the bioink (Table 2-2).

If preparing cell-laden constructs, the cells were prepared at this stage. Briefly, fibroblasts were dissociated and transferred to a falcon tube, centrifuged, resuspended, and counted with a hemacytometer (Sigma-Aldrich, cat#: Z359629). A volume containing 550,000 cells was added to another falcon tube which was again centrifuged and the supernatant was removed. 1.1 mL of warm sterile bioink was added to the cell pellet and gently mixed by pipetting to homogenously distribute the cells in the hydrogel. A slightly cut pipette tip was used to prevent cell lysis during this step. The required volume of cell-laden hydrogel, usually 1.0 mL for small prints, was added to the PDMS-coated petri dish and the print was started. A pre-printing control of 15ul cell-laden hydrogel was taken from the residue in the falcon tube and added to 300 µl of complete media in a 24 well plate.

During printing, a 24 well plate was filled with media and warmed at 37°C. After printing, each construct was gently scrapped off of the build platform with a plastic razor and placed in a well of pre-warmed media. A post-printing control of 15 µL of the remaining cell-laden hydrogel from the petri dish was added to 300 µl of media. The bioprinted constructs were incubated at 37°C for 1-2 hours to allow the tartrazine and unreacted LAP to diffuse out. At that time, the media was replaced with fresh complete media and the plate was returned to the incubator for culture. Media was changed completely on days 1, 3, and 5.

2.1.6 Printability Characterization

To characterize their printability, GelMA bioinks with 5, 7.5, and 10% (w/v) GelMA were prepared (Table 2-2) and DLP bioprinted into a 1 mm thick rectangle containing circular pores vertically through the construct with diameters varying from 0.25 to 2 mm. Low magnification panoramas of the constructs were taken with phase contrast on an inverted microscope.

2.1.7 Scanning Electron Microscopy

A Hitachi S-4800 scanning electron microscope (SEM) was used to image the flat upper surface and cross-section of the DLP bioprinted 7.5% GelMA constructs. The constructs were lyophilized to remove all moisture, mounted on SEM stubs, and sputter coated with gold in preparation for imaging. Images were taken with a beam energy of 1 keV at a working distance of 8mm and magnifications of 180X or 450X.

2.1.8 DAPI and H&E Staining

The tissue processing, deparaffinization, and staining processes will be described at length in section 3.1.5. Briefly, both human skin tissues and the bioprinted dermal layer were fixed with 10% neutral buffered formalin and subsequently dehydrated with increasing concentrations of ethanol, incubated in xylene, and then placed in melted paraffin wax. Details about donors of the human skin tissue were blinded by the provider (Biopredic, France), making ethical approval unnecessary as per Article 2.4 of the 2018 Tri-Council Policy Statement—Ethical Conduct for Research Involving Humans [98]. The tissues were then embedded in a wax block, sliced into 5 µm sections with a microtome, and floated onto glass slides. After air-drying, sections were deparaffinized with xylene, ethanol, and water. Slides were either stained with 5 µg/mL DAPI or as per the H&E staining protocol. After staining, slides were incubated in ethanol, xylene, coverslipped with Entellan, and imaged with a fluorescent inverted microscope or upright microscope.

2.1.9 Metabolic Activity Assay

A PrestoBlue™ assay was used to evaluate cell proliferation in fibroblast-laden constructs at 1, 3, and 5 days of culture after bioprinting. At each timepoint, 110 µL of PrestoBlue working solution was added to clean wells of a 96 well plate and the cell-laden constructs were carefully lowered into the solutions. A bioprinted hydrogel with the same GelMA concentration but without cells was added to PrestoBlue working solution as the blank condition for each GelMA concentration. This is necessary as resazurin (MW: 229 g/mol) diffuses into the hydrogel and becomes trapped, giving a lower fluorescent intensity when incubated on an acellular hydrogel than in an empty well. The hydrogels were incubated with PrestoBlue working solution for 1 hour at 37 °C and then 100 µl was aspirated from each well and added to a separate 96 well plate. The fluorescent intensity was immediately read on a microplate reader (560/590 nm ex/em). The average blank value (acellular hydrogel) was subtracted from each reading before data analysis. Three replicates of each GelMA concentration and the acellular hydrogel were used.

2.1.10 Live and Dead Staining

A live/dead viability kit for mammalian cells was used to determine the cellular viability of fibroblasts in DLP bioprinted constructs. Calcein AM easily permeates cells and is enzymatically converted by living cells to the highly fluorescent calcein which is then relatively impermeable to the cell membrane. Ethidium homodimer-1 only enters cells with ruptured membranes and subsequently binds to nucleic acids which tremendously increases its fluorescence.

Live/dead working solution was prepared by diluting the live and dead dyes at 0.25 µl/mL and 1.0 µl/mL respectively in DPBS. At 1 and 5 days of culture after bioprinting, fibroblast-laden constructs were incubated in live/dead working solution for 30 minutes at room temperature protected from light. The constructs were then washed twice with DPBS and imaged immediately with a fluorescent inverted microscope (live: 488/525 nm ex/em, dead: 546/607 nm ex/em).

2.1.11 Cytoskeleton Staining

To visualize the morphology and distribution of fibroblasts in the bioprinted constructs, filamentous actin (f-actin) and cell nuclei were stained. At 5 days of culture after bioprinting, fibroblast-laden constructs were fixed for 45 minutes with 10% neutral buffered formalin at room temperature then washed 3 times with DPBS. The constructs were permeabilized with 0.3% Triton-X100 in PBS for 15 minutes. A stock solution of Alexa Fluor™ 488 Phalloidin was prepared in methanol as per the manufacturer's instructions and diluted 1:40 in PBS containing 0.3% Triton-X100 and 1% BSA. Constructs were incubated in the diluted phalloidin solution for 1 hour at room temperature protected from light, then incubated in a 5 µg/mL DAPI solution for 15 minutes. Finally, the constructs were washed 3 times in DPBS and stored at 4 °C until imaging. A confocal laser scanning microscope was used to capture a z-stack of a segment of the construct.

2.1.12 Data and Statistical Analysis

All statistical analysis in this chapter was performed using GraphPad Prism 8 and results are shown as the mean plus or minus one standard deviation. The bioink cytotoxicity and cell proliferation experiments were performed with three replicates for each condition. For the cytotoxicity analysis, ordinary one-way analysis of variance (ANOVA) with a post-hoc Dunnett's multiple comparison's test ($\alpha = 0.05$) was used to compare the viability of each condition with the control. For the cell proliferation analysis, the fluorescent intensity at each timepoint was normalized to the average of that concentration's initial intensity on day 1. This allows the results on days 3 and 5 for each concentration to be presented as a fold-change compared to day 1. Comparisons of the normalized cell proliferation in each GelMA concentration after 5 days was performed with two-way ANOVA using a post-hoc Tukey's multiple comparisons test ($\alpha = 0.05$).

2.2 Results and discussion

2.2.1 Bioink Cytotoxicity

Before cell-laden bioprinting was conducted, the cytotoxicity of LAP and tartrazine was evaluated with a PrestoBlue assay. A 90-minute exposure time was chosen as a generous estimation of how long the fibroblasts will be in contact with LAP and tartrazine during the printing process before the bioprinted constructs are placed in media which allows both molecules to diffuse out of the constructs. The cytotoxicity test was performed with three concentrations of LAP (0.6%, 0.3%, 0.1% (w/v)) and tartrazine (5, 2.5, 1.25 mM) each tested separately (Fig. 2-1). Of these, the only significant decrease in viability compared to the control was seen in the 0.6% LAP condition (85.5 ± 5.5%, $p = 0.036$). The bioink to be used for DLP bioprinting contains a maximum of 0.3% LAP and 2.5 mM tartrazine. When exposed to this solution, referred to as 'bioink' (Fig. 2-1), fibroblasts showed an insignificant decrease in viability (89.6 ± 2.9%, p = 0.195).

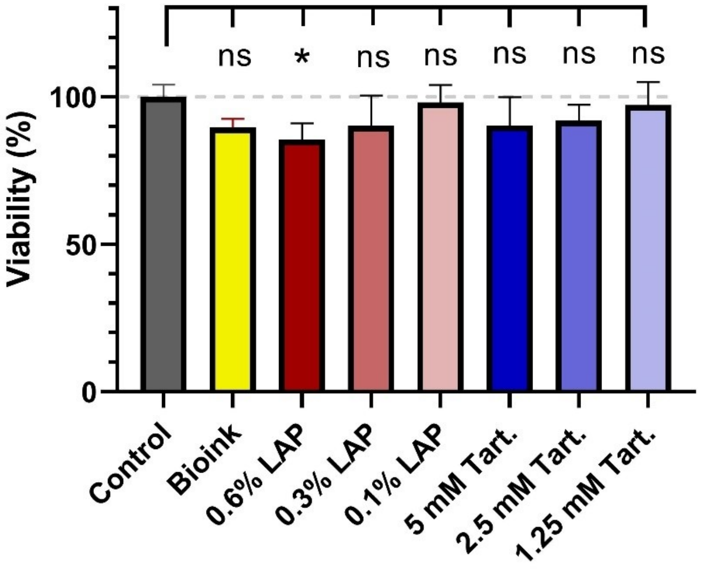

*Figure 2-1: Cytotoxicity of 90 minutes of LAP and/or Tartrazine Exposure to Fibroblasts in 2D Culture. 'Bioink' = 0.3% LAP and 2.5mM tartrazine. * $p < 0.05$.*

2.2.2 Printability Characterization

The DoF of the GelMA used for all DLP bioprinting was 85.1% ± 1.2%. A printability characterization was performed with 5%, 7.5%, and 10% (w/v) GelMA to evaluate the suitability of using DLP bioprinting to form small features. First, the printability of circular pores was characterized by bioprinting a 3D model containing pores with diameters of 2 mm, 1 mm, 500µm, and 250 µm (Fig. 2-2, Table 2-3). 10% GelMA showed excellent printability; all pore sizes formed and there was minimal deformation near the edges of the construct. The 7.5% GelMA condition also showed good printability with all pore sizes forming and only slight deformations near the edge of the construct. On the contrary, with 5% GelMA the 250 µm pores did not form, the 500 µm pores partially formed, and there was significant deformation on all edges of the construct.

Significant swelling was also observed for the 5% GelMA condition which was not apparent with 7.5 or 10% GelMA.

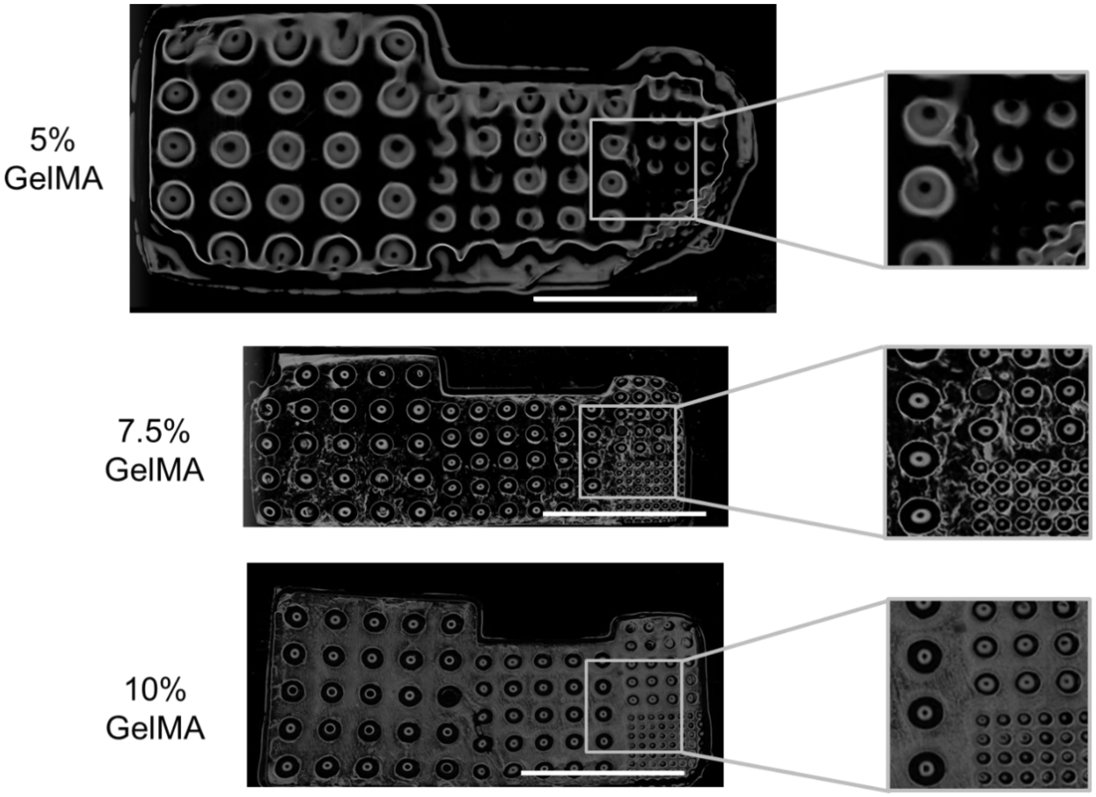

Figure 2-2: Printability of 5%, 7.5%, and 10% (w/v) GelMA demonstrated by DLP bioprinting a model containing circular pores with nominal diameters of 2 mm (left), 1 mm (middle), 500 µm (top right), and 250 µm (bottom right). Scale bar: 1 cm.

Table 2-3: Printability map of circular pores in 5, 7.5, and 10% GelMA.

	Pore Diameter			
	2 mm	1 mm	500 µm	250 µm
5% GelMA	🟩	🟩	🟥	🟥
7.5% GelMA	🟩	🟩	🟩	🟩
10% GelMA	🟩	🟩	🟩	🟩

Printable 🟩
Not printable 🟥

Prints using concentrations of GelMA below 5% failed to produce constructs with recognisable features. Although high concentrations of GelMA such as 15 and 20% were easily printable with high resolution (data not shown), these were considered unsuitable for creating tissue-engineered skin due to their unfavorable cell microenvironment (Fig. 1-10) [82].

2.2.3 Cell Viability in DLP Bioprinted Dermal Constructs

With the biocompatibility and printability of the bioink confirmed, GelMA containing 0.5×10^6 fibroblasts/mL was then DLP bioprinted to create a tissue-engineered dermis. The CAD model was designed as a Ø 6.25 mm disk with a thickness of 1 mm (Fig. 2-3) in order to snugly fit in Transwell® Inserts (I.D. 6.5mm). Closely spaced circular pores with 500 µm diameters were included to provide adequate nutrients and oxygen to fibroblasts encapsulated in the hydrogel. The pores only penetrate 750 µm into the disk to preserve a flat surface on one face of the disk for the epidermal layer which will be described in detail in Chapter 3. Hereafter, the flat surface will be referred to as the **apical surface** and the face penetrated with pores will be referred to as the **basal surface**. Arrays of 15 constructs were DLP bioprinted simultaneously (Fig. 2-3). Arrays printed with 10% GelMA usually had all 15 constructs form without any defects. The printability was slightly less consistent when using 7.5% GelMA, with 14/15 constructs typically printing to an acceptable degree. This is evidenced by Fig. 2-3 which shows an array of 7.5% GelMA constructs that all printed well except for the front right construct. When using 5% GelMA approximately half of the constructs printed deformed.

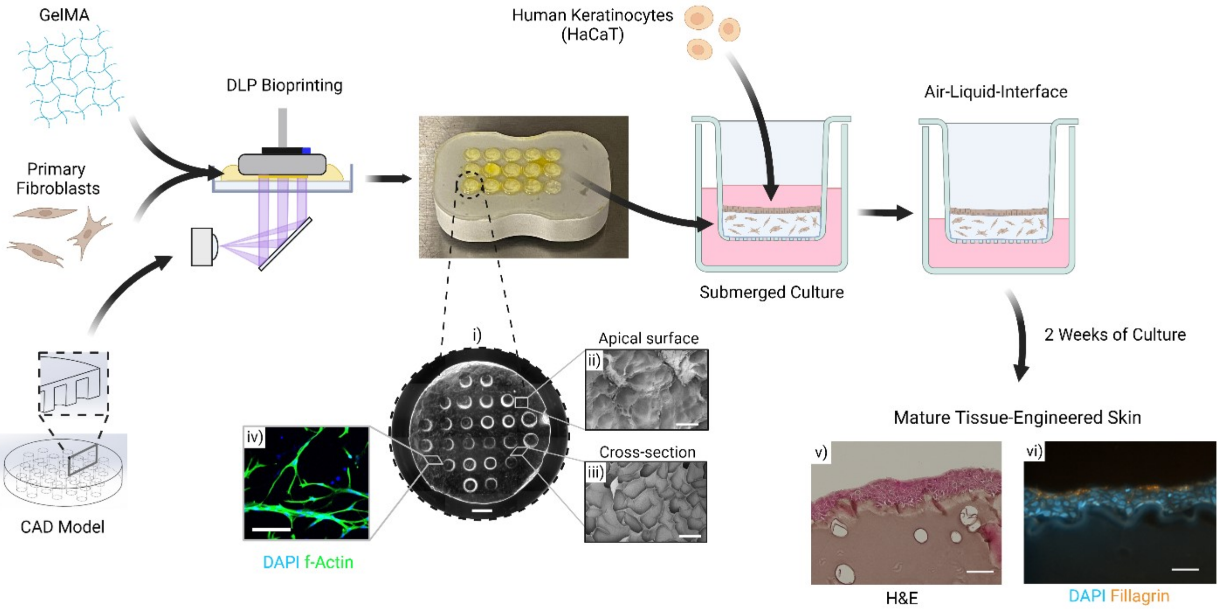

Figure 2-3: Schematic of the tissue-engineered skin biofabrication process. GelMA hydrogel and primary fibroblasts are combined and DLP bioprinted into porous constructs (i) with a flat apical surface (ii), and microporous interior (iii) that is laden with fibroblasts (iv). HaCaT cells are added and after culture at the ALI a stratified and matured epidermis forms (v, vi). Scale bars: 1 mm (i), 100 µm (ii, iv), 50 µm (iii, v, vi).

Using this CAD model, GelMA concentrations of 5, 7.5, and 10% (w/v) showed high fibroblast viability 1 day after bioprinting (Fig. 2-4). The pores appear to be allowing adequate nutrients and oxygen to reach cells throughout the construct as even the cells farthest from the pores were viable after 5 days of culture. As expected, fibroblasts encapsulated in the GelMA hydrogel initially had a round morphology and eventually spread to varying degrees depending on the hydrogel concentration and time in culture. After 5 days, most fibroblasts in 5% and 7.5% GelMA developed a significantly elongated morphology with long projections while in 10% GelMA most fibroblasts were rounded with small projections. This reaffirms the concept that low GelMA concentrations are more appropriate for encouraging fibroblasts to adopt a similar morphology as they do *in vivo* [36], [82].

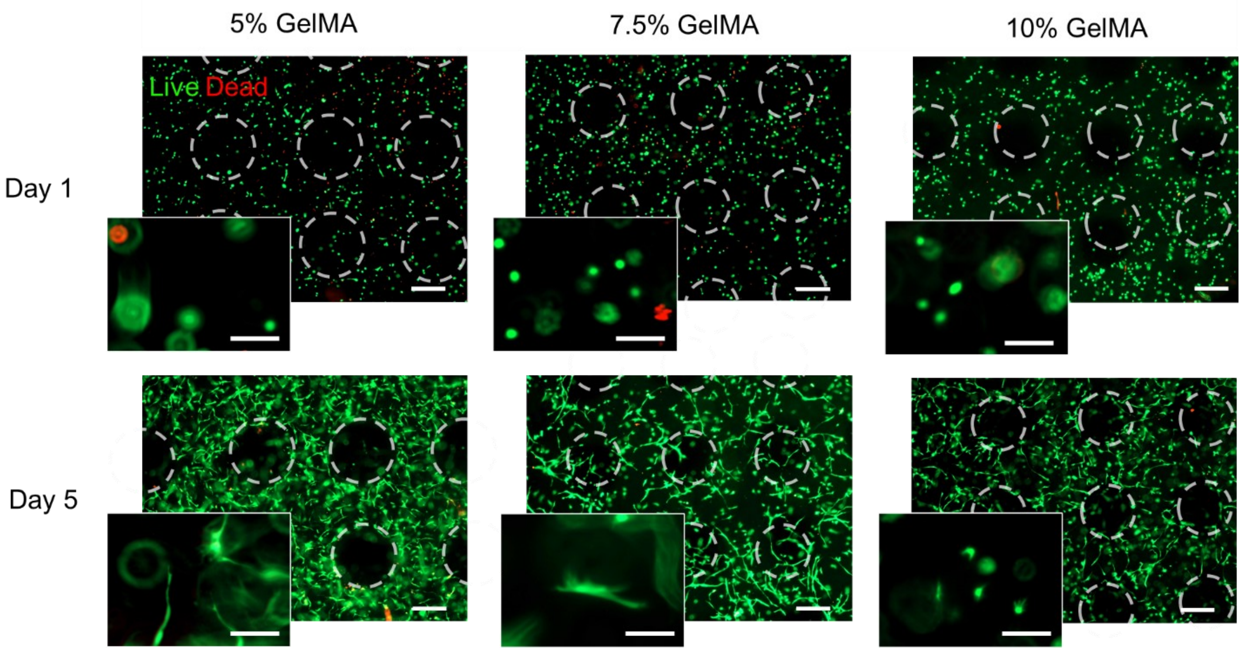

Figure 2-4: Fibroblasts DLP bioprinted in 5, 7.5, and 10% (w/v) GelMA on days 1 and 5 shown with a live (green) and dead (red) stain. Scale bars: 500 µm; and 100 µm in the high magnification insets.

2.2.4 Cell Distribution in DLP Bioprinted Dermal Constructs

To evaluate the 3D distribution of fibroblasts through the constructs, confocal microscopy was used to take z-stack images of fibroblasts in 7.5% GelMA (Fig. 2-5). Filamentous-actin in the fibroblast cytoskeleton was fluorescently stained green imposed over a blue nuclear counterstain. The side view of this stack shows that fibroblasts were distributed evenly through the bulk of the hydrogel. Interestingly, a large population of fibroblasts with a bipolar morphology proliferated on the basal surface, regardless of whether that surface was facing upwards or downwards during culture. Even after 5 days of culture the flat apical surface remained relatively free of fibroblasts, presumably due to the relatively rough surface left by the build platform of the DLP bioprinter.

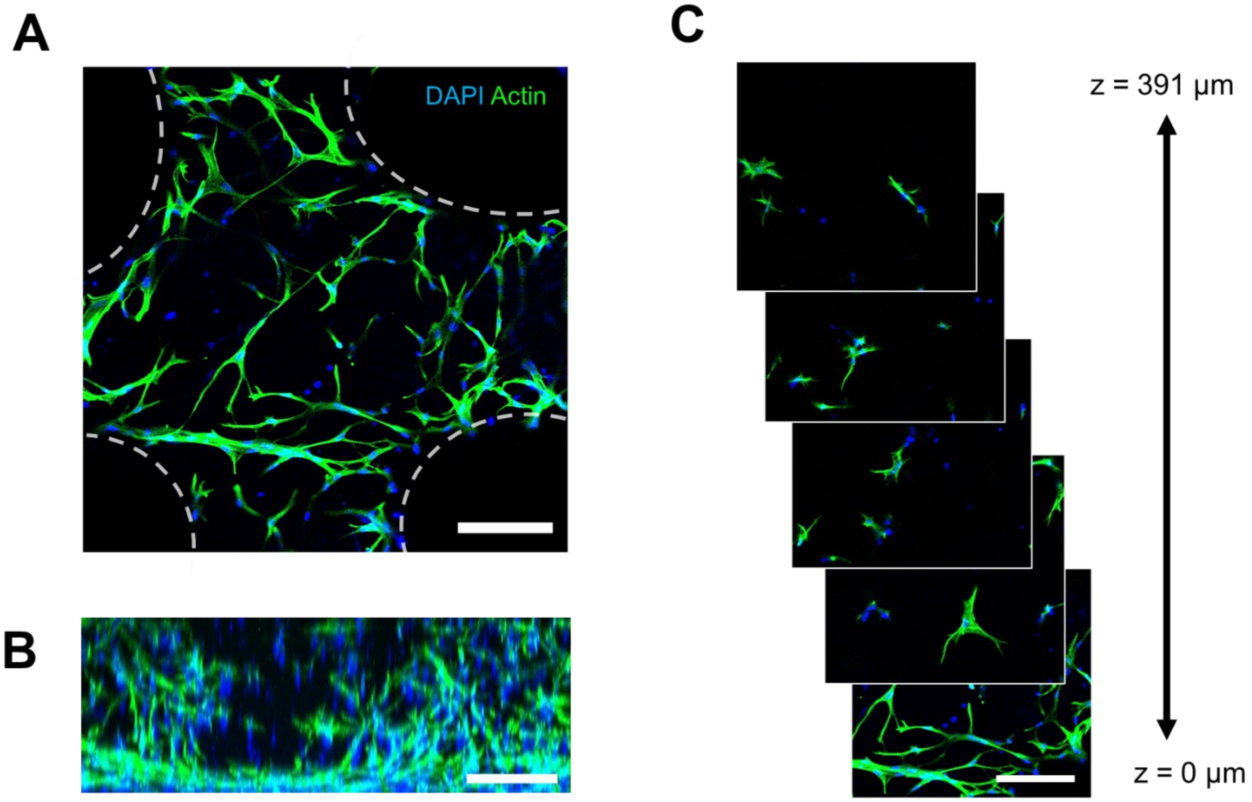

Figure 2-5: Distribution of fibroblasts throughout a DLP bioprinted 7.5% GelMA construct after 5 days of culture. (A) Fibroblasts on the basal surface. (B) Maximum projection from a side-view of the construct. (C) Stack of images showing fibroblasts encapsulated in the interior of the hydrogel. Scale bars: 200 µm.

The proliferation of fibroblasts within the bioprinted constructs was quantified with a PrestoBlue assay, showing an over three-fold increase in the number of cells on day 5 compared to day 1 for all GelMA concentrations (Fig. 2-6). On day 5, normalized cell proliferation was significantly higher in 5% GelMA than 10% GelMA (6.2- and 3.8-fold respectively, $p = 0.0003$). Also on day 5, normalized proliferation in 7.5% GelMA (4.4-fold) was significantly lower than in 5% GelMA (6.2-fold, $p = 0.0152$) and only slightly higher than in 10% GelMA (3.8-fold, $p = 0.553$). Therefore, not only does a low concentration of GelMA allow fibroblasts to develop a spread morphology, it also encourages more cell proliferation. These findings are in agreement with numerous studies that have touted the benefits of forming engineered-tissues from 5% GelMA

[75], [78]. A limitation this analysis is that all viable cells growing either on the exterior of or encapsulated within the constructs will contribute to the fluorescent intensity at each timepoint. Especially on the 10% GelMA constructs, a significant population of fibroblasts were noticed proliferating on the basal surface which could have skewed the results to overestimate the proliferation of encapsulated cells.

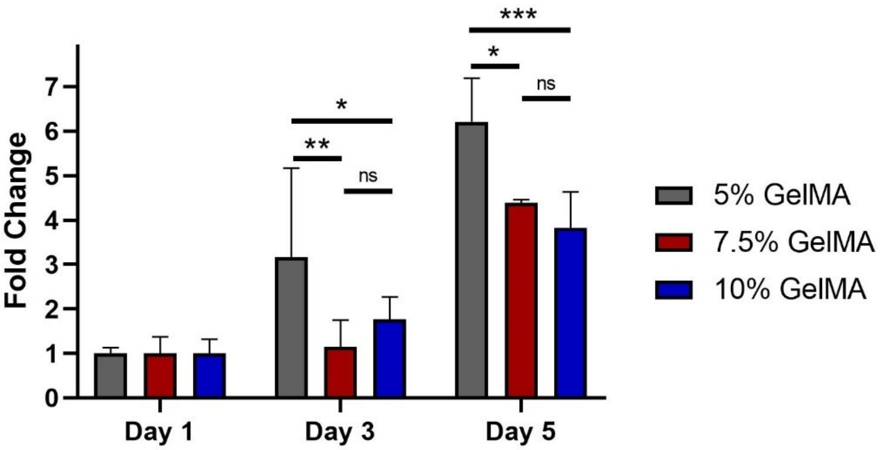

*Figure 2-6: Fibroblast proliferation in DLP bioprinted GelMA constructs over 5 days of culture (*p<0.05, **p<0.01, ***p<0.001).*

The fibroblast viability and proliferation results confirm the results of the cytotoxicity assay and the widely accepted consensus that GelMA is a suitable biomaterial for producing engineered tissues [73], [97], [99]. Constructs of 5, 7.5, and 10% GelMA all provided high cell viability and even cell distribution throughout the hydrogel; however, they varied significantly in terms of fibroblast morphology, proliferation, and printability. While fibroblasts adopted a spread morphology and proliferated significantly more in 5% GelMA, it was challenging to produce small features or arrays of constructs from that concentration. Conversely, 10% GelMA offered excellent printability but a more rounded fibroblast morphology and significantly less proliferation over time. The intermediate concentration, 7.5% GelMA, encouraged a spread fibroblast morphology and offered a middle ground in terms of printability and cell proliferation.

The final design parameter of the dermal layer that was verified was the fibroblast density within the hydrogel. The fibroblast density in thin slices of the tissue-engineered dermis was compared to the cell density in similar slices of human reticular dermis using a nuclear stain (Fig. 2-7). Although qualitative, these representative images show that 0.5 x 10^6 fibroblasts/mL is a reasonable approximation of the fibroblast density in the reticular dermis and for example is neither an order of magnitude higher nor lower than the actual fibroblast density.

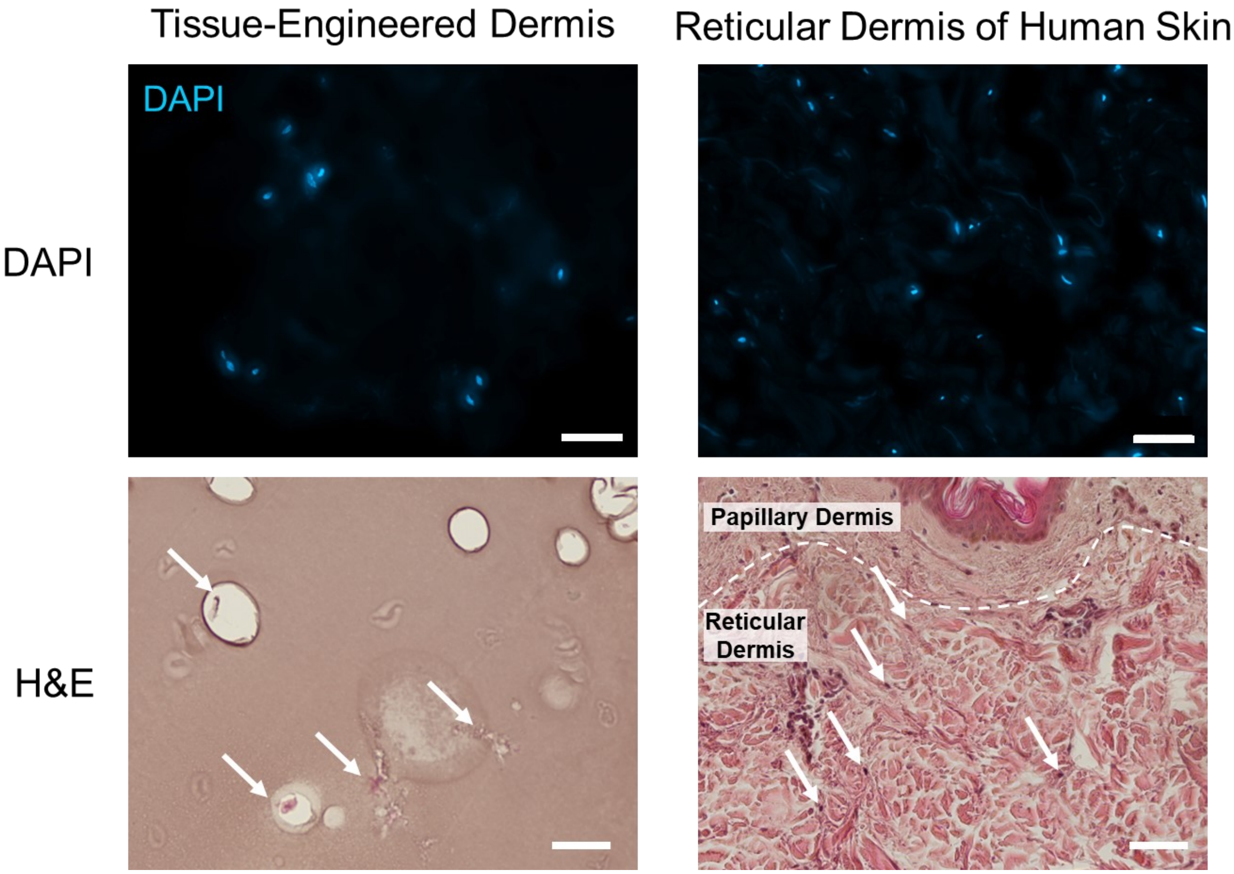

Figure 2-7: Representative images of cell densities in the tissue-engineered dermis after 5 days of culture and human reticular dermis shown. White arrows indicate fibroblasts. Scale bars: 50 µm.

2.3 Conclusion

These experiments demonstrated that DLP bioprinting GelMA laden with 0.5 x 10^6 fibroblasts per mL produces constructs with high cell viability, an even cell distribution, and a similar cell density as in human reticular dermis. All GelMA concentrations tested showed sufficient fibroblast viability and proliferation over 5 days in culture, however; they differed significantly in terms of printability and also promoted different morphologies of the encapsulated fibroblasts. 10% and 7.5% GelMA showed good printability and could successfully form 250 µm diameter pores, while bioprinting with 5% GelMA was inconsistent and could only successfully form pores with a minimum diameter of 1 mm. Fibroblasts encapsulated in 5% and 7.5% GelMA both developed a well-spread morphology, indicating that these concentrations provide a desirable cellular microenvironment. As it was not practical to proceed with 5% GelMA due to severe challenges with printability, 7.5% GelMA was considered the optimal GelMA concentration for DLP bioprinting a tissue-engineered human dermis. While it may be tempting to increase the photo-initiator concentration to improve the printability of low GelMA concentrations, the cytotoxicity assay (Fig. 2-1) shows that increasing the photo-initiator concentration will lead to a decrease in cell viability. Ultimately, the GelMA concentration used to produce the full-thickness tissue-engineered skin will also depend on if it is a suitable substrate for the epidermal layer. A biofabrication approach for the epidermal layer should be selected with the target of being compatible with a 7.5% GelMA substrate, although, the GelMA concentration could be adjusted, if necessary, with knowledge and consideration of the detriments of higher or lower GelMA concentrations.

Chapter 3 - Establishment and Verification of the Epidermal Layer

A tissue-engineered model of skin for studying wound healing must also include the epidermis as reepithelialisation and cellular cross-talk between keratinocytes and fibroblasts are both crucial in the wound healing process [2], [31]. First, the keratinocyte cell type and biofabrication approach will deliberated and then a suitable choice for each will be selected. The experimental work of this chapter will outline the process of forming, maturing, and then verifying the epidermal layer of the tissue-engineered skin. This epidermis will be formed on the flat apical surface of the DLP bioprinted dermal constructs.

Unlike the dermis, the human epidermis is mostly comprised of cells and has relatively little ECM (Fig. 1-1). In 2D culture human keratinocytes proliferate rapidly until a confluent monolayer has formed. If the apical surface of the confluent keratinocyte layer is exposed to air, the monolayer will stratify and differentiate into a mature epidermis. Accordingly, most approaches for creating an epidermis *in vitro* take advantage of this property by only forming a monolayer of keratinocytes and allowing a stratified epidermis to form through culture at the ALI. Inkjet bioprinting [37] and pipetting cell suspensions [43], [62], [94] are the most common approaches for creating an epidermis *in vitro*. While inkjet bioprinting offers more uniform cell deposition and is highly scalable, it is not worth the complexity in most cases as even if there are gaps in the initial cell layer the keratinocytes will quickly proliferate to form a confluent layer.

Primary human keratinocytes are readily available and once exposed to high Ca^{2+} concentrations or at confluence they begin to terminally differentiate and form a stratified epidermis. However, these cells can only be expanded *in vitro* for a short time, have fluctuating proliferation and differentiation characteristics at different passages, and have heterogenous phenotypes depending on the donor. These factors severely complicate the use of primary keratinocytes in tissue-engineered skin. Immortal human keratinocytes cell lines such as hTert keratinocytes or HaCaT cells (Human Adult low Calcium At high Temperature) solve many of these problems as they can proliferate indefinitely, retain their ability to differentiate normally, and have a homogenous phenotype [100], [101]. HaCaT cells in particular have frequently been used in tissue-engineered skin due to their attractive *in* vitro growth and differentiation characteristics [50], [62]. While HaCaT cells promptly form a stratified epidermis when implanted in athymic mice, it is less straightforward to produce a mature epidermis from HaCaT cells *in vitro*. Schoop *et al.* and Maas-Szabowski *et al.* performed intensive characterizations of HaCaT stratification *in vitro* and reported the optimal conditions for differentiation: media supplemented with 2 ng/mL TGF-α and 100 ng/mL GM-CSF, and an adjacent fibroblast feeder layer with 0.5 x 10^6 cells/mL.

For keratinocyte differentiation to occur, the apical surface of a monolayer must be raised to the ALI. In practice this is usually implemented with a Transwell™ insert, a well plate insert with a permeable membrane that can suspend cells or a tissue above the bottom of the well. Removing the media from the Transwell compartment exposes the tissue to air while it still receives hydration and nutrients through the membrane from the remaining media in the well.

3.1 Materials and Methods

Trypsin-EDTA (Gibco, cat#: 15400), DiI (Invitrogen, cat# D3911), N,N-Dimethylformamide (DMF, Caledon, cat# 3800-1), and transwell inserts (Sigma-Aldrich, cat#: CLS3470-48EA) were used for cell culture and analysis.

Tween 20 (Sigma-Aldrich, cat#: P1379), tris base (Fisher Scientific, cat#: BP152-1), EDTA (Fisher Scientific, cat#: S311), sodium citrate (Bio Basic Canada Inc., cat#: CB0035), xylene

(Sigma-Aldrich, 534056), paraffin wax (Fisher Scientific, cat#: 22900700), SuperFrost Plus slides (Fisher Scientific, cat# 12-550-15), entellan (Merck, cat# 1.07961.0500), acid alcohol 1% (Newcomer Supply, cat#: 10011A), Harris' Hematoxylin (Newcomer Supply, Cat#: 1201A), and eosin Y (Newcomer Supply, cat#: 1072A) were used for tissue processing and histology.

3.1.1 HaCaT Cell Culture and Labelling with DiI

HaCaT cells (Addex Bio; Cat#: T0020001) were cultured in DMEM with 10% (v/v) FBS and 100 U/mL pen/strep with media changes every second day. At 80-90% confluency cells were passaged with 0.25% Trypsin-EDTA and split at 1:5 or 1:10. Media was changed every second day.

The fluorescent cell tracker DiI was used to better visualize HaCaT cell attachment to GelMA substrates (Fig. 3-1). This lipophilic dye integrates with the plasma membrane and is retained for days in culture. A 1 mg/mL stock solution of DiI in DMF was diluted to 10 µg/mL in 3 mL of DMEM. The DiI media was added to a T-25 flask of semi-confluent HaCaT cells and incubated at 37°C for 20 minutes. The HaCaT cells were then washed 3 times with DPBS, trypsinized, and used as required.

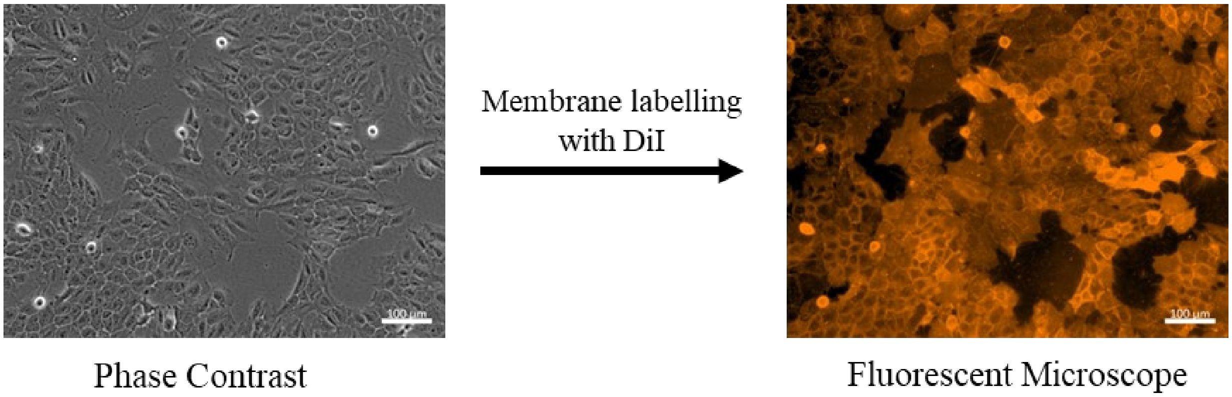

Phase Contrast

Fluorescent Microscope

Figure 3-1:HaCaT plasma membrane labelling with DiI. Scale bars: 100 µm.

3.1.2 Characterization of HaCaT Coverage on GelMA Substrates

Hydrogel disks of Ø 6.5 mm and 1 mm height were DLP bioprinted from 5, 7.5, and 10% GelMA. CAD models without pores were used to improve the quality of the images. The hydrogel disks were carefully placed in Transwell Inserts, ensuring that the rougher surface that was in contact with the build-platform during printing faced upward in culture. The well and Transwell compartment were filled with complete media and incubated for 2 hours at 37°C. Then media was aspirated from the Transwell compartment and replaced with 100 µl of media containing 165,000 DiI labelled HaCaT cells (0.5 x 10^6/cm^2) for each construct. After 24 hours the media was gently changed to remove unattached cells and HaCaT cells that had adhered to the GelMA surface were imaged with a fluorescent microscope. Media was again removed from the Transwell compartment and the apical GelMA surface was seeded for a second time with 165,000 DiI labelled HaCaT cells in 100 µl of media. 24 hours after the second seeding the constructs were washed and imaged again as before. This characterization of HaCaT attachment was performed in triplicate for each GelMA concentration.

Images were imported to ImageJ to quantify the percentage of cell coverage on each GelMA concentration. A colour threshold was set that was appropriate for separating the areas covered with cells from the background fluorescence. This quantification was performed on one low magnification and one high magnification image of each replicate.

3.1.3 Developing a Tissue-Engineered Epidermis

An array of dermal constructs with Ø500 µm partial pores was DLP bioprinted from 7.5% GelMA laden with 0.5 x 10^6 fibroblasts/mL. These constructs were cultured submerged in a 24 well plate for 5 days to allow for fibroblasts to attach, spread, and proliferate in the hydrogel and to begin secreting growth factors. On the 5th day, the dermal constructs were carefully transferred into modified Transwell inserts with their apical surfaces facing upwards. This orientation provides a flat upper surface for the epidermal layer to form on and also allows nutrients to diffuse through the Transwell membrane and into the pores of the construct. The easiest method to accomplish this in practice was to fill the Transwell compartment with media and allow the hydrogel to slowly sink to the bottom. An inverted microscope was used to confirm the orientation of the constructs which were floated into the media and flipped if necessary. 7.5% GelMA constructs without fibroblasts were also loaded into Transwell with the apical surface facing upwards to evaluate how the presence or absence of fibroblasts influences epidermal maturation.

HaCaT cells were then seeded on the apical surface of each construct in the inserts at a density of $0.5 \times 10^6/cm^2$. After 24 hours the constructs were gently washed once with media and another seeding of $0.5 \times 10^6/cm^2$ HaCaT cells was added to each Transwell compartment. The confluent HaCaT monolayer was then cultured submerged in proliferation media (DMEM + 10% FBS) for 2 days to begin the differentiation process. On the 2nd day, the constructs were lifted to ALI by removing the media from the Transwell compartment and replacing the media in the bottom of the well with the epidermal differentiation media (DMEM + 10% FBS + 2 ng/mL TGF-α + 100 ng/mL GM-CSF, Fig. 3-2). Media was changed every 2nd day for the first week and daily for the second week. Culture media was taken at days 4 and 14 of ALI culture and stored at -80 °C for cytokine analysis.

3.1.4 Tissue Processing for Histology

At 7 and 14 days of culture at the ALI, inserts holding tissue-engineered skin were transferred to a separate plate and fixed in 10% neutral-buffered formalin for 45 minutes at room temperature. All steps were conducted in a fume hood as neutral-buffered formalin, xylene, and Entellan all produce toxic fumes. Fixed tissues were washed with DPBS, dehydrated in ethanol, cleared in Xylene, then incubated in liquid paraffin wax following published protocols for histological analysis of cell-laden hydrogels [37], [46]. A microtome was used to slice 5 μm sections which were floated onto glass slides and deparaffinized prior to staining.

3.1.4 H&E Staining

Hematoxylin and Eosin (H&E) staining is the most popular histology stain for clinical evaluation of tissue morphology and is also widely used in tissue-engineering research [40], [93], [95], [102]. The major benefit of H&E staining is that it clearly shows the gross morphology of the tissue as well as the morphology of individual cells. The hematoxylin solution binds to acidic intracellular components such as the nucleus and stains them a dark purple pigment [103]. Eosin binds non-specifically to proteins and creates a gradient of pink colours in the cell cytoplasm, red blood cells, and collagen fibers [103]. H&E staining was performed as per the manufacturer's instruction (Newcomer's Supply).

3.1.5 Immunohistochemistry

While information about the tissue morphology is useful, it is often necessary to visualize patterns of specific protein expression within tissue-engineered skin to confirm the maturation and differentiation of the epidermis. Immunohistochemistry (IHC) uses antibodies that are specific for various proteins and can be conjugated with fluorescent dyes to accurately visualize patterns of protein expression with a fluorescent microscope. IHC was performed on tissue cross-sections mounted on glass slides that were embedded, sliced, deparaffinized and hydrated as described in the previous section. The general steps of IHC staining were heat-induced epitope retrieval, permeabilization, blocking, primary antibody staining, secondary antibody staining, and finally DAPI staining before mounting with a coverslip. Primary antibodies specific for filaggrin, laminin, fibronectin, and Ki-67 were used to characterize the tissue-engineered skin and compare it to human skin (Table 3-1).

Formalin fixatives create crosslinks between proteins that can mask epitopes from detection with IHC. Proving this point, when human skin was stained following this IHC protocol but without antigen retrieval no signal was observed. The solution for this issue is to heat the slides in a buffer to break the protein crosslinks and 'retrieve' the epitopes. This step must take place after deparaffinization but before proceeding with the rest of the IHC protocol. The optimal buffer for epitope retrieval is highly dependant on the epitope in question. Unfortunately, the optimal buffer and pH is rarely mentioned on the antibody datasheet and usually must be determined experimentally.

Primary Antibody	Species	Conjugate	Source
Filaggrin	Rabbit		Novus Bio: NBP1-87528
Laminin	Rabbit		Invitrogen: PA5-115490
Fibronectin	Rabbit		ProteinTech: 15613-1-AP
Ki-67	Rabbit		ProteinTech: 27309-1-AP
Secondary Antibody			
Anti-rabbit IgG	Goat	Alexa Fluor 546	Invitrogen: A-11035

Table 3-1: Antibodies used for IHC on tissue-engineered or human skin.

3.1.6 Trans-Epidermal Electrical Resistance (TEER)

A function generator and digital multimeter were used to determine the electrical resistance of tissues to alternating current [43]. Ø8 mm disks were biopsy punched from the human skin samples and each was press-fit into a Transwell insert (Ø6.5 mm). DLP bioprinted 7.5% GelMA constructs without cells were also loaded into inserts with the apical side facing upwards. All media below the tissue-engineered skin in culture was removed. 500µl of Sterile PBS was added to each well below the inserts loaded with human skin, tissue-engineered skin, or GelMA constructs and 200 µl was added to the upper Transwell compartment. Two solid core wires were sterilized with ethanol and rinsed once in PBS and used as electrodes. A function generator (Instek, GFG-8250A) was used to apply a 50 mV_{p-p} square wave at 1.0 kHz across the sample. The alternating current flowing through the sample was measured with a multimeter (Aneng, AN8008) in series. TEER was performed at each timepoint in triplicate.

3.1.6 Statistical Analysis

All statistical analysis in this chapter was performed in GraphPad Prism 8 and results are displayed as the mean plus or minus the standard deviation. A two-way ANOVA using Tukey's multiple comparisons test was performed to compare the differences in cell coverage between GelMA concentrations at each timepoint (α=0.05). TEER measurements were compared with a one-way ANOVA that also used Tukey's multiple comparisons test ($\alpha = 0.05$).

3.2 Results and Discussion

There are two strategies to form a confluent monolayer of keratinocytes on a hydrogel surface, either a lower density of cells can be seeded which will then proliferate to eventually form a confluent monolayer, or a high density of cells can be seeded which will form a confluent monolayer soon after attachment. Seeding a low density of HaCaT cells on a high concentration of GelMA or gelatin (20% w/v) has proven suitable for creating a monolayer through the cell proliferation approach [43], [50], presumably due to either the stiffness of the substrate or the high density of cell binding sites on the hydrogel surface. However, it is not appropriate to produce the entire dermal construct from such a high concentration hydrogel when fibroblasts are encapsulated. Unfortunately, lower GelMA concentrations are less compatible with this proliferation strategy as Zhao *et al.* demonstrated that 5, 7.5, and 10% GelMA were only ~50, 75, and 85% covered respectively by HaCaT cells 7 days after low density seeding [43]. Conversely, the high density seeding approach has been used for quickly forming confluent monolayers of keratinocytes on 7.5% GelMA [45] or softer hydrogels such as collagen [93], [102]. Benefits of this approach include the shorter culture time required and the compatability with a tissue-engineered dermal layer that consists of 7.5% GelMA.

3.2.1 Characterization of HaCaT Attachment to GelMA

To confirm if the high-density seeding approach will be successful on DLP bioprinted constructs, 0.5 x $10^6/cm^2$ HaCaT cells were seeded on 5, 7.5, and 10% GelMA constructs (Fig. 3-2 A). Even though significantly more HaCaT cells were added than required to form a confluent layer, the cell-covered areas after 24 hours were only **22.8%** ± 14.9%, **74.8%** ± 11.9%, and **77.0%** ± 6.5% for 5, 7.5, and 10% GelMA respectively (Fig. 3-2 B). Instead of focusing on how to optimize the surface for cell adhesion via coatings or other treatments, a second identical seeding of HaCaT cells was performed to fill the gaps after the first seeding. This approach is simple and also has the benefit of forming a two-layered sheet of HaCaT cells which should reduce the length of culture required at the ALI for epidermal maturation [45]. 24 hours after the second HaCaT seeding the cell-covered areas had increased to **26.1%** ± 9.0%, **98.5%** ± 1.2, **98.6%** ±1.2 for 5, 7.5, and 10% GelMA. Both 7.5 and 10% GelMA were sufficiently covered with a confluent HaCaT layer after 2 seedings while 5% GelMA had significantly less coverage.

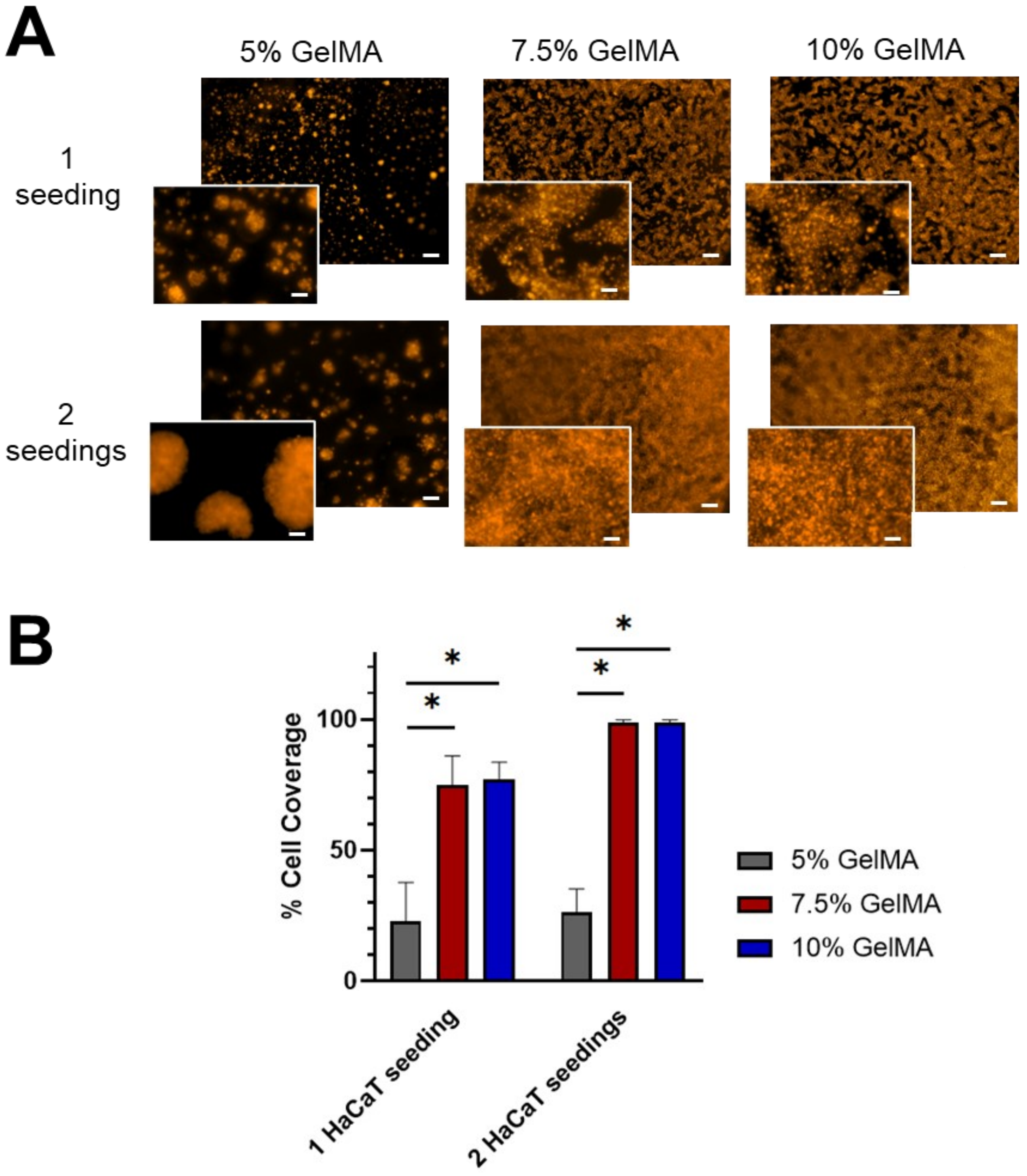

*Figure 3-2: HaCaT attachment to 5, 7.5, and 10% GelMA surfaces after 1 and 2 seedings. (A) DiI labelled HaCaT cells shown at low magnification (scale bar: 500 µm) with higher magnification insets (scale bar: 100 µm). (B) Quantification of HaCaT surface coverage after 1 and two seedings (*p<0.0001).*

Clearly this strategy for forming a confluent HaCaT layer is not suitable for 5% GelMA but can be used effectively with either 7.5 and 10% GelMA. Therefore, 7.5% GelMA will be used for all further experiments as it is the optimal condition for the dermal layer and is sufficient for creating a confluent HaCaT layer with the approach of seeding twice with a high cell density.

3.2.2 Verification of the Maturity of the Tissue-Engineered Skin

After forming of the confluent HaCaT layer, the engineered skin was cultured submerged in proliferation media for 48 hours and then raised to the ALI with the basal surface in contact with differentiation media (Fig. 3-3 A). The originally transparent epidermal surface develops a translucent appearance after approximately 7 days of ALI culture (Fig. 3-3 B). Brightfield images taken on ALI day 7 (Fig. 3-3 C) show (i) the confluent basal keratinocyte layer, (ii) encapsulated fibroblasts with a spread morphology, (iii) fibroblasts on the top surface of the pore, (iv) fibroblasts on the internal surfaces of the pore, (iv) and fibroblasts on the apical surface. The expected spread morphology of the fibroblasts throughout the scaffold after 2 weeks of ALI culture indicates that nutrients are diffusing through the membrane up into the hydrogel and that the differentiation media does not have detrimental effects on the fibroblasts.

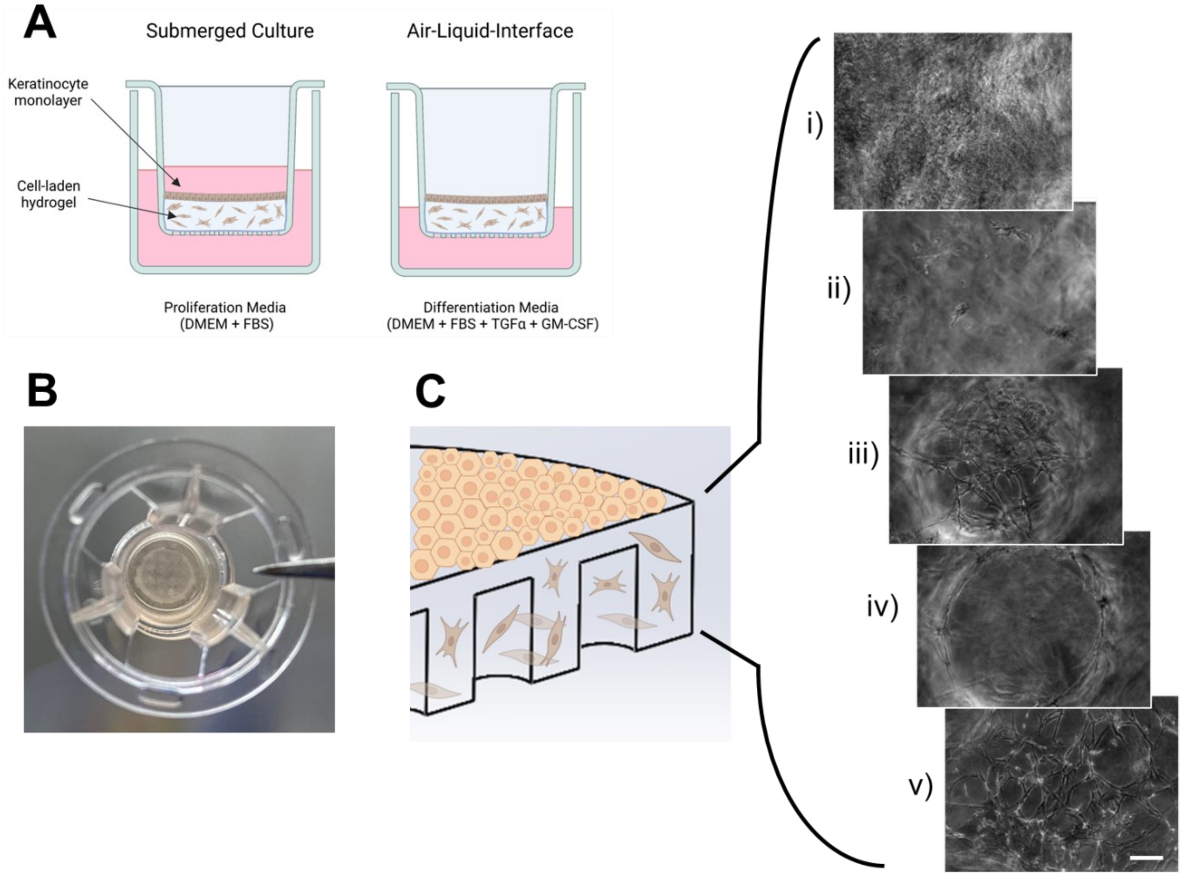

Figure 3-3: (A) The implementation of submerged and ALI culture with Transwell inserts. (B) Top-view of tissue-engineered skin after 2 weeks of maturation. (C) Stack of brightfield images at various heights of the tissue-engineered skin after 2 weeks of maturation. Scale bar: 100 µm.

Cross-sections of the tissue-engineered skin stained with H&E clearly show the epidermis and encapsulated fibroblasts with dark nuclei and light pink cytoplasm (Fig. 3-4 A, B, C). Interestingly, many but not all of the fibroblasts are located in a circular void in the hydrogel, likely due to MMP secretions locally degrading the GelMA matrix. An unexpected ‘ribbing’ pattern can be seen that is not observed on H&E sections of human tissues and appears to be a nuance of performing paraffin-based histology on hydrogels tissues (Fig. 3-4 D). When the paraffins sections are floated after slicing, the hydrophilic hydrogel expands significantly yet the wax surrounding the hydrogel remains the same size. There is usually a slight gap around the hydrogel which provides some space for expansion, but in almost every tissue section some of this ribbing pattern is observed. It seems that this is a product of the histology process and does not correspond to any differences in the intrinsic properties of the hydrogel. This hypothesis is supported by the darker eosin staining of the ribbing pattern which indicates a higher concentration of proteins that would indeed be present in compressed regions of GelMA.

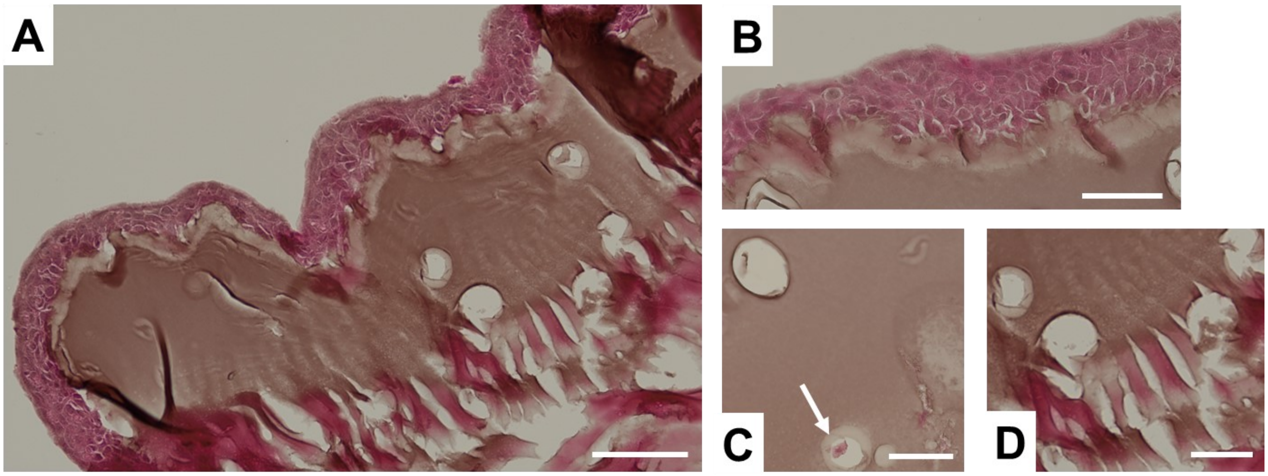

Figure 3-4: H&E staining of tissue-engineered skin cross-sections after 7 days culture at the ALI shows (A) the gross tissue morphology, (B) the epidermal layer, (C) the presence of dermal fibroblasts either in small cavities (white arrow) or spread in the hydrogel, and (D) the contrasting smooth and 'ribbed' appearances of the GelMA hydrogel. Scale bar: 100 µm (A) and 50 µm (B, C, and D).

Tissue-engineered skin was matured at the ALI for up to 2 weeks. To investigate the influence of dermal fibroblasts on epidermal maturation, tissue-engineered skin constructs with fibroblasts (+fibroblasts) and without (-fibroblasts) were matured and stained with H&E after 1 and 2 weeks of ALI culture (Fig. 3-5). As expected, fibroblasts contribute significantly to the integrity and organization of the epidermal layer. Tissue-engineered skin without fibroblasts in the dermal layer after 1 week of maturation was not strong enough to stay intact through the histology process and after 2 weeks the epidermal layer was poorly organized. In the tissue-engineered skin with fibroblasts a significantly more organized epidermis was present after 7 days of maturation and moderately flattened keratinocytes were seen in the superficial layers of the epidermis. After

14 days, drastically flattened keratinocytes were observed in the upper layers of the epidermis (Fig. 3-5, white arrows) but a fully-formed stratum corneum was clearly absent. From the histology analysis alone, it appears that the stratum spinosum and stratum granulosum have formed. More analysis is needed to determine if the flattened keratinocytes have formed a primitive or partial stratum corneum.

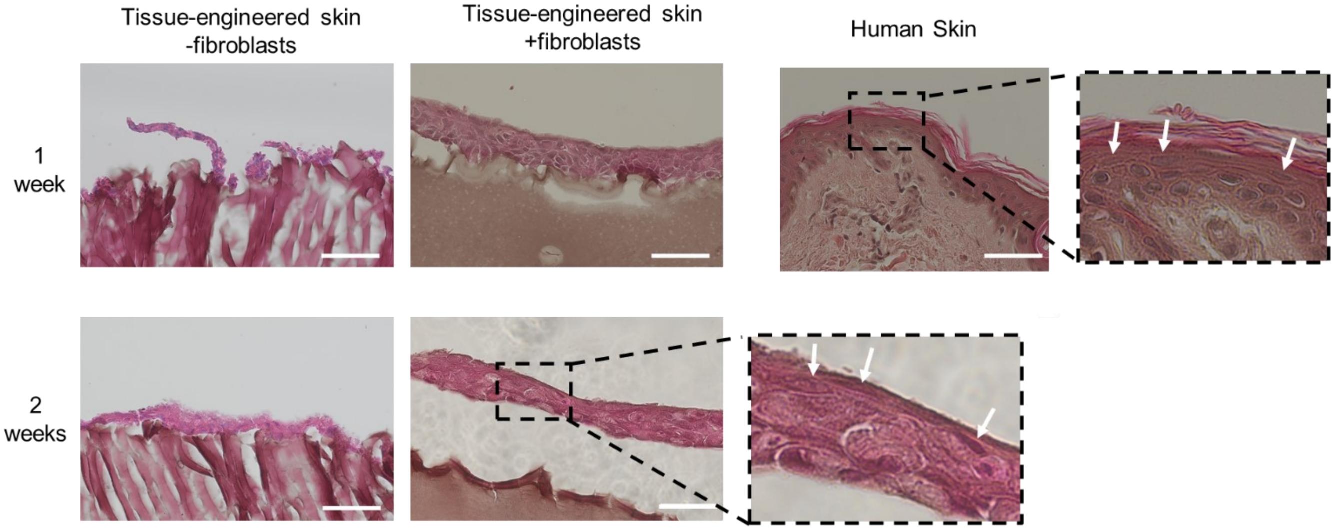

Figure 3-5: The morphology of tissue-engineered skin after 1 and 2 weeks of ALI culture with dermal fibroblasts (+fibroblasts) and without (-fibroblasts) in comparison to human skin. White arrows indicate flattened keratinocytes. Scale bars: 50 µm.

IHC analyses were performed to more clearly compare the degrees of maturation and organization between the tissue-engineered and human skin sections. Filaggrin is a marker of epidermal maturation that is present in the upper edge of the stratum granulosum and the lower stratum corneum in human skin (Fig. 3-6). Tissue-engineered skin without fibroblasts did not display a detectable level of filaggrin expression, while organized but weak expression was observed with fibroblasts after 1 week of ALI culture (Fig. 3-6). Interestingly, this the pattern of filaggrin expression is less organized after 2 weeks of ALI culture. This highlights one of the limitations of histological analysis of engineered-tissues: at each timepoint a sample must be fixed and stained, making it impossible to monitor how a single construct develops over time.

Presumably, if the +fibroblasts construct that was fixed and stained after 1 week had instead been allowed to mature for 2 weeks a stronger pattern of filaggrin expression would have been observed with similar organization, although this hypothesis is impossible to verify. Regardless, the weak filaggrin staining on the upper edge of the tissue-engineered skin after 1 week indicates that in places a mature stratum granulosum has formed. Patches of primitive stratum corneum could also be present in these regions.

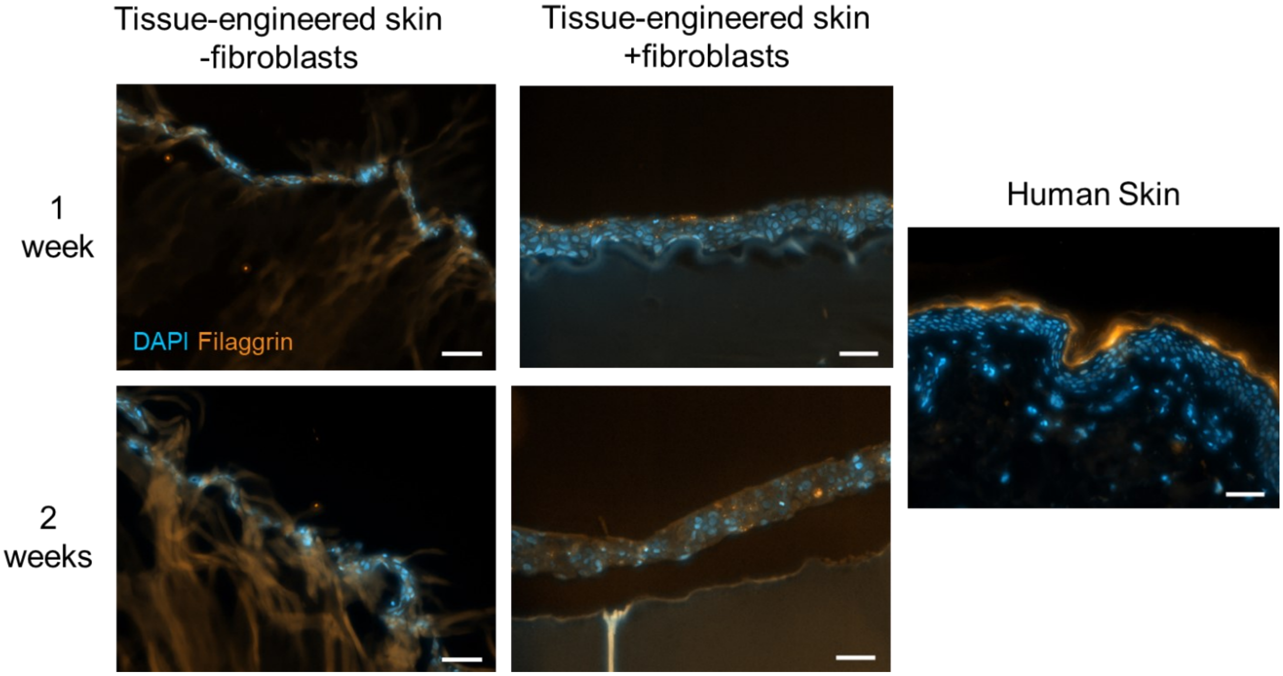

Figure 3-6: Localization of filaggrin (orange) in tissue-engineered and human skin via IHC with a nuclear counterstain (blue). Scale bars: 50 µm.

Laminin is a primary component of the basement membrane between the epidermis and dermis and various laminin isoforms are also expressed by keratinocytes in the stratum basale. This marker can be used to evaluate if the dermo-epidermal junction is intact and well developed which is indicated by a crisp difference in intensity between the basal layer and papillary dermis. Human skin stained with a pan-specific laminin antibody showed strong expression in basal keratinocytes and little to no expression in the dermis. HaCaT cells grown in 2D stain positively with this laminin antibody (data not shown), but in tissue-engineered skin without fibroblasts the intensity of laminin staining in the epidermal layer was similar to the background (Fig. 3-7 A). Tissue-engineered skin with fibroblasts showed significant laminin expression and a distinct dermo-epidermal junction, further confirming the expected organization of the tissue Fig. 3-7 B).

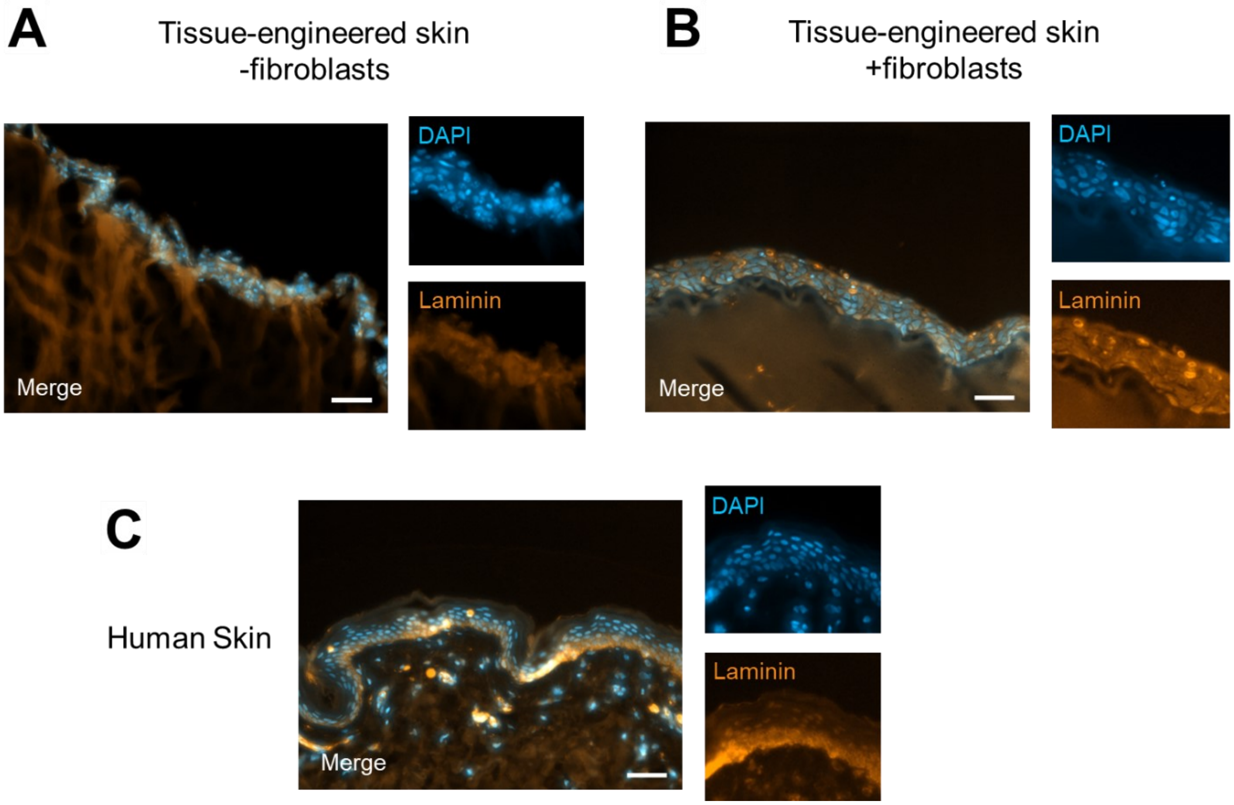

Figure 3-7: Localization of filaggrin in (A) tissue-engineered skin without fibroblasts on ALI week 2, (B) tissue-engineered skin with fibroblasts on ALI week 1, and (C) human skin. Scale bars: 50 µm.

Basal keratinocytes are the only cells that divide in the human epidermis which helps maintain the organization and define the gradient of cell maturity throughout the epidermis. Ki-67 is a nuclear protein expressed by proliferating cells during all phases of the cell cycle and is commonly used to evaluate the epidermal organization of tissue-engineered skin [37], [42], [43], [94]. The expression of Ki-67 in the tissue-engineered skin with fibroblasts was confined to a small population of basal keratinocytes as expected (Fig. 3-8). This indicates the epidermal layer of the tissue-engineered skin is developing and maturing normally and will continue to do so over time. The prevalence of Ki-67 positive basal keratinocytes is much higher in the tissue-engineered than human skin. This is also seen in many other tissue-engineered skin models [37], [42], [43] and could be attributed to the hyperproliferative nature of keratinocytes in wounds as they attempt to quickly reform a stratified epidermis from a confluent monolayer, similar to the growth pattern of keratinocytes in tissue-engineered skin..

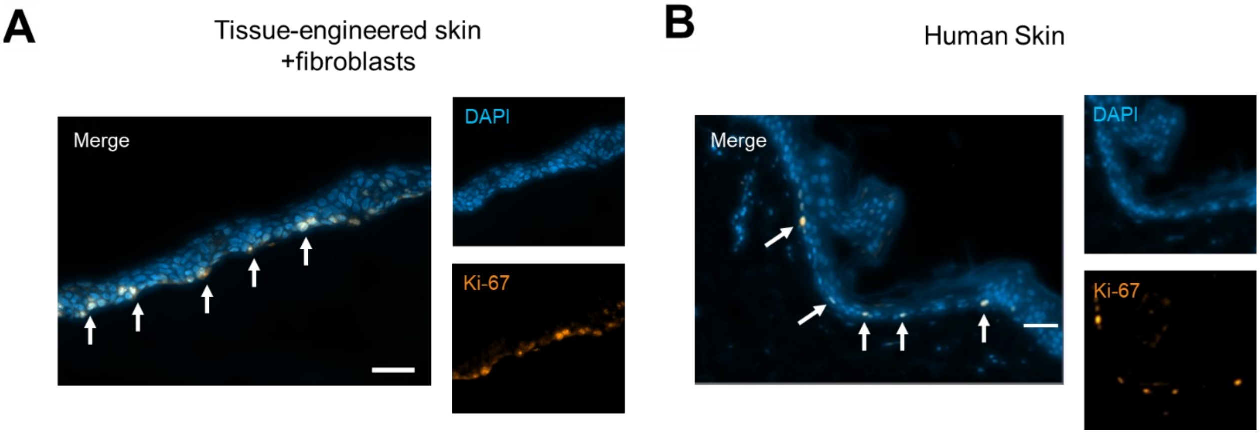

Figure 3-8: Localization of Ki-67 in (A) tissue-engineered skin +fibroblasts on ALI 1 week and (B) human skin. White arrows indicate some of the Ki-67 positive keratinocytes. Scale bars: 50 µm.

Another common method for evaluating the maturation of tissue-engineered skin is measuring the trans-epithelial electrical resistance (TEER) [40], [43], [104]. An alternating current is used to prevent damaging direct current from flowing through the cells which allows TEER to be monitored over time on the same tissues. Fig. 3-9 shows that the TEER of tissue-engineered skin after 1 week ($95.5 \pm 19.3\ \Omega\cdot\text{cm}^2$) had not increased significantly over the TEER of a GelMA hydrogel without cells ($82.8 \pm 22.6\ \Omega\cdot\text{cm}^2$, $p = 0.875$), but after 2 weeks of ALI culture the TEER had significantly increased ($169.7 \pm 19.0\ \Omega\cdot\text{cm}^2$, $p = 0.0012$) compared to the baseline. This indicates a meaningful increase in the barrier properties of the engineered tissue. However, the

TEER after 2 weeks of ALI was still significantly lower than that of human skin (268.3 ± 28.5 Ω·cm^2, p = 0.0009). Further cornification and the formation of a fully-developed stratum corneum would likely be required for the tissue-engineered skin to have a similar TEER to human skin.

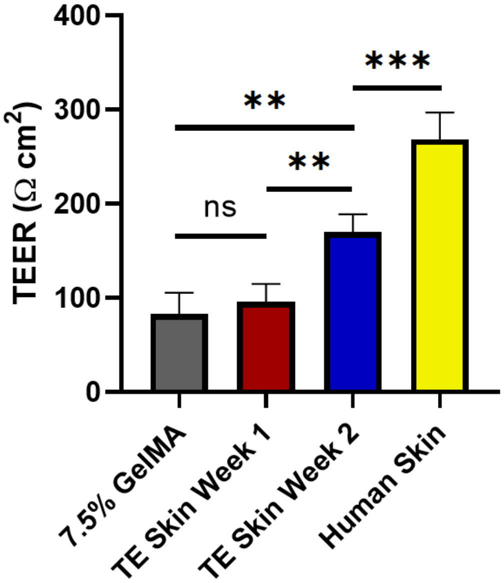

*Figure 3-9: Comparison of the TEER of GelMA hydrogel, tissue-engineered skin, and human skin (*p<0.05, **p<0.01, ***p<0.001).*

3.5 Conclusion

The tissue morphology, protein expression patterns, and electrical resistance of the tissue-engineered skin were evaluated and compared to human skin. While the tissue-engineered skin did not have a fully developed stratum corneum, highly flattened keratinocytes are present, indicating that the stratum spinosum, stratum granulosum and a potentially a portion of the stratum corneum are present. This is supported by the presence of slight filaggrin expression on the upper edge of the epidermal layer, which is usually found on the upper edge of the stratum granulosum and throughout the lower stratum corneum in normal human skin. The presence of an intact dermo-epidermal junction was confirmed by laminin staining. Ki-67 expression was used to determine that cell proliferation within the tissue-engineered skin was limited to basal keratinocytes as expected. Finally, the electrical resistance of the tissue-engineered skin was found to be significantly higher than the resistance of the GelMA hydrogel, but lower the TEER of human skin, again indicating that the tissue-engineered skin had matured to a significant degree. These verifications confirm that the tissue-engineered skin has an organized structure and has matured considerably, albeit without a complete stratum corneum. In its current state, the tissue-engineered skin model developed is not appropriate for mimicking the barrier properties of skin for drug or cosmetics testing, but is suitable for studying healing in chronic wounds.

During culture at the ALI, the epidermal layer is exposed to the air inside the incubator which has a relative humidity of over 95%. Although this is common practice for developing tissue-engineered skin, the humidity is substantially higher than the typical humidity that human skin experiences on a day-to-day basis. It is tempting to hypothesize that reducing the humidity during ALI culture will either increase the speed or final degree of epidermal maturation; however further experiments would be necessary to confirm this hypothesis.

Chapter 4 – Healing of Infected *in Vitro* Wounds

Ultimately, tissue-engineered skin is only useful for modelling chronic wounds if it can be artificially wounded and subsequently shows healing *in vitro*. Bacterial infection plays an important role in chronic wounds and ideally should be included in an *in vitro* wounding experiment to mimic the chronic wound environment. As a proof-of-concept, an infected wound healing experiment was performed on the tissue-engineered skin to determine firstly if it is capable of healing, and secondly how bacterial infection influences healing. The depth of the wound and the species of bacteria used must be chosen strategically for the results to be relevant to chronic wounds.

There are two major options for the depth of the wound: it can either penetrate only the epidermis, or both the epidermis and dermis. While a wound that damages the dermis is more representative of the chronic wound environment, it is challenging to implement on tissue-engineered skin due to the soft nature of the hydrogel. Additionally, an artificial wound that removes part of the dermis will provide a rough or uneven hydrogel surface that may impede reepithelialisation. Manuela *et al.* demonstrated that it is possible to inject a collagen hydrogel into a full-thickness *in vitro* wound and observed reepithelialisation on the flat upper surface of the injected hydrogel (Fig. 1-7 A); however, a simpler approach was desired for this proof-of-concept experiment. Scratch assays are commonly used in 2D culture experiments with HaCaT cells to observe to speed or degree of reepithelialisation in response to pharmaceuticals, conditioned media, or infection [50], [105], [106]. Typically, a single line is scratched into a confluent monolayer of keratinocytes with a pipette tip. Keratinocytes from either side of the scratch migrate and proliferate to fill the void over time (Fig. 1-7 B). This reproducible and easy to implement wounding method was chosen to evaluate the healing of the tissue-engineered skin.

P. aeruginosa is one of the most common bacteria found in chronic wounds [107], [108] and has been extensively studied with *in vitro* models (Table 1-2). *P. aeruginosa* has also demonstrated an ability to form biofilms *in vitro* [16], [55]. For these reasons *P. aeruginosa* was chosen to infect the tissue-engineered wound. *P. aeruginosa* is gram-negative with a rod-shaped structure and a single polar flagellum that provides motility [107], [109].

4.1 Materials and Methods

P. aeruginosa, tryptic soy agar (Sigma-Aldrich, cat#: 22091), tryptic soy broth (Sigma-Aldrich, cat#: 22092), and ciprofloxacin HCl (Sigma-Aldrich, cat#: PHR1044) were used for bacteria culture and infection experiments.

High binding microplates (Greiner Bio., cat#: 655081), 3,3',5,5'-tetramethylbenzidine (TMB substrate, Sigma-Aldrich, cat#: T0440), and a mini TMB ELISA kit for TNF-α (PeproTech, cat#: 900-TM25) were used for quantifying pro-inflammatory cytokine production.

4.1.1 *P. Aeruginosa* Culture

P. aeruginosa was streaked onto tryptic soy agar (TSA) plates and cultured at 37ºC in a normal atmosphere. When necessary, a single colony was suspended in tryptic soy broth, vortexed to homogenize the solution, and the optical density (O.D) at 600 nm was measured in triplicate on a microplate reader.

4.1.2 Artificial Wounding of the Tissue-Engineered Skin

Tissue-engineered skin after 14 days ALI culture was used for all wounding experiments. All media was aspirated and each Transwell insert was individually transferred to a sterile petri dish for wounding. Sharp tweezers were sterilized with 70% ethanol then used to create roughly circular artificial wounds in the epidermal layer of the tissue-engineered skin. An inverted microscope was used to confirm that the epidermis was completely removed from the wound bed; the wound surface was scratched again if keratinocytes were still present.

4.1.3 Infection and Treatment of the *in vitro* Wound

A single *P. aeruginosa* colony was inoculated in tryptic soy broth and diluted to create a solution with an O.D. (600 nm) of 0.4. The bacteria were centrifuged and resuspended in an equal volume of DMEM without antibiotics. The wounded tissue-engineered skin was washed once with DMEM without antibiotics and then divided into three groups, control, infected, and treated, each containing 4 biological replicates. Each group was transferred to its own separate well plate to prevent cross-contamination. The infected and treated groups were both inoculated with 10 µl of the *P. aeruginosa* solution which was pipetted directly onto the artificial wound and incubated at 37ºC for 2 hours to allow bacteria to adhere to the wound. After the incubation, antibiotic-free proliferation media was added to the Transwell compartments of the control and infected groups. Proliferation media containing 0.4 µg/mL ciprofloxacin, a concentration shown to be non-cytotoxic to HaCaT cells [50], was added to the Transwell compartments of the treated group. The submerged culture conditions mimic the moist healing environment that is desired in clinical wound care.

4.1.4 ELISA Analysis of Pro-Inflammatory Cytokines

On ALI days 4 and 14 (before infection) the culture media was removed from 3 wells and stored at -80 ºC. At 24 and 48 hours after infection, the media was aspirated from the Transwell compartments and either stored at -80 ºC or used immediately.

An enzyme-linked immunosorbent assay (ELISA) was used to detect TNF-α, a pro-inflammatory cytokine, in the culture media during normal growth and after wounding. Samples were diluted 1:3 in diluent to ensure they fell within the detectable range of the assay (16-2000 pg/mL). The manufacturer's detailed instructions were followed exactly to perform the assay. Briefly, wells were incubated with the capture antibody overnight then washed 4 times with washing buffer. The standard was serially diluted by factors of 2 from 2000 pg/mL down to 15 pg/mL in triplicate. The standard or a diluted sample (1:3) was added to each well and incubated at room temperature for 2 hours. After 4 washes, the detection antibody was added and incubated for 2 additional hours at room temperature. Streptavidin-HRP working solution was added to each well for 30 minutes then replaced with the TMB substrate. Colour developed over the 20 minutes TMB incubation which was promptly stopped by adding 1M HCl. Results were read on a microplate reader at 450 nm with reference wavelength correction at 620 nm. A linear trendline fit well to the standard curve with R^2=0.9946 (Fig. 4-1).

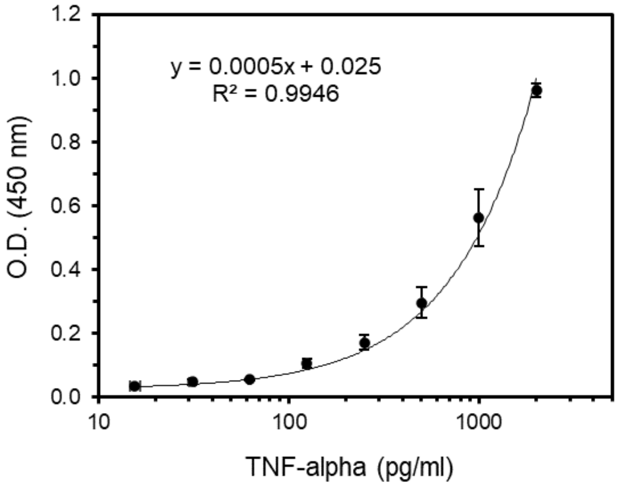

Figure 4-1: Standard curve for the detection of TNF-α with ELISA.

4.1.5 Statistical Analysis

All data was displayed as the mean plus or minus one standard deviation. Microsoft Excel was used to process the ELISA data and plot the TNF-α standard curve. GraphPad Prism 8 was used to plot and analyze the experimental TNF-α results. A two-way ANOVA was conducted using Tukey's multiple comparisons test to compare the TNF-α production between conditions at each timepoint ($\alpha = 0.05$).

4.2 Results and Discussion

When attempting to create a scratch wound on the epidermal surface it quickly became apparent that the conventional technique of creating the scratch with a pipette tip would be unsuccessful. Even when applying significant pressure, the pipette slid across the surface without creating damage visible to either the naked eye or under the microscope. In hindsight, this scratch resistance should have been predicted based on the histological, IHC, and TEER analyses which demonstrated the epidermis had matured and stratified. The resistance of the epidermis to scratching further supports the hypothesis that the epidermal layer has matured to a significant degree. Eventually, tweezers with a sharp point were found to be suitable for creating a scratch in the epidermis. The sharp point was used to puncture the epidermis and then the epidermis was gently pulled away from the puncture point, creating a circular epidermal wound approximately 1 mm in diameter (Fig. 4-2).

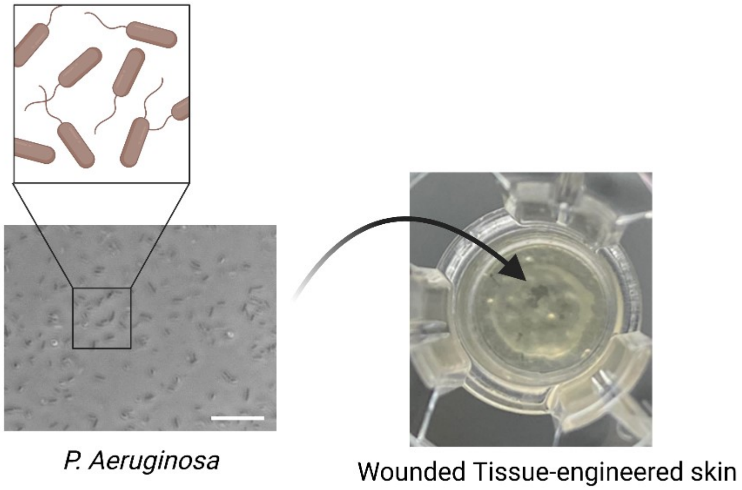

Figure 4-2:Infection of in vitro wound with P. aeruginosa

4.2.1 Reepithelialisation of the *in Vitro* Wound

Healing was compared between infected wounds, infected wounds treated with antibiotics (ciprofloxacin), and uninfected control wounds. All wounds were gently washed once before imaging to remove unattached keratinocytes or bacteria. After the injury there were no keratinocytes on the wound surface in all conditions (Fig. 4-3). *P. aeruginosa* can be seen as small black dots (Fig. 4-3, white arrows) on the infected and treated wounds following a 2-hour incubation for bacteria attachment. The bacteria are highly motile in the infected condition (antibiotic free media) and much less motile in the treated condition (DMEM + ciprofloxacin). Significant reepithelialisation is seen on the bed of the control wound by 48 hours after injury, none is seen on the infected wounds, and some reepithelialisation is seen on the treated wounds but less than the control. No bacteria were observed in the control or treated wounds after 48 hours and as expected, the infected wounds were overcome by bacteria at this timepoint. While some planktonic (individual) bacteria were present, the majority of the infected wound bed was covered in numerous motile conglomerations approximately 10-20 μm in diameter which could be seen converging with and separating from each other over time. Presumably, these are the beginnings of a biofilm, which consist of bacteria surrounded by a dense matrix of proteins, polysaccharides, and lipids (Fig. 1-5).

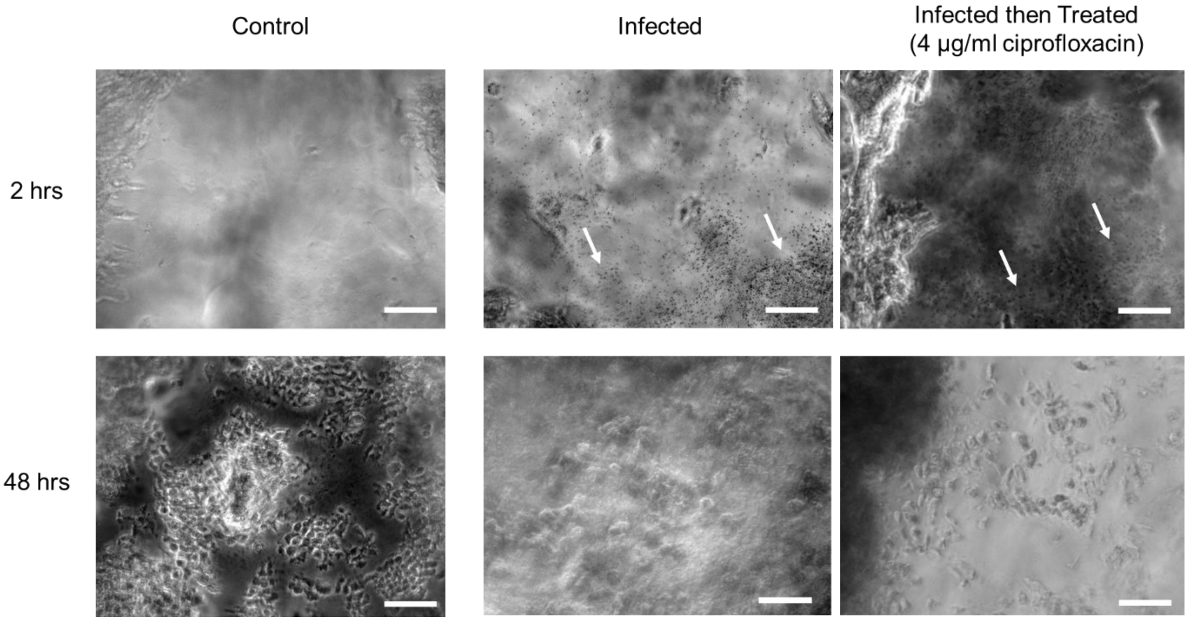

Figure 4-3: Reepithelialisation and bacterial colonization on uninfected (control), infected, and treated wounds in tissue-engineered skin. Scale bars: 50 μm.

4.2.1 Pro-inflammatory Cytokine Production

The influence of the wound and subsequent infection on the keratinocytes and fibroblasts in the tissue-engineered skin was investigated by quantifying their production of TNF-α, a pro-inflammatory cytokine. Bacterial pathogens, ultraviolet radiation, and physical injuries have all been shown to stimulate TNF-α release by human keratinocytes or fibroblasts [50], [52], [110]. A baseline of low TNF-α expression on ALI day 4 and 14 was established (~30 pg/mL), demonstrating that inflammatory pathways are not active during the maturation of the tissue-engineered skin (Fig. 4-4 A). 24 hours after wounding, 1 or 2 of the 4 replicates for each condition showed TNF-α production many times above the baseline while the other replicates continued to produce baseline levels (Fig. 4-4 B). At this timepoint there were minimal, statistically insignificant differences between the average TNF-α production in the control, infected, and treated conditions; however, 48 hours after wounding, TNF-α production was significant higher in the infected wounds (478 ± 324.8 pg/mL) compared to both the control (26.1 ± 10.9 pg/mL, p = 0.033) and treated wounds (12.3 ± 6.3 pg/mL, p = 0.028). This trend confirms that bacteria persist in the infected wound bed for 48 hours and that the ciprofloxacin treatment was successful at treating the infection. The wide distribution of TNF-α production after 24 hours may have been caused by variations in the physical wounding procedure between replicates. Modifying the wounding procure to be more consistent is one of the next steps for improving this *in vitro* wound model.

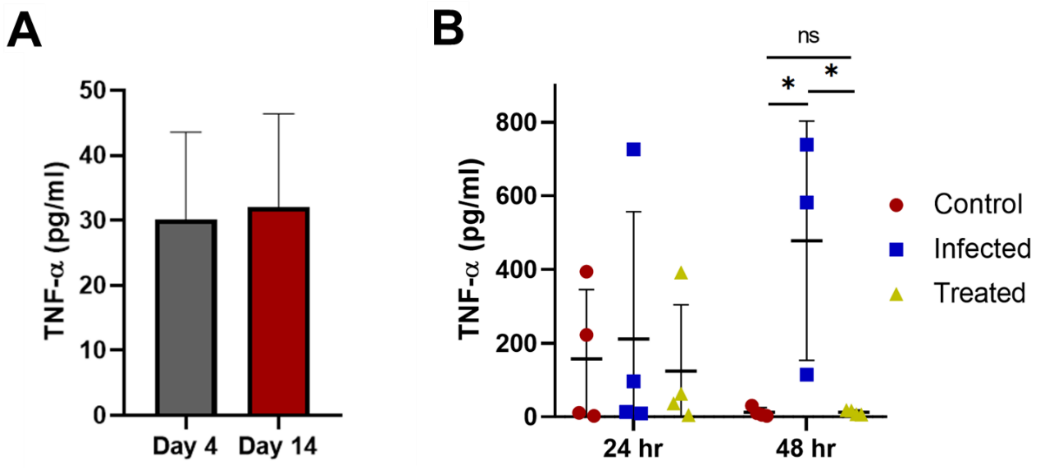

*Figure 4-4:Production of the pro-inflammatory cytokine TNF-α in tissue-engineered skin (A) during maturation at the ALI and (B) after wounding and infection (*p<0.05).*

After 4 days of culture, bacteria in the infected wounds had mostly concentrated into a smaller region of the wound (<50% of the total area) and formed an opaque layer that was not possible to image with a brightfield microscope at higher magnification (Fig. 4-5). Highly motile bacteria were observed on the borders of this dark region in the wound. Considering that this was not removed by washing, and that much smaller (10 - 20 μm) conglomerates of bacteria were observed after 2 days, a biofilm has likely formed on the wound after 4 days of infection. Further analysis would be required to confirm this hypothesis.

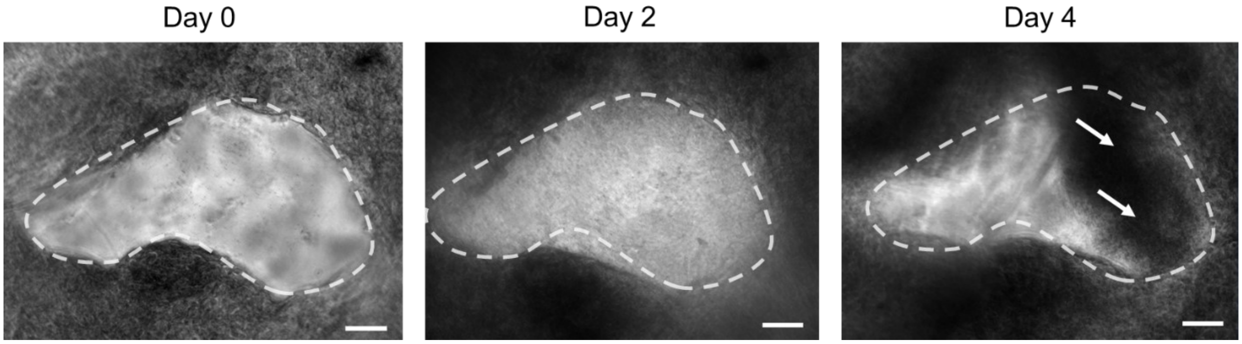

Figure 4-5: Progression of infection in an artificial wound. White arrows indicate bacteria. Scale bars: 100 μm.

4.3 Conclusion

This experiment demonstrated that the tissue-engineered skin developed in this work is indeed capable of acting as an *in vitro* model of infected and non-infected wound healing. Uninfected wounds showed significant reepithelialisation after 48 hours while infected wounds were overcome by bacteria and potentially covered by a biofilm after 4 days of infection.

A more consistent method of creating the physical wound and a technique for evaluating biofilm formation should be both be developed before the model is used further. While a wound that penetrated only the epidermis was initially chosen due to simplicity, this was challenging to implement on an epidermal layer strong enough to resist scratching. Using a biopsy punch to remove a full-thickness segment of skin as demonstrated by Manuela *et al.* will be more reproducible and also will provide a better representation of a chronic wound where the dermis is also damaged [49]. To more clearly show the development of biofilms on the *in vitro* wound, regions of interest could be investigated with SEM, periodic acid–Schiff (PAS) staining, or polymerase chain reaction (PCR). SEM images of a biofilm will clearly show individual bacteria on the surface or protruding into a dense matrix [16], [25]. PAS staining detects the presence of polysaccharides which are a major component of the biofilm matrix. Although more labour intensive, PCR could also be used to detect the up-regulated expression of biofilm-associated proteins [111].

Chapter 5 - Conclusion and Future Work

The wound model presented in this work has many advantages over existing *in vitro* models of chronic or infected wounds. Unlike many alternatives (Table 1-2) [50]–[52], this model includes both human keratinocytes and dermal fibroblasts which have important roles in producing ECM and reepithelialising the wound surface. The combination of keratinocytes and fibroblasts with infection allows for the influence of bacteria on healing to be observed in a highly controllable environment. DLP bioprinting also enables arrays of 15 constructs to be bioprinted simultaneously, improving the feasibility of using this model for high throughput testing.

The *in vitro* wound model developed herein is capable of healing but admittedly requires slight improvements before it can reliably mimic the chronic wound environment. At minimum, this includes improving the method for creating the physical wound and developing a technique for visualizing biofilm formation on the wound. A potential method of creating the physical wound is to remove a full-thickness segment of tissue with a biopsy punch and fill the void with a hydrogel. Keratinocytes would then reepithelialise over the surface of the hydrogel to close the wound (Fig. 1-7). As discussed thoroughly in Chapter 1, immune cells such as neutrophils and macrophages play a prominent role in the persistent inflammation seen in many chronic wounds. Macrophages such as the THP-1 monocyte line could easily be added to the surface of the wound bed with or without bacteria to investigate how their interactions influence reepithelialisation. This situation could potentially imitate the persistent inflammation in chronic wounds and would be very valuable for investigating therapies to propel the wound out of inflammatory phase. Supernatant from the *in vitro* wound could be analysed with ELISA to quantify the presence of cytokines, MMPs, and TIMPs in the wound. This would provide a picture of inflammatory state of the wound and balance between MMPs and TIMPs that could be monitored over time. If the biopsy punch method is chosen to create the physical wound, immune cells could be encapsulated in the hydrogel used to fill the gap in the tissue, which would be very similar to the *in vivo* situation where immune cells enter the wound from the vasculature below. Such a model would be the most sophisticated *in vitro* chronic wound model available and would be well-poised to improve the *in vitro* testing of novel chronic wound therapies such as wound dressings, drugs, biosensors, or growth factors. The adaptability of DLP bioprinting can also be leveraged in future work to study the effects of different wound sizes and shapes. Chronic wounds have a diverse range of surface areas, shapes, and depths [1], [112]. After designing the appropriate CAD models, tissue-engineered skin wounds that capture these differences can be produced through DLP bioprinting and used to study how the wound geometry influences healing and potential treatments.

More generally, this work is also a significant contribution to the field of skin tissue engineering as it is the first demonstration and characterization of full-thickness skin formed with a DLP bioprinting approach. The optimized DLP bioprinting parameters (Table 2-2), optimized GelMA concentration based on the characterizations in Chapter 2, and the technique for establishing and maturing the epidermal layer as explained in Chapter 3 can all be directly adopted by other researchers in the future. These provide the building blocks for using DLP bioprinting to incorporate relevant microscale features of skin such as vasculature, rete ridges, nerves, or hair follicles into tissue-engineered models. This will allow future research to concentrate more on the functional analysis of complex geometries and spend less time optimizing the bioprinting approach.

The approach of DLP bioprinting GelMA laden with fibroblasts could also be useful for creating tissue-engineered models of other connective tissues that consist of a low number of fibroblasts in a matrix of collagen fibers. The submucosa of the digestive tract, bone marrow, or organ capsules all have such an organization and these tissues could be mimicked *in vitro* with a very similar approach. This work demonstrated that an epithelial sheet could be formed on one surface of the bioprinted constructs. By replacing the keratinocytes with a different cell type, epithelial tissues such as the intestinal mucosa or pulmonary epithelium could be mimicked *in vitro*. Furthermore, DLP bioprinting also opens up the possibilities of creating complex structures with cavities or hollow vessels which allows this approach to also be extended to endothelial tissues including blood vessels or lymphatics.

References

[1] L. M. Morton and T. J. Phillips, “Wound healing and treating wounds: Differential diagnosis and evaluation of chronic wounds,” *J. Am. Acad. Dermatol.*, vol. 74, no. 4, pp. 589–605, Apr. 2016.

[2] A. J. Singer and R. A. F. Clark, “Cutaneous wound healing,” *N. Engl. J. Med.*, vol. 341, no. 10, pp. 738–746, Sep. 1999.

[3] V. Blanchette and J. L. Kuhnke, “The Current Situation for Non-healing Wounds,” *Wound Care Canada*, vol. 19, no. 1, pp. 60–69, 2021.

[4] L. Martinengo *et al.*, “Prevalence of chronic wounds in the general population: systematic review and meta-analysis of observational studies,” *Annals of Epidemiology*, vol. 29. Elsevier, pp. 8–15, 01-Jan-2019.

[5] T. Hurd and J. Posnett, “Point prevalence of wounds in a sample of acute hospitals in Canada,” *Int. Wound J.*, vol. 6, pp. 287–293, 2009.

[6] E. Eriksson *et al.*, “Chronic wounds: Treatment consensus,” *Wound Repair Regen.*, vol. 30, no. 2, pp. 156–171, Mar. 2022.

[7] P. Krzyszczyk, R. Schloss, A. Palmer, and F. Berthiaume, “The role of macrophages in acute and chronic wound healing and interventions to promote pro-wound healing phenotypes,” *Front. Physiol.*, vol. 9, no. 419, May 2018.

[8] J. Larouche, S. Sheoran, K. Maruyama, and M. M. Martino, “Immune regulation of skin wound healing: Mechanisms and novel therapeutic targets,” *Adv. Wound Care*, vol. 7, no. 7, pp. 209–231, Jul. 2018.

[9] S. Liarte, Á. Bernabé-García, and F. J. Nicolás, “Role of TGF-β in Skin Chronic Wounds: A Keratinocyte Perspective,” *Cells*, vol. 9, no. 2, p. 306, Jan. 2020.

[10] S. Werner and R. Grose, “Regulation of Wound Healing by Growth Factors and Cytokines,” *Physiol. Rev.*, vol. 83, pp. 835–870, 2003.

[11] R. Blakytny and E. Jude, “The molecular biology of chronic wounds and delayed healing

in diabetes," *Diabet. Med.*, vol. 23, no. 6, pp. 594–608, Jun. 2006.

[12] I. A. Darby, B. Laverdet, F. Bonté, and A. Desmoulière, "Fibroblasts and myofibroblasts in wound healing," *Clinical, Cosmetic and Investigational Dermatology*, vol. 7. Dove Medical Press Ltd., pp. 301–311, 06-Nov-2014.

[13] L. E. Tracy, R. A. Minasian, and E. J. Caterson, "Extracellular Matrix and Dermal Fibroblast Function in the Healing Wound," *Adv. Wound Care*, vol. 5, no. 3, pp. 119–136, 2016.

[14] T. T. Nguyen *et al.*, "Translational pharmacology Expression of active matrix metalloproteinase-9 as a likely contributor to the clinical failure of aclerastide in treatment of diabetic foot ulcers," 2018.

[15] A. Parnham and C. Bousfield, "The influence of matrix metalloproteases and biofilm on chronic wound healing: A discussion," *Br. J. Community Nurs.*, vol. 23, pp. S22–S29, Mar. 2018.

[16] M. Ashrafi *et al.*, "Validation of biofilm formation on human skin wound models and demonstration of clinically translatable bacteria-specific volatile signatures," *Sci. Rep.*, vol. 8, no. 1, pp. 1–16, 2018.

[17] A. Grada, J. Mervis, and V. Falanga, "Research Techniques Made Simple: Animal Models of Wound Healing," *J. Invest. Dermatol.*, vol. 138, no. 10, pp. 2095-2105.e1, Oct. 2018.

[18] H. Shimizu, "Structure and Function of the Skin," in *Shimizu's Dermatology, Second Edition*, 2017, pp. 1–42.

[19] S. Han, "Basics of Wound Healing," in *Innovations and Advances in Wound Healing*, Berlin, Heidelberg: Springer, 2016, pp. 1–37.

[20] M. Martin, "Physiology of Wound Healing," in *Wound Healing and Skin Integrity: Principles and Practice*, 2013, pp. 33–48.

[21] N. J. Trengove, H. Bielefeldt-Ohmann, and M. C. Stacey, "Mitogenic activity and cytokine levels in non-healing and healing chronic leg ulcers," *Wound Repair Regen.*, vol. 8, no. 1,

pp. 13–25, Jan. 2000.

[22] N. J. Trengove *et al.*, “Analysis of the acute and chronic wound environments: the role of proteases and their inhibitors,” *Wound Repair Regen.*, vol. 7, no. 6, pp. 442–452, Nov. 1999.

[23] D. R. Yager, S. M. Chen, S. I. Ward, O. O. Olutoye, R. F. Diegelmann, and I. K. Cohen, “Ability of chronic wound fluids to degrade peptide growth factors is associated with increased levels of elastase activity and diminished levels of proteinase inhibitors,” *Wound Repair Regen.*, vol. 5, no. 1, pp. 23–32, Jan. 1997.

[24] T. N. Demidova-Rice, M. R. Hamblin, and I. M. Herman, “Acute and Impaired Wound Healing: Pathophysiology and Current Methods for Drug Delivery, Part 1: Normal and Chronic Wounds: Biology, Causes, and Approaches to Care,” *Adv. Skin Wound Care*, vol. 25, no. 7, p. 304, Jul. 2012.

[25] G. A. James *et al.*, “Biofilms in chronic wounds,” *Wound Repair Regen.*, vol. 16, no. 1, pp. 37–44, Jan. 2008.

[26] Y. K. Wu, N. C. Cheng, and C. M. Cheng, “Biofilms in Chronic Wounds: Pathogenesis and Diagnosis,” *Trends Biotechnol.*, vol. 37, no. 5, pp. 505–517, May 2019.

[27] R. F. Diegelmann, “Excessive neutrophils characterize chronic pressure ulcers,” *Wound Repair Regen.*, vol. 11, no. 6, pp. 490–495, Nov. 2003.

[28] H. C. Flemming, J. Wingender, U. Szewzyk, P. Steinberg, S. A. Rice, and S. Kjelleberg, “Biofilms: an emergent form of bacterial life,” *Nat. Rev. Microbiol. 2016 149*, vol. 14, no. 9, pp. 563–575, Aug. 2016.

[29] O. Sarheed, A. Ahmed, D. Shouqair, and J. Boateng, “Antimicrobial Dressings for Improving Wound Healing,” in *Wound Healing - New insights into Ancient Challenges*, IntechOpen, 2016, pp. 374–398.

[30] J. M. Davidson, “First-Class Delivery: Getting Growth Factors to Their Destination,” *J. Invest. Dermatol.*, vol. 128, no. 6, pp. 1360–1362, Jun. 2008.

[31] C. J. Van Koppen and R. W. Hartmann, “Advances in the treatment of chronic wounds: a patent review,” *http://dx.doi.org/10.1517/13543776.2015.1045879*, vol. 25, no. 8, pp. 931–

937, Aug. 2015.

[32] C. K. Sen *et al.*, “Human skin wounds: A major and snowballing threat to public health and the economy,” *Wound Repair and Regeneration*, vol. 17, no. 6. NIH Public Access, pp. 763–771, Nov-2009.

[33] J. Wu, Y. Zheng, X. Wen, Q. Lin, X. Chen, and Z. Wu, “Silver nanoparticle/bacterial cellulose gel membranes for antibacterial wound dressing: investigation in vitro and in vivo,” *Biomed. Mater.*, vol. 9, no. 3, p. 035005, Apr. 2014.

[34] T. Eberlein *et al.*, “Comparison of PHMB-containing dressing and silver dressings in patients with critically colonised or locally infected wounds,” *J. Wound Care*, vol. 21, no. 1, pp. 12–20, 2012.

[35] E. Bell, H. P. Ehrlich, D. J. Buttle, and T. Nakatsuji, “Living Tissue Formed in Vitro and Accepted as Skin-Equivalent Tissue of Full Thickness,” *Science (80-.).*, vol. 211, no. 4486, pp. 1052–1054, 1981.

[36] R. Jin *et al.*, “Three-dimensional bioprinting of a full-thickness functional skin model using acellular dermal matrix and gelatin methacrylamide bioink,” *Acta Biomater.*, vol. 131, pp. 248–261, Sep. 2021.

[37] B. S. Kim, G. Gao, J. Y. Kim, and D. W. Cho, “3D Cell Printing of Perfusable Vascularized Human Skin Equivalent Composed of Epidermis, Dermis, and Hypodermis for Better Structural Recapitulation of Native Skin,” *Adv. Healthc. Mater.*, vol. 8, no. 7, pp. 1–11, 2019.

[38] F. Kreimendahl *et al.*, “Macrophages significantly enhance wound healing in a vascularized skin model,” *J. Biomed. Mater. Res. - Part A*, vol. 107, no. 6, pp. 1340–1350, 2019.

[39] Z. Shen *et al.*, “Construction of tissue-engineered skin with rete ridges using co-network hydrogels of gelatin methacrylated and poly(ethylene glycol) diacrylate,” *Mater. Sci. Eng. C*, p. 112360, Aug. 2021.

[40] X. Liu, S. Michael, K. Bharti, M. Ferrer, and M. J. Song, “A biofabricated vascularized skin model of atopic dermatitis for preclinical studies,” *Biofabrication*, vol. 12, p. 035002, 2019.

[41] E. M. Haisma, M. H. Rietveld, A. Breij, J. T. Van Dissel, A. El Ghalbzouri, and P. H. Nibbering, "Inflammatory and Antimicrobial Responses to Methicillin-Resistant Staphylococcus aureus in an In Vitro Wound Infection Model," *PLoS One*, vol. 8, no. 12, p. e82800, Dec. 2013.

[42] T. Baltazar *et al.*, "Three Dimensional Bioprinting of a Vascularized and Perfusable Skin Graft Using Human Keratinocytes, Fibroblasts, Pericytes, and Endothelial Cells," *Tissue Eng. Part A*, vol. 26, no. 5, pp. 227–238, 2020.

[43] X. Zhao *et al.*, "Photocrosslinkable Gelatin Hydrogel for Epidermal Tissue Engineering," *Adv. Healthc. Mater.*, vol. 5, pp. 108–118, 2016.

[44] B. S. Kim *et al.*, "3D cell printing of in vitro stabilized skin model and in vivo pre-vascularized skin patch using tissue-specific extracellular matrix bioink: A step towards advanced skin tissue engineering," *Biomaterials*, vol. 168, pp. 38–53, 2018.

[45] N. Barros *et al.*, "Biofabrication of endothelial cell, dermal fibroblast, and multilayered keratinocyte layers for skin tissue engineering," *Biofabrication*, vol. 13, no. 035030, 2020.

[46] L. Costello *et al.*, "Engineering a Multilayered Skin Equivalent: The Importance of Endogenous Extracellular Matrix Maturation to Provide Robustness and Reproducibility," in *Skin Tissue Engineering: Methods and Protocols*, vol. 1993, 2019, pp. 107–122.

[47] A. Monfort, M. Soriano-Navarro, J. M. García-Verdugo, and A. Izeta, "Production of human tissue-engineered skin trilayer on a plasma-based hypodermis," *J. Tissue Eng. Regen. Med.*, vol. 7, no. 6, pp. 479–490, 2013.

[48] S. Kadam, S. Nadkarni, J. Lele, S. Sakhalkar, P. Mokashi, and K. S. Kaushik, "Bioengineered Platforms for Chronic Wound Infection Studies: How Can We Make Them More Human-Relevant?," *Frontiers in Bioengineering and Biotechnology*, vol. 7. Frontiers Media S.A., p. 418, 13-Dec-2019.

[49] B. Manuela, K. Milad, S. Anna-Lena, R. Julian-Dario, and S. Ewa Klara, "Acute and Chronic Wound Fluid Inversely Influence Wound Healing in an in-Vitro 3D Wound Model," *J. Tissue Repair Regen.*, vol. 1, no. 1, pp. 1–11, Dec. 2017.

[50] M. Jahanshahi *et al.*, "An Engineered Infected Epidermis Model for In Vitro Study of the

Skin's Pro-Inflammatory Response," *Micromachines*, vol. 11, no. 2, 2020.

[51] P. M. Alves, E. Al-Badi, C. Withycombe, P. M. Jones, K. J. Purdy, and S. E. Maddocks, "Interaction between Staphylococcus aureus and Pseudomonas aeruginosa is beneficial for colonisation and pathogenicity in a mixed biofilm," *Pathog. Dis.*, vol. 76, no. 1, p. 3, Feb. 2018.

[52] A. Tankersley, M. B. Frank, M. Bebak, and R. Brennan, "Early effects of Staphylococcus aureus biofilm secreted products on inflammatory responses of human epithelial keratinocytes," *J. Inflamm. (Lond).*, vol. 11, no. 1, p. 17, 2014.

[53] F. Ellett *et al.*, "Microfluidic arenas for war games between neutrophils and microbes," *Lab Chip*, vol. 19, no. 7, pp. 1205–1216, Mar. 2019.

[54] A. R. Hauser and J. N. Engel, "Pseudomonas aeruginosa induces type-III-secretion-mediated apoptosis of macrophages and epithelial cells," *Infect. Immun.*, vol. 67, no. 10, pp. 5530–5537, 1999.

[55] M. Werthén, L. Henriksson, P. Ø. Jensen, C. Sternberg, M. Givskov, and T. Bjarnsholt, "An in vitro model of bacterial infections in wounds and other soft tissues," *APMIS*, vol. 118, no. 2, pp. 156–164, Feb. 2010.

[56] B. L. Price, A. M. Lovering, F. L. Bowling, and C. B. Dobson, "Development of a novel collagen wound model to simulate the activity and distribution of antimicrobials in soft tissue during diabetic foot infection," *Antimicrob. Agents Chemother.*, vol. 60, no. 11, pp. 6880–6889, 2016.

[57] M. Ahearne, "Introduction to cell–hydrogel mechanosensing," *Interface Focus*, vol. 4, no. 2, Apr. 2014.

[58] H. Li, M. Bao, and Y. Nie, "Extracellular matrix–based biomaterials for cardiac regeneration and repair," *Heart Fail. Rev.*, 2020.

[59] S. L. Bellis, "Advantages of RGD peptides for directing cell association with biomaterials," *Biomaterials*, vol. 32, no. 18, pp. 4205–4210, 2011.

[60] A. Tamayol, M. Akbari, N. Annabi, A. Paul, A. Khademhosseini, and D. Juncker, "Fiber-

based tissue engineering: Progress, challenges, and opportunities," *Biotechnol. Adv.*, vol. 31, no. 5, pp. 669–687, 2013.

[61] N. Annabi *et al.*, "25th Anniversary Article: Rational Design and Applications of Hydrogels in Regenerative Medicine," *Adv. Mater.*, vol. 26, no. 1, pp. 85–124, 2014.

[62] M. H. Jung, S. M. Jung, and H. S. Shin, "Co-stimulation of HaCaT keratinization with mechanical stress and air-exposure using a novel 3D culture device," *Sci. Rep.*, vol. 6, no. September, pp. 1–7, 2016.

[63] A. Lee *et al.*, "3D bioprinting of collagen to rebuild components of the human heart," *Science (80-.).*, vol. 365, pp. 482–487, 2019.

[64] R. A. Li *et al.*, "Bioengineering an electro-mechanically functional miniature ventricular heart chamber from human pluripotent stem cells," *Biomaterials*, vol. 163, pp. 116–127, 2018.

[65] E. J. Lee, D. E. Kim, E. U. Azeloglu, and K. D. Costa, "Engineered Cardiac Organoid Chambers: Toward a Functional Biological Model Ventricle," *Tissue Eng. - Part A*, vol. 14, no. 2, pp. 215–225, 2008.

[66] Y. B. Lee *et al.*, "Bio-printing of collagen and VEGF-releasing fibrin gel scaffolds for neural stem cell culture," *Exp. Neurol.*, vol. 223, no. 2, pp. 645–652, 2010.

[67] N. Davidenko *et al.*, "Evaluation of cell binding to collagen and gelatin: a study of the effect of 2D and 3D architecture and surface chemistry," *J. Mater. Sci. Mater. Med.*, vol. 27, no. 10, 2016.

[68] S. Ricard-Blum, "The Collagen Family," *Cold Spring Harb. Perspect. Biol.*, vol. 3, no. 1, pp. 1–19, Jan. 2011.

[69] M. Tallawi *et al.*, "Strategies for the chemical and biological functionalization of scaffolds for cardiac tissue engineering: A review," *J. R. Soc. Interface*, vol. 12, no. 108, 2015.

[70] C. Michon, G. Cuvelier, and B. Launay, "Concentration dependence of the critical viscoelastic properties of gelatin at the gel point," *Rheol. Acta*, vol. 32, no. 1, pp. 94–103, Jan. 1993.

[71] C. D. Roche, P. Sharma, A. W. Ashton, C. Jackson, M. Xue, and C. Gentile, “Printability, Durability, Contractility and Vascular Network Formation in 3D Bioprinted Cardiac Endothelial Cells Using Alginate–Gelatin Hydrogels,” *Front. Bioeng. Biotechnol.*, vol. 9, p. 110, Feb. 2021.

[72] G. Camci-Unal, D. Cuttica, N. Annabi, D. Demarchi, and A. Khademhosseini, “Synthesis and characterization of hybrid hyaluronic acid-gelatin hydrogels,” *Biomacromolecules*, vol. 14, no. 4, pp. 1085–1092, 2013.

[73] K. Yue, G. Trujillo-de Santiago, M. M. Alvarez, A. Tamayol, N. Annabi, and A. Khademhosseini, “Synthesis, properties, and biomedical applications of gelatin methacryloyl (GelMA) hydrogels,” *Biomaterials*, vol. 73, pp. 254–271, 2015.

[74] D. Loessner *et al.*, “Functionalization, preparation and use of cell-laden gelatin methacryloyl-based hydrogels as modular tissue culture platforms,” *Nat. Protoc.*, vol. 11, no. 4, pp. 727–746, 2016.

[75] J. Yin, M. Yan, Y. Wang, J. Fu, and H. Suo, “3D Bioprinting of Low-Concentration Cell-Laden Gelatin Methacrylate (GelMA) Bioinks with a Two-Step Cross-linking Strategy,” *ACS Appl. Mater. Interfaces*, vol. 10, pp. 6849–6857, 2018.

[76] K. Yue *et al.*, “Structural analysis of photocrosslinkable methacryloyl-modified protein derivatives,” *Biomaterials*, vol. 139, pp. 163–171, Sep. 2017.

[77] Gelatin Manufacturers Institute of America, “GMIA Handbook,” *Gelatin Handb.*, p. 26, 2019.

[78] W. Liu *et al.*, “Extrusion Bioprinting of Shear-Thinning Gelatin Methacryloyl Bioinks,” *Adv. Healthc. Mater.*, vol. 6, no. 12, pp. 1–11, 2017.

[79] Y. C. Chen *et al.*, “Functional human vascular network generated in photocrosslinkable gelatin methacrylate hydrogels,” *Adv. Funct. Mater.*, vol. 22, no. 10, pp. 2027–2039, 2012.

[80] J. W. Nichol, S. T. Koshy, H. Bae, C. M. Hwang, S. Yamanlar, and A. Khademhosseini, “Cell-laden microengineered gelatin methacrylate hydrogels,” *Biomaterials*, vol. 31, no. 21, pp. 5536–5544, Jul. 2010.

[81] E. Hoch, C. Schuh, T. Hirth, G. E. M. Tovar, and K. Borchers, “Stiff gelatin hydrogels can be photo-chemically synthesized from low viscous gelatin solutions using molecularly functionalized gelatin with a high degree of methacrylation,” *Journal of Materials Science: Materials in Medicine*, vol. 23, no. 11. pp. 2607–2617, 2012.

[82] M. Y. Shie, J. J. Lee, C. C. Ho, S. Y. Yen, H. Y. Ng, and Y. W. Chen, “Effects of Gelatin Methacrylate Bio-ink Concentration on Mechano-Physical Properties and Human Dermal Fibroblast Behavior,” *Polym. 2020, Vol. 12, Page 1930*, vol. 12, no. 9, p. 1930, Aug. 2020.

[83] J. Faix and K. Rottner, “The making of filopodia,” *Curr. Opin. Cell Biol.*, vol. 18, no. 1, pp. 18–25, Feb. 2006.

[84] T. W. Oates, S. C. Maller, J. West, and B. Steffensen, “Human Gingival Fibroblast Integrin Subunit Expression on Titanium Implant Surfaces,” *J. Periodontol.*, vol. 76, no. 10, pp. 1743–1750, Oct. 2005.

[85] A. Blaeser, D. F. Duarte Campos, U. Puster, W. Richtering, M. M. Stevens, and H. Fischer, “Controlling Shear Stress in 3D Bioprinting is a Key Factor to Balance Printing Resolution and Stem Cell Integrity,” *Adv. Healthc. Mater.*, vol. 5, no. 3, pp. 326–333, 2016.

[86] W. Liu *et al.*, “Coaxial extrusion bioprinting of 3D microfibrous constructs with cell-favorable gelatin methacryloyl microenvironments,” *Biofabrication*, vol. 10, no. 2, 2018.

[87] B. Mirani, E. Stefanek, B. Godau, S. M. Hossein Dabiri, and M. Akbari, “Microfluidic 3D printing of a photo-cross-linkable bioink using insights from computational modeling,” *ACS Biomater. Sci. Eng.*, vol. 7, no. 7, pp. 3269–3280, 2021.

[88] B. Grigoryan *et al.*, “Multivascular networks and functional intravascular topologies within biocompatible hydrogels,” *Science (80-.).*, vol. 364, pp. 458–464, 2019.

[89] L. S. Magalhaes *et al.*, “Printing 3D Hydrogel Structures Employing Low-Cost Stereolithography Technology,” *J. Funct. Biomater.*, vol. 11, no. 12, 2020.

[90] Z. Wang *et al.*, “Visible Light Photoinitiation of Cell-Adhesive Gelatin Methacryloyl Hydrogels for Stereolithography 3D Bioprinting,” *Appl. Mater. Interfaces*, vol. 10, pp. 26859–26869, 2018.

[91] T. Lam *et al.*, “Photopolymerizable gelatin and hyaluronic acid for stereolithographic 3D bioprinting of tissue-engineered cartilage,” *J. Biomed. Mater. Res. Part B Appl. Biomater.*, vol. 107B, no. 8, pp. 2649–2657, 2019.

[92] CELLINK, “Lumen X Brochure,” 2020.

[93] V. M. Schoop, N. Mirancea, and N. E. Fusenig, “Epidermal Organization and Differentiation of HaCaT Keratinocytes in Organotypic Coculture with Human Dermal Fibroblasts,” *J. Invest. Dermatol.*, vol. 112, no. 3, pp. 343–353, Mar. 1999.

[94] H. E. Abaci *et al.*, “Human Skin Constructs with Spatially Controlled Vasculature Using Primary and iPSC-Derived Endothelial Cells,” *Adv. Healthc. Mater.*, vol. 5, pp. 1800–1807, 2016.

[95] Y. Kim *et al.*, “Establishment of a complex skin structure via layered co-culture of keratinocytes and fibroblasts derived from induced pluripotent stem cells,” *Stem Cell Res. Ther.*, vol. 9, no. 1, pp. 1–10, Aug. 2018.

[96] M. Sonnaert, I. Papantoniou, F. P. Luyten, and J. Schrooten, “Quantitative Validation of the Presto Blue$^{\text{TM}}$ Metabolic Assay for Online Monitoring of Cell Proliferation in a 3D Perfusion Bioreactor System,” *Tissue Eng. - Part C Methods*, vol. 21, no. 6, pp. 519–529, Mar. 2015.

[97] F. Tabatabaei, K. Moharamzadeh, and L. Tayebi, “Fibroblast encapsulation in gelatin methacryloyl (GelMA) versus collagen hydrogel as substrates for oral mucosa tissue engineering,” *J. Oral Biol. Craniofacial Res.*, vol. 10, no. 4, pp. 573–577, 2020.

[98] Canadian Institutes for Health Research, Natural Sciences and Engineering Research Council of Canada, and Social Sciences and Humanities Research Council, “Tri-Council Policy Statement: Ethical Conduct for Research Involving Humans,” 2018.

[99] H. Shin, B. D. Olsen, and A. Khademhosseini, “The mechanical properties and cytotoxicity of cell-laden double-network hydrogels based on photocrosslinkable gelatin and gellan gum biomacromolecules,” *Biomaterials*, vol. 33, no. 11, pp. 3143–3152, 2012.

[100] P. Boukamp, R. T. Petrussevska, D. Breitkreutz, J. Hornung, A. Markham, and N. E. Fusenig, “Normal keratinization in a spontaneously immortalized aneuploid human

keratinocyte cell line," *J. Cell Biol.*, vol. 106, no. 3, pp. 761–771, Mar. 1988.

[101] I. Colombo *et al.*, "HaCaT Cells as a Reliable In Vitro Differentiation Model to Dissect the Inflammatory/Repair Response of Human Keratinocytes," *Mediators Inflamm.*, 2017.

[102] N. Maas-Szabowski, A. Stärker, and N. E. Fusenig, "Epidermal tissue regeneration and stromal interaction in HaCaT cells is initiated by TGF-α," *Journal of Cell Science*, vol. 116, no. 14. The Company of Biologists, pp. 2937–2948, 15-Jul-2003.

[103] A. T. Feldman and D. Wolfe, "Tissue processing and hematoxylin and eosin staining," *Methods Mol. Biol.*, vol. 1180, pp. 31–43, 2014.

[104] A. Vila *et al.*, "Hydrogel co-networks of gelatine methacrylate and poly (ethylene glycol) diacrylate sustain 3D functional in vitro models of intestinal mucosa," *Biofabrication*, vol. 12, no. 2, 2020.

[105] M. N. M. Walter, K. T. Wright, H. R. Fuller, S. MacNeil, and W. E. B. Johnson, "Mesenchymal stem cell-conditioned medium accelerates skin wound healing: An in vitro study of fibroblast and keratinocyte scratch assays," *Exp. Cell Res.*, vol. 316, no. 7, pp. 1271–1281, Apr. 2010.

[106] M. Fouché, C. Willers, S. Hamman, C. Malherbe, and J. Steenekamp, "Wound Healing Effects of Aloe muth-muth: In Vitro Investigations Using Immortalized Human Keratinocytes (HaCaT)," *Biol. 2020, Vol. 9, Page 350*, vol. 9, no. 11, p. 350, Oct. 2020.

[107] R. Raizman, W. Little, and A. C. Smith, "Rapid diagnosis of Pseudomonas aeruginosa in wounds with point-of-care fluorescence imaing," *Diagnostics*, vol. 11, no. 2, Feb. 2021.

[108] R. Serra *et al.*, "Chronic wound infections: the role of Pseudomonas aeruginosa and Staphylococcus aureus," *Expert Rev. Anti. Infect. Ther.*, vol. 13, no. 5, pp. 605–613, May 2015.

[109] T. B. Doyle, A. C. Hawkins, and L. L. McCarter, "The complex flagellar torque generator of Pseudomonas aeruginosa," *J. Bacteriol.*, vol. 186, no. 19, pp. 6341–6350, Oct. 2004.

[110] M. M. Bashir, M. R. Sharma, and V. P. Werth, "TNF-α production in the skin," *Archives of Dermatological Research*, vol. 301, no. 1. Springer, pp. 87–91, 30-Jan-2009.

[111] A. Oliveira and M. D. L. R. S. Cunha, “Comparison of methods for the detection of biofilm production in coagulase-negative staphylococci,” *BMC Res. Notes*, vol. 3, no. 1, pp. 1–8, Oct. 2010.

[112] E. Darwin and M. Tomic-Canic, “Healing Chronic Wounds: Current Challenges and Potential Solutions.”